



**THE EFFECTS OF RARE EARTH DOPING
ON GALLIUM NITRIDE THIN FILMS**

DISSERTATION

Stephen R. McHale, Lieutenant Colonel, USA
AFIT/DS/ENP/11-S05

**DEPARTMENT OF THE AIR FORCE
AIR UNIVERSITY**

AIR FORCE INSTITUTE OF TECHNOLOGY

Wright-Patterson Air Force Base, Ohio

DISTRIBUTION STATEMENT A
APPROVED FOR PUBLIC RELEASE; DISTRIBUTION UNLIMITED

The views expressed in this document are those of the author and do not reflect the official policy or position of the United States Air Force, the United States Department of Defense or the United States Government. This material is declared a work of the U.S. Government and is not subject to copyright protection in the United States.

AFIT/DS/ENP/11-S05

THE EFFECTS OF RARE EARTH DOPING ON GALLIUM NITRIDE THIN
FILMS

DISSERTATION

Presented to the Faculty
Graduate School of Engineering and Management
Air Force Institute of Technology
Air University
Air Education and Training Command
in Partial Fulfillment of the Requirements for the
Degree of Doctor of Philosophy

Stephen R. McHale, BS, MS
Lieutenant Colonel, USA

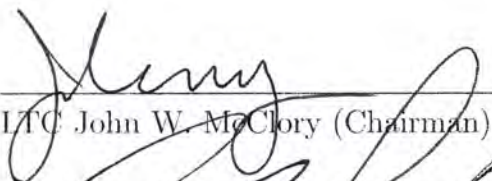
September 2011

DISTRIBUTION STATEMENT A
APPROVED FOR PUBLIC RELEASE; DISTRIBUTION UNLIMITED

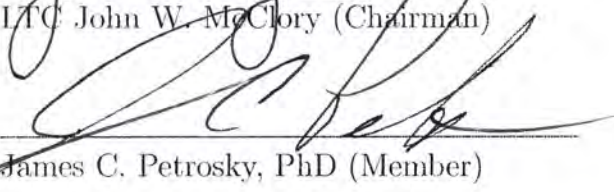
THE EFFECTS OF RARE EARTH DOPING ON GALLIUM NITRIDE THIN
FILMS

Stephen R. McHale, BS, MS
Lieutenant Colonel, USA

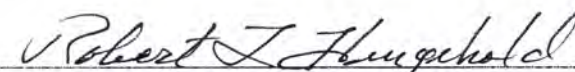
Approved:


LTC John W. McClory (Chairman)

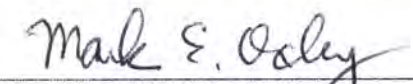
29 Aug 11
Date


James C. Petrosky, PhD (Member)

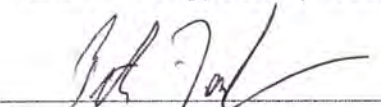
24 Aug 11
Date


Robert L. Hengehold, PhD (Member)

24 Aug 2011
Date



Mark E. Oxley, PhD (Member)

24 Aug 2011
Date


Peter A. Dowben, PhD (Member)

17 Aug 2011
Date

Accepted:


M. U. Thomas
Dean, Graduate School of Engineering
and Management

30 Aug 2011
Date

Abstract

The thermal neutron capture cross section of the rare earth metal isotope ^{157}Gd is 255,000 barns and is the largest of all known natural isotopes, which distinguishes the material as a logical candidate for neutron detection. Semiconductors that incorporate large neutron absorption cross section elements, such as gadolinium, are gaining attention. Despite the relative immaturity of the development of such semiconductors, gallium nitride is one such semiconductor material that has attained considerable recognition. In spite of study over the past two decades, there still exists an incomplete understanding of the physical and electronic properties of GaN materials, particularly whether even low concentrations of a rare earth in a GaN host can alter the surface electronic structure. To address this concern, investigations of the surface electronic structure and interface properties of GaN thin films doped with three distinct rare earths (Yb, Er, Gd) were undertaken using photoemission spectroscopy.

The effective Debye temperatures of ytterbium and gallium in GaN:Yb thin films were obtained using X-ray photoemission spectroscopy. The vibrational motion normal to the surface resulted in a diminution of photoemission intensities from which the effective Debye temperatures of 221 ± 30 K and 308 ± 30 K for Yb and Ga, respectively, were estimated. The similarity between the Yb and Ga Debye temperatures is indicative of a substitutional occupation of a Ga site by a Yb ion. The slightly smaller effective surface Debye temperature for Yb correlates to a soft, strained surface, possibly due to an increased Yb–N bond length as compared to the Ga–N bond length.

Bonding with the GaN and rare earth $4f$ hybridization were also examined. The

$4d \rightarrow 4f$ super Coster-Kronig resonances for various rare earth doped GaN thin films (RE = Yb, Er, Gd) were investigated using synchrotron photoemission spectroscopy. Resonant photoemission Fano profiles showed that the major Gd and Er rare earth $4f$ weight was at about 5–6 eV below the valence band maximum, similar to the $4f$ weights in the valence band of many other rare earth doped semiconductors. For Yb, there was very little resonant enhancement of the valence band of Yb doped GaN, consistent with a largely $4f^{14}$ occupancy. The placement of the occupied Gd, Er and Yb $4f$ levels, deep within the valence band, suggested that the intra-atomic f – f transitions may be more ‘blue’ than predicted by theoretical models. The Schottky barriers formed at the interface between gold and the various rare earth doped GaN thin films were also investigated *in situ* using synchrotron photoemission spectroscopy. We found compelling evidence that thin layers of gold do not wet and uniformly cover the GaN surface, even with rare earth doping of the GaN. The resultant Schottky barrier heights were measured as 1.68 ± 0.1 eV (GaN:Yb), 1.64 ± 0.1 eV (GaN:Er), and 1.33 ± 0.1 eV (GaN:Gd), which were 25–55% larger than those reported at the gold to undoped GaN interface. The trend of the Schottky barrier heights followed the trend of the rare earth metal work function.

The utility of gadolinium as a neutron detection material in a hypothetical direct conversion homojunction was examined via fundamental nuclear and semiconductor physics. In the single neutron detection limit, the charge produced in a Gd-based semiconductor by an internal conversion electron created from ^{157}Gd neutron capture was found to approach the intrinsic noise level of commercial preamplifiers required for pulse height analysis. The fraction of captured neutrons, and hence efficiency, was maximized with Gd-layer thickness, and the range of internal conversion electrons created from neutron capture by ^{157}Gd was estimated to be ~ 20 – 25 μm . Full depletion of a Gd-based homojunction to the 25 μm range of the internal conversion electrons was seen to be contrary to low power operation.

AFIT/DS/ENP/11-S05

To my beautiful wife and our two spirited children.

Acknowledgements

Many people and organizations warrant a ration of gratitude for their direct contributions to this research effort. First, this research was funded in part through the Defense Threat Reduction Agency. Without their material support, none of this research would have been possible.

It was my distinct privilege to work with a research committee that was dedicated to providing me with opportunities for success in the classroom, in the laboratory, and throughout the preparation of conference presentations and journal manuscripts. In particular, John McClory and Jim Petrosky might recall that the initial pace and direction they set for this research endeavor caused mild trepidation on my part. Nevertheless, in true Army fashion, their foresight at the outset and leadership during the past few years were always aimed at reaching the final objective in a timely and efficient manner, i.e., on time and on target.

I must also thank Yaroslav Losovyj for his patient instruction in teaching me the techniques that were vital to this research, and for the regular dinner invitations and welcoming environment that he and his wife created during my many extended visits to Baton Rouge. As a result, he is a mentor, colleague, and friend to me, all at once.

Peter Dowben's vast expertise in many fields of physics is an impressive rarity, but the modest and good-natured posture he maintains with regard to this expertise is equally impressive. Without his innate ability to synthesize massive amounts of data with tremendous speed and insight, I would almost certainly still be staring at trees. Thank you, Peter, for providing me with a few glimpses of the forest that you gaze upon.

As my research advisor, John McClory's contribution to my success cannot possibly be overstated. He was the first person to reach out to me when I returned to AFIT, and he has been involved thoroughly with every aspect of my education,

research, and personal and professional development since that time. Moreover, John's ability to analyze technical and interpersonal situations thoughtfully and, at the same time, with levity is refreshing.

My most heartfelt thanks are reserved for my loving wife, whose unwavering support deserves multiple honorary degrees in the fields of patience, understanding, curiosity, and cheerleading. Any success I may have had resulted from her constant encouragement and countless personal sacrifices. She will always be number one to me.

Stephen R. McHale

Table of Contents

	Page
Abstract	iv
Acknowledgements	vii
List of Figures	xii
List of Tables	xviii
List of Abbreviations	xix
List of Symbols	xx
I. Introduction	1
1.1 Motivation	1
1.2 Special Nuclear Material Detection	3
1.2.1 Detection Challenges	3
1.2.2 Ionizing Radiation Interactions with Matter	7
1.2.3 Non-ionizing Radiation Interactions with Matter	9
1.3 General Neutron Detector Design Considerations	14
1.4 Research Objectives and Overview	20
References	23
II. Theory	28
2.1 Photoelectron Spectroscopy Models	28
2.1.1 Optical Excitation of the Electron in the Solid	30
2.1.2 Transport of the Electron to the Surface	33
2.1.3 Escape of the Electron into Vacuum	34
2.2 Resonant Photoemission Spectroscopy	37
2.3 Temperature-Dependent X-ray Photoemission Spectroscopy	40
2.4 The Schottky Barrier	43
2.4.1 Schottky-Mott Model	44
2.4.2 Metal Induced Gap States Model	46
2.4.3 Current Transport in Schottky Barrier Devices	51
References	54
III. Experimental Procedures	58
3.1 Sample Growth and Characterization	58
3.2 Sample Surface Preparation	62
3.3 Photoemission Spectroscopy Considerations	63
3.4 Photoemission Spectra Conditioning	66

	Page
3.4.1 Conversion to Binding Energy	66
3.4.2 Removal of Background and Secondary Electron Signals	69
3.4.3 Spectra Normalization	70
3.4.4 Spectral Feature Deconvolution	71
3.5 Schottky Barrier Considerations	73
References	75
IV. The Effective Surface Debye Temperature of Yb:GaN	77
4.1 Introduction	77
4.2 Experimental	79
4.3 Results and Discussion	80
4.4 Conclusions	83
References	84
V. Resonant Photoemission of Rare Earth Doped GaN Thin Films	87
5.1 Introduction	87
5.2 Experimental	89
5.3 Results and Discussion	91
5.3.1 The $4f$ Contributions to the Valence Band of Doped GaN	91
5.3.2 The $4f$ Contributions to the Valence Band of GaN:Gd	94
5.3.3 The $4f$ Contributions to the Valence Band of GaN:Er	94
5.3.4 The $4f$ Contributions to the Valence Band of GaN:Yb	97
5.4 Summary and Conclusions	98
References	99
VI. Schottky Barrier Formation at the Au to Rare Earth Doped GaN Thin Film Interface	105
6.1 Introduction	105
6.2 Experimental	107
6.3 Results and Discussion	108
6.3.1 The Rare Earth Doped GaN Surfaces	108
6.3.2 The Growth of Gold Overlayers on RE:GaN Surfaces	112
6.3.3 Schottky Barrier Formation at RE:GaN Surfaces	114
6.4 Conclusions	120

	Page
References	120
VII. Neutron Detection Using Gadolinium	126
7.1 Overview	126
7.2 Single Neutron Capture Event	127
7.2.1 Gd-157 Neutron Capture Scheme	127
7.2.2 Ionizing Radiation Charge Production	130
7.3 Detector Circuit Considerations	132
7.4 Material and Geometry Considerations	137
References	147
VIII. Conclusions	149
8.1 Summary of Findings	149
8.2 Future Work	151
References	157

List of Figures

Figure		Page
1.	Microscopic cross section hierarchy used to calculate neutron interaction rates.	12
2.	General schematic (top view) of a hypothetical solid state semiconducting device capable of neutron detection.	14
3.	Scintillation detector schematics.	17
4.	Solid state neutron conversion detector schematics.	18
5.	Neutron absorption (detection and capture efficiencies) as a function of detector thickness.	18
6.	Energy dependent neutron capture cross sections for various materials.	19
7.	The photoelectron energy distribution produced by incoming photons and measured as a function of the kinetic energy E_{kin} of the photoelectrons (right) is more conveniently expressed in terms of the binding energy E_B (left) when one refers to the density of states inside the solid ($E_B = 0$ at E_F .)	29
8.	Schematic molecular-orbital diagram of the resonant photoemission process for a hypothetical solid.	38
9.	Plot of Fano function using $h\nu_j = 140$ eV, $\Delta h\nu_j = 3$ eV, and $q = 2$	40
10.	Ideal Schottky barrier formation.	45
11.	Schematic energy diagram of a practical metal-semiconductor interface with a continuum of interface states.	47
12.	Barrier heights of various metal to n -Si contacts as a function of electronegativity difference. The theoretical MIGS line (solid) is drawn using a least squares fit of the data with $\Phi_{zc} = 0.792$ and $S_X = 0.113$	50
13.	Typical molecular beam epitaxy schematic.	59

Figure		Page
14.	Typical pulsed laser deposition schematic.....	60
15.	The X-ray diffraction (XRD) pattern of a GaN:Yb film grown on Si(111) substrates. The films show <i>c</i> -axis orientation of the texture growth and a high level of crystallinity. The presence of any secondary phases or spurious peaks has not been observed.	61
16.	Sample mounting technique used at the Center for Advanced Microstructures and Devices.	63
17.	Schematic of the 3-meter Toroidal Grating Monochromator (3m TGM) beamline at the Center for Advanced Microstructures and Devices.	64
18.	Typical layout for electron kinetic energy analysis.	65
19.	Raw spectra of intensity versus kinetic energy for GaN:Yb (black) and tantalum foil (red) using 90 eV photons.	66
20.	Kinetic energy of spectrometer Fermi level using 90 eV photons. The Fermi level is established at the intersection between the Fermi-Dirac distribution at $T = 300$ K (black) and the experimentally observed tantalum density of states (red).	67
21.	Raw spectrum of intensity versus binding energy for GaN:Yb using 90 eV photons. The valence band maximum (VBM) is located by linear extrapolation of the high kinetic energy edge of the spectrum at the intersection of zero background.	68
22.	Removal of secondary electron influence using Origin Baseline Toolkit. Several intensity values (squares) are used to fit a baseline (red), which is subtracted from the sample spectra.	70
23.	Deconvolution of valence band and shallow core level lineshapes from example GaN:RE photoemission spectra.	72
24.	Semiconductor surface valence band bending via core level shift.	74

Figure		Page
25.	The X-ray diffraction (XRD) pattern of a GaN:Yb film grown on Si(111) substrates. The films show c -axis orientation of the texture growth and a high level of crystallinity. The presence of any secondary phases or spurious peaks has not been observed.	79
26.	Temperature dependent X-ray photoemission spectra of the indicated core levels after background subtraction.	81
27.	Logarithm of the core peak photoemission intensities for Yb and Ga as a function of temperature following background (I_{BG}) subtraction and normalization to the peak intensity at the lowest temperature I_0 . The experimental values were fitted (solid line) with the Debye-Waller factor.	82
28.	Energy distribution curves of GaN:Gd for various incident photon energies, as shown for each spectrum. The strong surface and bulk $4f$ Gd components of the GaN:Gd valence band are illustrated. Resonating components C (-8.1 eV) and D (-9.6 eV), used for the constant initial state curves in Figure 31, are shown at the bottom.	92
29.	Energy distribution curves of GaN:Er for various incident photon energies, as shown for each spectrum. The resonating components C (-8.9 eV) and D (-10.7 eV), used for the constant initial state curve in Figure 32, are shown at the bottom.	92
30.	Energy distribution curves of GaN:Yb for various incident photon energies, as shown for each spectrum. Resonating components C (-6.2 eV) and D (-7.6 eV), used for the constant initial state curve in Figure 33, are shown at the bottom.	93
31.	Constant initial state curves and Fano fit (solid lines) for feature C (squares) at -8.1 eV and feature D (triangles) at -9.6 eV in GaN:Gd. The fitting component, q , for feature C was calculated as 1.91; for feature D it was 2.79.	95

32. Constant initial state curve (triangles) and Fano fit (solid lines) for the valence band feature in the vicinity of -9 eV binding energy, for GaN:Er. The fitting component, q , in the region of the Er $4d_{5/2}$ absorption threshold (166 eV) was calculated as 1.55; in the region of the Er $4d_{3/2}$ absorption threshold (173 eV) it was 2.14. 96
33. Constant initial state curve (squares) and Fano fit (solid lines) for the valence band features in the vicinity of -7 eV binding energy, for GaN:Yb. The fitting component, q , in the region of the Yb $4d_{5/2}$ absorption threshold (179 eV) was calculated as 0.33; in the region of the Yb $4d_{3/2}$ absorption threshold (189 eV) it was 1.15..... 97
34. Deconvolution of Ga $3d$ core-level spectra (a) and evolution of valence band and Au $4f$ bands (b) with increasing Au coverage on Yb:GaN thin film. The components attributed to bulk GaN features are shown with solid black lines. The lower binding energy ‘surface’ component, shown as the orange line, is removed with increasing Au coverage and is replaced with Au-GaN and Au-RE alloy features (solid green lines). 110
35. Deconvolution of Ga $3d$ core-level spectra and valence band evolution with increasing Au coverage on Er:GaN (a) and Gd:GaN (b) thin films. The components attributed to bulk GaN features are shown with solid black lines. The lower binding energy ‘surface’ component, shown as the orange solid line, is removed with increasing Au coverage and is replaced with Au-GaN and Au-RE alloy features (solid green lines)..... 111
36. The intensity ratio of the Ga $3d$ core level before I_0 and after I_s Au deposition as a function of film thickness for the deposition of Au on RE:GaN, as indicated. The expected ratio as a function of thickness (dashed lines) is plotted using the Volmer-Weber growth mode. 114

Figure		Page
37.	Fermi level movement (a) and Schottky Barrier formation (b) at the surface of Gd:GaN based upon the binding energy of the bulk component of a Ga $3d$ core level taken at a photon energy of 90 eV. The filled region in (b) indicates the range of ideal barrier height values, as predicted by the Schottky-Mott model using our measured χ values from Table 3.	118
38.	De-excitation schemes of $^{158}\text{Gd}^*$ following neutron capture by ^{157}Gd	127
39.	Q_{max} creation from (red): a single ^{157}Gd neutron capture event resulting in 79 keV internal conversion electron emission, as a function of molar concentration x in $\text{Gd}_x\text{Ga}_{1-x}\text{N}$; (black): a single neutron capture event in B_5C resulting in 0.84 MeV ^7Li ion production.	131
40.	Example of detector current pulse where t_c represents collection time.	133
41.	Pulse height spectra and background (inset) from a B_5C heterojunction detector. Each spectra was collected for 600 seconds at the reactor power indicated. The three identifiable peaks are attributable to the boron capture products. The 1.02 MeV peak is lost in the continuum between the 0.84 MeV and 1.47 MeV peaks owing to its branching ratio.	135
42.	Elements of a typical signal chain for pulse height analysis.	135
43.	System for measuring charge-sensitive preamplifier noise.	135
44.	Depletion width as a function of bias for a hypothetical Gd-based (100% ^{157}Gd) homojunction neutron detector using $N_D = 10^{19}$ and $N_A = 10^{14}$	140
45.	Schematic of GEANT4 simulation of thermal neutrons incident on a $\text{HfO}_2\text{:Gd}$ on silicon heterojunction. The doping concentration was 15% natural Gd.	143
46.	GEANT4 simulation output.	143

Figure		Page
47.	Fraction of absorbed neutrons as a function of film thickness for B_5C and GdN . A one dimensional monoenergetic narrow beam of thermal neutrons is assumed.	145
48.	Photon energy dependent mean free path λ , determined from NIST-tabulated values of μ/ρ for natural Gd	146
49.	Logarithm of forward current density versus applied voltage for NTE555 PIN Schottky Diode (points) and least squares fit (line) in the linear region of the diode characteristic.	152
50.	Logarithm of forward current density versus applied voltage for NTE555 PIN Schottky Diode (points) and theoretical current density (lines) for a Schottky contact with $\Phi_{B,n} = 0.94$ eV and ideality factors $\eta = 1$ (yellow) and $\eta = 1.55$ (purple).	154
51.	Single quantum well schematic.	156
52.	Superlattice structure schematic.	156

List of Tables

Table		Page
1.	Selected properties of common special nuclear material.	5
2.	Prompt fission energy distribution.	11
3.	Measured properties of clean RE:GaN surfaces. Experimental uncertainties are listed only when explicitly stated within the indicated references.	109
4.	Comparison between experimentally measured and theoretically predicted (Schottky-Mott) barrier heights. Experimental uncertainties are listed only when explicitly stated within the indicated references.	117
5.	Summary of ionizing radiation produced from neutron capture by ^{157}Gd	130
6.	Diode parameters for charge pulse rate comparison. Parameters common to both materials are: $\Phi_{th} = 10^4 \text{ n cm}^{-2}\text{s}^{-1}$; $A_c = \pi(0.1 \text{ cm})^2/4$; $W = 4.2 \mu\text{m}$	138

List of Abbreviations

Abbreviation	Page
DHS	Department of Homeland Security 1
SNM	Special Nuclear Material 3
^{235}U	Uranium-235 4
^{239}Pu	plutonium-239 4
^{238}U	Uranium-238 4
NNDC	National Nuclear Data Center 6
^{10}B	boron-10 16
^6Li	lithium-6 16
^3He	helium-3 16
TLD	thermoluminescent dosimeters 16
^{157}Gd	gadolinium-157 18
GaN	Gallium nitride 20
RE	rare earth 20
XPS	X-ray photoemission spectroscopy 21
PES	photoelectron spectroscopy 28
RPES	Resonant photoemission spectroscopy 37
ARUPS	angle-resolved ultraviolet photoemission spectroscopy 39
I-V	current-voltage 44
C-V	capacitance-voltage 44
MIGS	metal induced gap states 46
CAMD	Center for Advanced Microstructures and Devices 58
XRD	X-ray diffraction 60

List of Symbols

Symbol		Page
N_{AV}	Avogadro's number	10
M_{AW}	Molar mass	10
σ	Microscopic nuclear cross section	11
Σ	Macroscopic nuclear cross section	12
\dot{R}_{vol}	Reaction rate density	13
Φ	Neutron flux	13
E_{ion}	Energy of an ionizing agent	15
E_g	Bandgap energy	15
$h\nu$	Photon energy	28
ϕ	Work function	28
E_B	Binding energy	28
E_{kin}	Kinetic energy	28
$N(E, h\nu)$	Photoelectron energy distribution	30
\mathbf{A}	Vector potential	30
c	Speed of light in a vacuum	31
\mathbf{p}	Momentum operator	31
φ	Scalar potential	31
\mathbf{k}	Wave vector of electronic state	32
W	Debye-Waller factor	42
$\langle u_0 \rangle^2$	Mean square displacement of atom	42
$\hbar(\Delta k)$	Debye model electron momentum transfer	42
Θ_D	Debye temperature	42

Symbol		Page
$\Phi_{B,n}$	Schottky barrier (n -type semiconductor)	45
χ_s	Electron affinity (semiconductor)	45
E_F	Fermi level energy	45
E_V	Energy of valence band maximum	45
\mathcal{E}	Electric field	132
W	Depletion width	138
N_A	Acceptor impurity concentration	139
N_D	Donor impurity concentration	139
η	Ideality factor	153

THE EFFECTS OF RARE EARTH DOPING ON GALLIUM NITRIDE THIN FILMS

I. Introduction

1.1 Motivation

Nuclear radiation detection has long been one of the most troublesome homeland security challenges, and is not exclusively a post-9/11 concern. Months after the United States used the first nuclear weapons against Japan, apprehensive lawmakers asked Robert Oppenheimer, widely regarded as “The Father of the Atomic Bomb,” how authorities would detect a nuclear weapon in an incoming shipping crate. He replied, “with a screwdriver,” meaning the only device that would do the job was a screwdriver to open every incoming box and crate [1]. Many of the conclusions from the aptly dubbed and still classified “Screwdriver Report,” co-authored by top physicists and Manhattan Project veterans Robert Hofstadter and Wolfgang Panofsky, remain largely unchanged today. Consequently, in 2007, while serving as the director emeritus of the Stanford Linear Accelerator Center, Panofsky defended the validity of the report’s assertions, stating that “the laws of physics have not changed one bit,” and that nuclear devices remain virtually undetectable “unless you are, say, ten feet away from it—and even then it can be quite easily shielded” [2].

While the central point of Panofsky’s report is still valid, in that radioactive material emits less radiation with distance and shielding from the source, not everyone completely agrees with him; Department of Homeland Security (DHS) officials claim that state-of-the-art detectors offer far better performance. Nevertheless, DHS continues its vigilant pursuit of improved radiation detector design, performance, and

efficiency.

The creation of DHS provided the impetus to invigorate a radiation detector market considered by many to be saturated or, at best, growing slowly because neither incentives to invest in new technology nor demands for new applications existed. In 2002, DHS enlisted the assistance of the American National Standards Institute (ANSI), which oversees the development of voluntary consensus standards for products, services, processes, systems, and personnel in the United States. DHS and ANSI collaborated to develop and adopt, within an unprecedented two-year time frame, four American national standards designed to assist federal agencies, as well as state and local officials, in procurement decisions related to radiological and nuclear detection equipment [3].

These new standards, coupled with DHS funding, stimulated demand for innovative ideas, technology, and instruments, thus improving miniaturization, efficiency, accuracy, and operation of radiation detectors for homeland security users. As one example, *Instrument Business Outlook* projected 14.5% and 13.7% global market growth rates for personal radiation detectors, radioactive isotope identification devices, and radiation portal monitors for the years 2006 and 2007, respectively, with anticipated increases in subsequent years [4]. Furthermore, DHS's Radiation Portal Monitor Program (RPMP) seeks to deploy a suite of stationary, mobile, and hand-held radiation detection systems at all U.S. Customs and Border Protection (CBP) ports of entry. The objective is to scan 100% of all traffic and cargo for nuclear and radioactive materials, while maintaining the efficient flow of commerce. In November 2009, DHS Secretary Janet Napolitano announced the RPMP's full deployment of non-intrusive scanning equipment to detect radiation emanating from nuclear device material across all northern border land points of entry into the United States [5].

While these efforts are noteworthy, we cannot underestimate our enemies' ambitions to circumvent the capabilities of our current detection systems. The RPMP

directs the preponderance of efforts toward the proactive detection of radioactive material at high volume entry points; hence, its assets are mostly fixed, or vehicle-mobile, and these assets are concentrated at roadway entry points. Accordingly, we must continue to develop novel radiation detection technologies, which accurately and efficiently identify nuclear material via proactive cargo screening. We must also provide our first responders (firefighters, law enforcement, emergency medical) with reaction capability during crisis situations, such as a hostile dispersion of radiological material on American soil.

In the succeeding sections, analysis of the radioactive decay modes of nuclear weapon material isotopes will show that neutron detection potentially offers the most accurate method of detecting Special Nuclear Material (SNM). Radiation detector design considerations will be discussed briefly, and the ever-present problem of detecting nuclear weapon material in an incoming shipping crate will be addressed.

1.2 Special Nuclear Material Detection

1.2.1 Detection Challenges.

In response to recent worldwide events, our nation's ability to monitor and intercept special nuclear material has become a top national security priority [6]. Cargo screening at ports of entry requires standoff detection at distances of several meters or more, but the low intrinsic activity of special nuclear material, coupled with the limited range of SNM-emitted charged particles and gamma rays, combine to present challenges to standoff detection capability.

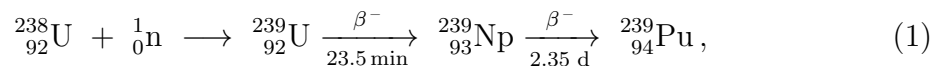
Neutron background also complicates the ability to discern a legitimate signal from persistent noise. Specifically, the cosmic ray-induced spallation neutron background of $\sim 120 - 150 \text{ n m}^{-2} \text{ s}^{-1}$ [7, 8], which is due to cosmic ray interactions with the air and ground, is competitive with, and sometimes dominates, the signal arising

from special nuclear material. The creation of neutron background depends upon atomic number, and this further complicates detection of a SNM source, as the background due to cosmic ray interactions at an air/iron interface (shipping container) is $\sim 770 \text{ n m}^{-2} \text{ s}^{-1}$ [8]. When compared to an unmoderated, unshielded hypothetical mass of 5 kg of 94% enriched ^{239}Pu (weapons grade) at a distance of 3 m, which would have an isotropic neutron flux of $\sim 3700 \text{ n m}^{-2} \text{ s}^{-1}$, the neutron background clearly affects the detection process for nuclear material at US ports of entry.

Most radiation detectors operate using the same basic principles; radiation enters a detection region and interacts with the detector material, which ultimately liberates electrons that are collected and measured as a current or light output (scintillation). Therefore, the challenge of detecting radiation from special nuclear material requires an understanding of the nuclear decay modes of the fissile isotopes used for nuclear weapons, as well as how radiation, produced via these decay modes, interacts with matter.

Uranium-235 (^{235}U) and plutonium-239 (^{239}Pu) are the commonly used isotopes for nuclear weapons. Uranium is a metal that is obtained by mining from natural deposits, and contains approximately 99.3% Uranium-238 (^{238}U) and 0.7% ^{235}U . Following mining, the uranium is enriched to approximately 80% ^{235}U , through a series of chemical and mechanical processes, at which point the material is considered suitable for weapon production.

Unlike uranium, only trace amounts of plutonium exist in nature. Therefore, ^{239}Pu is synthesized in a nuclear reactor using uranium and neutrons (n), via beta decay (β^-) with neptunium (Np) as an intermediate, in the reaction



which inevitably produces ^{240}Pu and ^{241}Pu via the reactions



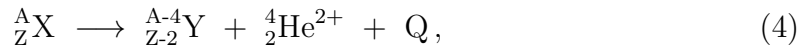
Table 1 displays several properties of the SNM isotopes from reactions (1), (2), and (3), and highlights several concerns regarding their timely and accurate detection. First, a long half life, or low intrinsic radioactivity, requires extended collection

Table 1. Selected properties of common special nuclear material.

Isotope	Half Life [years]	Primary Decay Mode	Spontaneous Fission Neutron Emission Rate [†] [n/kg-sec]
^{235}U	7.0×10^8	α	1.04×10^{-2}
^{238}U	4.5×10^9	α	12.6
^{239}Pu	2.4×10^4	α	19.9
^{240}Pu	6.5×10^3	α	1.38×10^6
^{241}Pu	14.4	α	2.20×10^2

[†] Based upon average neutrons per fission of 2.44 and 2.89 for uranium and plutonium, respectively [9].

times to successfully observe the infrequent decay events for the isotopes of concern. Second, the dominant decay mode for these isotopes is alpha (α) decay, described by the emission of a doubly-ionized helium atom (${}^4_2\text{He}^{2+}$), or alpha particle, as



where A represents the atomic mass or the sum of protons and neutrons, Z is the atomic number or the number of protons, X and Y are the reactant and product isotopes, respectively, and Q is the reaction energy. In theory, Q is calculated from the ground state mass-energies of the reactant, product, and alpha particle and by

conservation of energy and momentum. The reaction energy is distributed between the product isotope and the alpha particle, with the alpha particle receiving nearly all of the reaction energy. In practice, however, a distribution of alpha particle energies exists, due to the fact that the reactant isotope or the product isotope may be in an excited or meta-stable state prior to or immediately following the nuclear decay. These distributions are well-known and tabulated for easy reference in the *Chart of the Nuclides* [10] or online via the National Nuclear Data Center (NNDC) [11], as two examples. For the SNM of greatest concern, the most probable alpha particle energies for ^{235}U and ^{239}Pu are 4.39 MeV and 5.15 MeV, respectively [11].

It should be noted that the term “special nuclear material” in these discussions implies that the mass of material is composed of isotopes from Table 1 and contains at least a small percentage of the isotope ^{240}Pu . This assumption is required because, of the isotopes listed in Table 1, only ^{240}Pu has a spontaneous fission neutron emission rate that exceeds the background neutron emission from cosmic ray interactions. In fact, although not explicitly stated earlier, the unmoderated, unshielded hypothetical mass of 5 kg of weapons grade material used for comparison with neutron background contained 5% or 250 g of the isotope ^{240}Pu .

In addition to alpha particles, meta-stable state decay and spontaneous fission reactions yield gamma rays, electrons, and neutrons. The material response to charged particles and photons classify both as ionizing radiation, due to their interaction with atomic electrons. On the other hand, neutrons are classified as non-ionizing radiation, due to the fact that their interaction is with the nucleus of the absorbing material. Thus, an understanding of both ionizing radiation and non-ionizing radiation interactions with matter is required in order to determine the feasibility to identify special nuclear material via the radiation interaction mechanisms.

1.2.2 Ionizing Radiation Interactions with Matter.

Heavy charged particles, such as the alpha particle, interact with matter primarily through Coulomb forces between their positive charge and the negative charge of the orbital electrons within the absorber atoms. In any single encounter, the electron experiences an impulse from the attractive Coulomb force as the particle passes in its vicinity. Depending on the proximity of the interaction, this impulse may be sufficient either to raise the electron to a higher-lying shell within the absorber (excitation) or to completely remove the electron from the atom (ionization). In either case, the energy that is transferred to the electron must come at the expense of the charged particle, and its velocity is therefore decreased as a result of the encounter. At any given time, a charged particle interacts with many electrons, so the net effect is to decrease its velocity continuously until the particle is stopped at its depth of penetration in the material, or range.

The alpha particle energies mentioned in the previous paragraph have approximate ranges, in air, of less than 4 cm [12]. For materials with higher atomic numbers, that value is significantly reduced; for example, the same particles would travel less than 100 μm in silicon [12]. Therefore, the primary decay mechanism for common nuclear weapon isotopes is easily shielded and does not facilitate successful identification of special nuclear material.

As mentioned earlier, a product isotope may be in an excited or meta-stable state following nuclear decay, and subsequent decay to a stable ground state is often accompanied by gamma ray emission. As with alpha particle decay, distributions of characteristic gamma ray energies are well-known and tabulated. For example, the approximate ranges of characteristic gamma ray energies associated with ^{235}U and ^{239}Pu are 110–280 keV and 40–400 keV, respectively [11]. Given these energy ranges, the dominant photon interaction mechanisms are the photoelectric effect and

Compton scattering, whereby electrons receive the partial or complete transfer of the gamma ray photon energy. The resulting interactions exponentially attenuate the gamma ray photons, as functions of photon energy, interaction material density, and interaction material thickness. Specifically, a narrow beam of monoenergetic photons with an incident intensity I_0 , penetrating a layer of material with thickness x and density ρ , will emerge with intensity I given by the exponential attenuation law

$$I(x) = I_0 e^{-\left(\frac{\mu}{\rho}\right)\rho x}, \quad (5)$$

where μ/ρ is the photon mass attenuation coefficient, which is a function of incident photon energy and absorber material density. These experimentally determined coefficients are well-known and tabulated. As an example, the National Institute of Standards and Technology (NIST) provides a comprehensive, electronic listing [13].

Using (5) and appropriate values from the NIST database, the highest gamma ray energies associated with SNM isotopes listed in Table 1 require less than a 3 cm thickness of lead shielding to attenuate 99.9% of emitted gamma ray photons; therefore, gamma rays are easily shielded. Furthermore, distinguishing SNM emitted gammas from the background continuum of gamma rays and X-rays from naturally occurring terrestrial and cosmic radiation sources compounds the problem. Hence, identification of special nuclear material from either characteristic alpha decay or characteristic gamma ray emission is problematic.

Electrons and positrons are primarily created following the SNM fission product beta (β) decay mechanisms of

$$n \longrightarrow p + \beta^- + \bar{\nu}, \quad (6)$$

and

$$p \longrightarrow n + \beta^+ + \nu, \quad (7)$$

where $\bar{\nu}$ and ν are the antineutrino and neutrino particles. The beta decay-produced charged particles offer little potential for identifying SNM. Analysis of the particles' interactions with matter shows that collisional and radiative energy losses yield beta particle ranges that are approximately 100 times larger than those for an energetically equivalent alpha particle, but are still easily attenuated by minimal shielding material. Thus, neutron emission detection is the remaining choice to identify SNM via radiation detection.

1.2.3 Non-ionizing Radiation Interactions with Matter.

Due to their charge neutrality, neutrons interact with the nucleus, as opposed to with the atomic electrons, and the mechanisms that govern their attenuation in a material differ slightly from those associated with ionizing radiation. Typically, a neutron will lose energy in material through a series of, for the most part, elastic scattering events. As neutron energy decreases, scattering continues, but the likelihood of its capture by a nucleus generally increases. First, we shall consider neutron production by special nuclear material, followed by a more detailed discussion of neutron interaction mechanisms.

Recall that Table 1 listed spontaneous fission neutron emission rates for common nuclear weapon materials. Spontaneous fission is a form of radioactive decay characteristic of very heavy isotopes. As the atomic number, Z , and atomic mass, A , of an isotope increase, the sensitive balance between the nuclear binding energy and the Coulombic repulsion between the protons within the nucleus may be disrupted, at which point it becomes energetically possible for the nucleus to spontaneously divide into two smaller fragments (fission). A quantum mechanical analysis of the

semi-empirical mass formula (SEMF) for nuclear binding energy dictates that this phenomenon occurs, approximately, for isotopes in the limiting condition [14]

$$\frac{Z^2}{A} = \frac{2 a_s}{a_c} \approx 49, \quad (8)$$

where a_s and a_c are the surface and Coulomb SEMF correction factors to the liquid drop binding energy model. The spontaneous fission neutron emission rate, \dot{n}_{SF} , listed in Table 1, is calculated as

$$\dot{n}_{SF} = \left(\frac{\ln 2}{t_{1/2}} \right) \left(\frac{m N_{AV}}{M_{AW}} \right) \mathcal{P}_{SF} \bar{n}_{\text{fission}}, \quad (9)$$

where $t_{1/2}$ is the isotope half-life, m is the isotope mass, N_{AV} is Avogadro's number, M_{AW} is the isotope molar mass, \mathcal{P}_{SF} is the isotope probability of spontaneous fission, and \bar{n}_{fission} is the average neutrons emitted per fission event. These data are accessible from NNDC, with the exception of the \bar{n}_{fission} data, which are indicated in the Table 1 footnote via [9].

In addition to spontaneous fission neutrons, neutrons may be liberated by fission that is induced from neutrons originating from terrestrial, cosmic, or other radioactive sources. In general, the prompt fission responses of the SNM of interest follow the reactions



As with alpha particle and gamma ray decay, the reaction energies and their distributions are tabulated for the nuclear weapon material isotopes, although explicit calculation of the reaction energies is accomplished using the mass energies of the product and reactants, as done in (4).

It should be noted that the fission fragment pair produced in reaction (10) does

not always consist of the same nuclides, even for the case of induced fission with identical target nuclei and identical bombarding neutron energy. Instead, a range of pairs is possible, subject to the requirement that the total number of nucleons is conserved, although experimentally determined maxima exist at $A = 95$ and $A = 140$ for ^{235}U . Further experimental analysis indicates that the average value of prompt fission energy for all possible fission fragment pairs is 180 MeV for ^{235}U and 185 MeV for ^{239}Pu and that these energies are distributed among the products according to Table 2. Therefore, the average number of neutrons emitted per fission event (2–3) from re-

Table 2. Prompt fission energy distribution [9].

Energy Form	^{235}U	^{239}Pu
Fission Fragment Kinetic Energy	168	172
Neutron Kinetic Energy	5	6
Prompt Gamma Energy	7	7
Total Prompt Energy (MeV)	180	185

action (10) and the neutron kinetic energy allocation from Table 2 indicates that the average neutron energy resulting from ^{235}U and ^{239}Pu fission is approximately 2 MeV; however, the most probable neutron energy is approximately 1.5 MeV [9].

The interaction of these neutrons with matter and the likelihood of identifying SNM via neutron detection must be examined next. A neutron’s ability to generate an electronic signal in a detector requires conversion of the neutron into a charged particle through a secondary reaction, and the likelihood, or probability, of this conversion is governed by nuclear cross sections.

The concept of a microscopic nuclear cross section σ is that the effective size of a nucleus should be proportional to the probability that an incident particle would react with it. This probability is expressed conventionally in terms of the barn (10^{-28} m^2) for each type of interaction. For example, each isotope will have an elastic scattering

cross section, a radiative capture cross section, and so on, each of which will be a function of the neutron energy. The hierarchy of microscopic cross sections used to determine neutron interaction rates is shown in Figure 1, courtesy of [15].

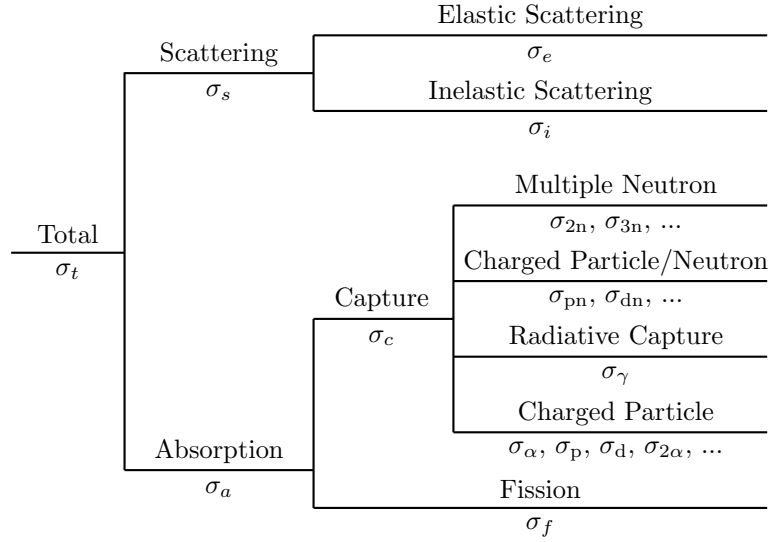


Figure 1. Microscopic cross section hierarchy used to calculate neutron interaction rates. Adapted from [15].

When multiplied by the the number of nuclei per unit volume N , the microscopic cross section is converted to a macroscopic cross section, Σ , then as

$$\Sigma = N \sigma, \quad (11)$$

which has dimensions of inverse length, and represents physically the probability per unit path length for the specific process described by the microscopic cross section. Combining the processes for each interaction

$$\Sigma_{\text{total}} = \Sigma_{\text{scatter}} + \Sigma_{\text{rad. capture}} + \dots \quad (12)$$

gives the resulting total macroscopic cross section, or the probability per unit path

length that any interaction type will occur. Consequently, the neutron flux-dependent volumetric reaction rate, or reaction rate density \dot{R}_{vol} is directly proportional to Σ and is calculated as

$$\dot{R}_{\text{vol}} = \Sigma \Phi, \quad (13)$$

where Φ is the neutron flux.

As with photons, and in a simplistic, one-dimensional analysis, if a narrow beam neutron experiment were conducted, the entering neutron flux Φ_0 would attenuate exponentially [12, 15] with absorber thickness x as

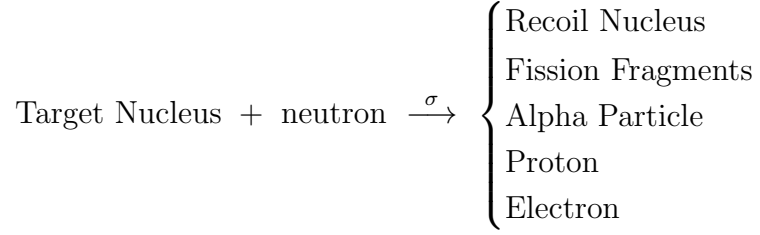
$$\Phi(x) = \Phi_0 e^{-\Sigma_{\text{total}} x}. \quad (14)$$

Rigorous neutron attenuation analysis requires replacing the simple position-dependent neutron flux $\Phi(x)$ considered in (14) with a multivariable counterpart described by the Boltzmann neutron transport equation. However, full analysis of the Boltzmann equation is unwarranted here, as a simplistic treatment of neutron flux yields a similar conclusion. That is, analysis of (14) with appropriate cross section data would show that neutrons produced by fission reactions possess sufficient energy to escape most typical shielding materials with minimal attenuation such that the neutron flux value resulting from the assumptions of an unmoderated, unshielded SNM mass, discussed in Section 1.2.1, is a reasonable initial estimate.

Therefore, neutrons offer the most accurate and efficient method to identify special nuclear material. However, while SNM identification via neutron detection appears favorable from a physical standpoint, several engineering design considerations must be addressed.

1.3 General Neutron Detector Design Considerations

A neutron's ability to generate an electronic signal in a detector requires conversion of the neutron into a charged particle through a secondary reaction, as shown below [12].



However, these neutron induced secondary reactions occur only with appreciable probability (cross section) in the thermal neutron energy range, about 0.025 eV at room temperature. Therefore, accurate and efficient neutron detection requires a careful combination of moderator, conversion, and detector materials, as shown hypothetically in Figure 2, that successfully reduces the energy of a fast neutron to

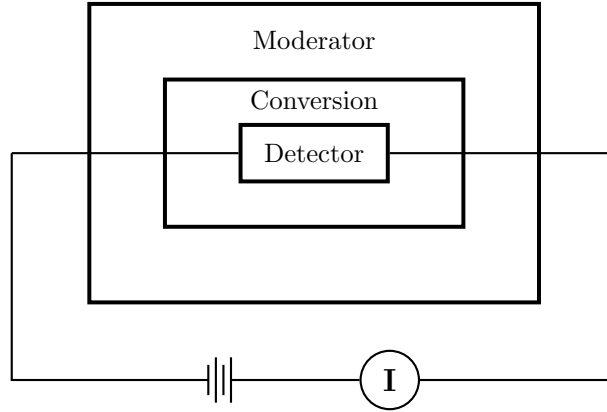


Figure 2. General schematic (top view) of a hypothetical solid state semiconducting device capable of neutron detection.

the thermal range, converts thermal neutrons to charged particles, and responds favorably to this ionizing radiation by emitting and collecting charged particles or

photons.

Neutron opacity, or complete neutron capture, within the conversion volume or layer presents one design challenge. If the moderator and conversion layers are too thin, neutrons are not captured and converted to charged particles; if the layers are too thick, the reaction products fail to reach the active layer of the detector. Similarly, the distance traveled by the charged particle reaction products has important consequences within the detector. Specifically, in order to capture the full kinetic energy of the products, the detector must be designed with an active volume that is large enough to fully stop the products.

Discrimination between neutron-induced and gamma-induced reactions in a detector is another consideration. If the active layer of the detector is much smaller than the mean free path of gamma rays in the material, then the detector would be insensitive to these photons. However, if the gamma mean free path, which is a function of material density and Z , or the number of electrons per atom, approaches the active layer width of the detector, the neutron and gamma signals may overlap, and detection via gross neutron counting can be problematic.

Of course, efficient neutron capture and conversion are inadequate if the neutron conversion reaction products cannot produce electron-hole pairs for efficient collection. In general, the charge created from a single ionizing radiation interaction is proportional to the energy lost by an ionizing agent E_{ion} in the material, at the cost of approximately $3E_g$ per electron-hole pair [16], where E_g is the bandgap energy. Assuming full energy deposition of the ionizing radiation, the maximum charge created in a single event is approximated as

$$Q_{\text{max}} = \frac{E_{\text{ion}}}{3E_g} \times (1.6 \times 10^{-19}) \quad [\text{C}]. \quad (15)$$

The delicate balance of material composition and dimensions must be coupled

with a device design that maximizes the electronic signal, such that the generated charge exceeds the intrinsic noise level of the charge-sensitive commercial preamplifier-amplifier combination. In short, the cross section for the neutron conversion reaction must be as large as possible so that efficient detectors can be built with small dimensions. If the detection medium is a solid, this requirement is typically achieved because the ranges of the ionizing radiation reaction products in solid materials are on the order of 10^3 less than products of equivalent energy in a gas detection medium. Hence, the ranges of these products in gas-based detection systems can be significant compared to the detector dimensions and can prevent full collection of the products.

Common neutron detection materials include boron-10 (^{10}B), lithium-6 (^6Li), and helium-3 (^3He), which are configured in designs that include proportional counters, scintillators, thermoluminescent dosimeters, solid state conversion layers, and neutron absorbing solid state layers. Proportional counters employ gas as the detection medium and, by design, tend to be large compared to the remaining designs, which use solid detection materials. Furthermore, limited production of ^3He , caused in combination by the 1988 closure of the Savannah River production facility and the post-9/11 growth in security-related neutron detectors [17], has elevated alternatives to ^3He as a top priority for the Department of Homeland Security [17].

Currently, most commercially available solid state neutron detectors are based on lithium iodide scintillation. Scintillators and thermoluminescent dosimeters (TLD), shown in Figures 3(a) and 3(b), respectively, consist of neutron absorbing materials that decay into ionizing radiation reaction products and create electron-hole pairs. Scintillation detectors and thermoluminescent dosimeters are similar in that both use solid state materials that incorporate dopants, which capture the electrons and holes and then measure the light output, via a photomultiplier tube (PMT), when the electrons and holes recombine. However, while scintillators facilitate rapid recombination of electrons and holes, thermoluminescent dosimeters require heating in

order to de-trap the electron-hole pairs.

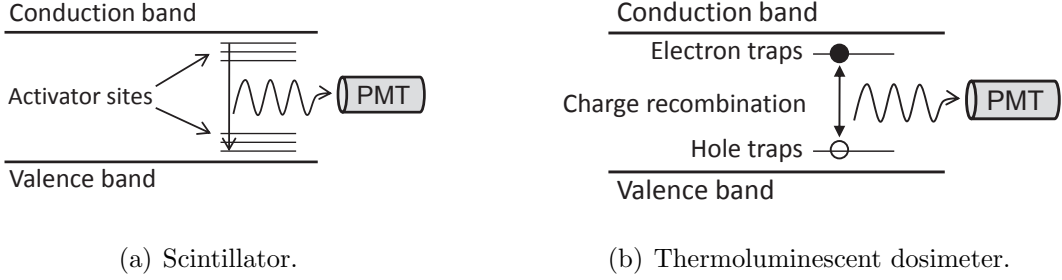


Figure 3. Scintillation detector schematics.

Solid state neutron detectors may also take the form of $p - n$ junction or Schottky heterostructures, and are separated into two subclasses. Indirect conversion, or thin-film-coated [18, 19], neutron detectors, as depicted in Figure 4(a), use neutron absorbing material to generate ionizing radiation reaction products which interact with adjacent conventional semiconductor devices. Clever planar and stack designs are used to maximize the surface area between conversion materials and space charge. Direct conversion, or solid-form [18, 19] neutron detectors, shown in Figure 4(b) are fabricated from semiconductors doped with neutron conversion material. Unconverted reaction products are minimized, and higher theoretical efficiencies are possible. While clever designs are not required, maturity of materials and an understanding of the physical and electronic properties of the heterostructure materials are the limiting factors in direct conversion designs [18–20].

Figure 5 shows the detector efficiencies for several common, thin-film semiconductor diodes, and indicates that the most efficient diode, containing an enriched ^{10}B layer, requires an active volume thickness of approximately $40\ \mu\text{m}$ for optimal performance, whereas the other designs require thicknesses between several hundred microns and over one centimeter to achieve comparable performance. Device designs that minimize the conversion layer thickness are important for several reasons. First, the ranges and mean free paths of charged particles and photons created from

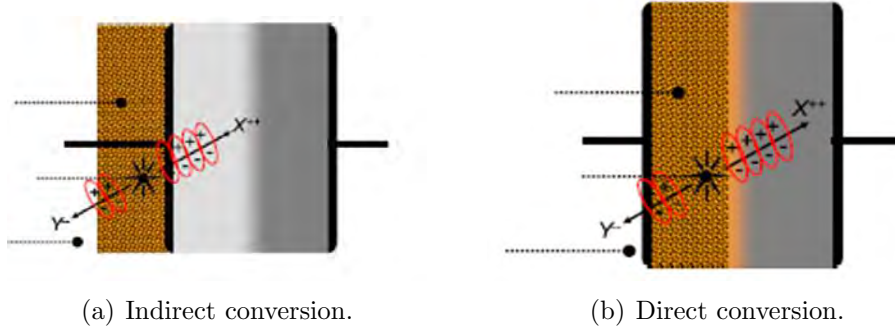


Figure 4. Solid state neutron conversion detector schematics. Adapted from [19].

neutron conversion decrease with increased thickness. Thus, charge collection efficiency is potentially reduced and the ability to discriminate between neutron and gamma interactions is complicated. Second, thicker films are more costly and potentially more difficult to grow and fabricate into devices, as compared to thinner films. Thin-film-coated semiconductor devices have been investigated for thermal neutron detection by various research groups [18,21–40], all of which have used ^{10}B , ^6Li , ^6LiF , Cd , U , or Gd coatings as the neutron reactive layer, although the most successful conversion layer devices are based on ^{10}B enriched boron coatings.

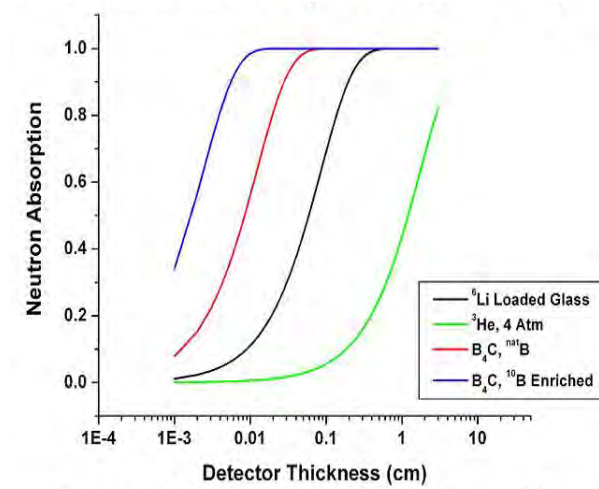


Figure 5. Neutron absorption (detection and capture efficiencies) as a function of detector thickness.

As shown in Figure 6, gadolinium-157 (^{157}Gd) possesses a thermal neutron cap-

ture cross section that is nearly two orders of magnitude larger than that of ^{10}B , and is the highest of all known isotopes, thus making it a potentially favorable choice for neutron detection. Moreover, due to the unique energy dependence of its cross section, ^{157}Gd maintains its utility for thermal neutron capture and detection at neutron energies in the range of 200–300 meV, as compared with approximately 25 meV for the common neutron absorbers. Finally, the secondary conversion reactions result in the emission of ionizing radiation, to include gamma-ray and characteristic X-ray photons, as well as Auger and internal conversion electrons. When absorbed by a detector material, these ionizing radiation photons and charged particles can ultimately provide reliable indication of the initial neutron absorption. From a neutron

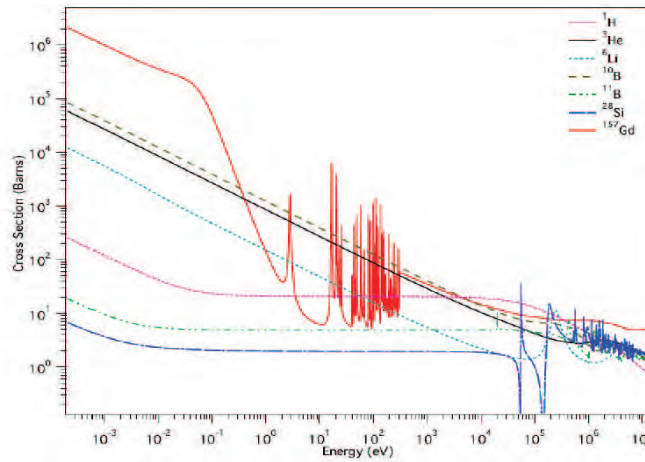


Figure 6. Energy dependent neutron capture cross sections for various materials.

detector device standpoint, these favorable properties indicate that neutron opacity in Gd occurs for smaller film thicknesses than in the other materials shown in Figure 6. It follows that the thinner Gd films are transparent to photons at a lower energy threshold than the remaining materials. This favorable combination of neutron opacity and gamma discrimination for Gd films offers the likelihood that a signal generated from a Gd-based neutron detector could be definitively correlated with

neutron emission from a radioactive source, as opposed to gamma decay. Several researchers [21–23] have incorporated gadolinium in semiconductor device neutron detectors with varying results. However, there remains great opportunity for continued exploration and development of high-quality Gd doped semiconductor materials and neutron detector device architectures.

1.4 Research Objectives and Overview

Semiconductors that incorporate large neutron absorption cross section materials, such as ^{157}Gd , are gaining attention, despite the relative immaturity of their development. Gallium nitride (GaN) is one semiconductor material which, by itself, has attained considerable recognition over the past two decades. Its favorable properties as a device material include a large bandgap (~ 3.4 eV), thermal and chemical stability, and high carrier mobility, ensuring that GaN-based designs are robust in the presence of fluctuating temperature and ionizing radiation environments. In the past, successful incorporation of rare earth (RE) dopants, to include Gd, into GaN structures had been limited, but during the past decade, rare earth doped semiconductors have generated considerable attention for their application in new optoelectronic devices [41–44]. Despite the increased attention, incomplete understanding of the physical and electronic properties of these materials classifies rare earth doped GaN heterostructures as non-conventional, as compared to silicon-based devices. It is therefore of considerable interest to know whether even low concentrations of a rare earth in a GaN host can alter the surface electronic structure. With these considerations in mind, investigations of the surface electronic structure and interface properties of $\text{RE}_x\text{Ga}_{1-x}\text{N}$ ($\text{RE} = \text{Gd}, \text{Er}, \text{Yb}$) semiconductors are necessary in order to advance the scientific community’s knowledge, and to determine the viability of these materials in neutron detection heterostructures.

To that end, systematic studies of these rare earth doped GaN thin films were

conducted over a period of 20 months in this research. Specifically, the research was designed to answer several questions, to include:

- (1) Can rare earth dopants be incorporated into a GaN lattice using various epitaxial growth techniques?
- (2) Is the location of the rare earth dopant in the GaN lattice classified as substitutional or interstitial?
- (3) Where are the rare earth dopant $4f$ electronic levels located within the valence band of rare earth doped GaN thin films?
- (4) How does the Schottky barrier height at the metal to rare earth doped GaN thin film interface compare with undoped GaN interfaces?
- (5) What does fundamental nuclear and semiconductor physics predict about the viability of gadolinium as a neutron detection material?

First, temperature dependent X-ray photoemission spectroscopy (XPS) studies of Yb doped GaN (GaN:Yb) were conducted in order to determine the effective surface Debye temperature, and concluded that the rare earth dopant occupied a substitutional Ga site within the GaN lattice, as had been previously reported [41,42].

Armed with confidence that the epitaxial growth process produced thin film samples with rare dopants incorporated successfully into the GaN lattice, resonant photoemission studies of several rare earth dopants (Gd, Er, Yb) in GaN were conducted next. The key value of resonant photoemission is to probe what valence bands of the semiconductors have strong $4f$ and/or rare earth weight [35,45,46]. The value in studying the resonant photoemission process of a semiconductor with several different rare earths is that while each is likely to dope the semiconductor in a similar fashion, the resonant enhancement of the valence band will occur at different photon energies. These studies concluded that the placement of the occupied Gd, Er and Yb $4f$ levels were more at the bottom of the valence band than predicted by theory. This suggests that photons emitted from intra-atomic $f-f$ transitions may

be more energetic or ‘blue’ than predicted by many theoretical models, which has implications for the physics, device fabrication, and engineering communities.

Next, device fabrication and neutron detector applications were explored more carefully by measuring the Schottky barrier heights at the gold to rare earth doped GaN interface for the Gd, Er, and Yb dopants via ultraviolet photoemission spectroscopy. The value in studying Schottky barrier heights is as follows. Heterostructure diodes that function as radiation detectors are reverse biased to minimize current flow through the device; thus, current is limited to leakage only. Under reverse bias, the depletion region, which correlates directly with the radiation-induced charge collection volume, widens with increasing reverse voltage. Despite efforts to limit current flow due to leakage, and maximize the charge collection volume, the generated signal due to radiation-induced currents can prove difficult to detect above noise due to leakage currents. To alleviate this obstacle, blocking or Schottky contacts are often used to reduce leakage currents and enhance the signal-to-noise ratio in the radiation detector device architecture.

The completed Schottky barrier studies discovered larger (25-55%) barrier heights at the metal to rare earth doped GaN interface than at interfaces with undoped GaN. These results were uniform for all of the rare earths studied, and imply further reduction in leakage currents as compared with undoped GaN devices. Moreover, the larger barrier height at the metal to rare earth doped GaN interface means that radiation-induced charge collection volumes are increased, and thus more efficient, over what would be the case in pure GaN devices.

Finally, the utility of gadolinium as a neutron detection material in a hypothetical direct-conversion $p - n$ homojunction diode was examined using fundamental nuclear and semiconductor physics. The charge produced in a Gd-based semiconductor by an internal conversion electron created from ^{157}Gd neutron capture was found to approach the intrinsic noise level of commercial preamplifiers required for

pulse height analysis. Neutron capture efficiency was shown to be maximized with Gd-layer thickness, and the bias-dependent depletion width of the Gd-based diode to the full range of the internal conversion electrons ($\sim 25\text{ }\mu\text{m}$) was considered for low power operation.

These preliminary results are promising, but more work is needed to fully understand the material interfaces and their implications for full device fabrication.

References

- [1] C. C. Kelly, *Oppenheimer and the Manhattan Project: Insights into J. Robert Oppenheimer, "Father of the Atomic Bomb"*. World Scientific Publishing Company Inc, 2006.
- [2] A. Kingsbury, "History's Troubling Lessons," *U.S. News and World Report*, February 26, 2007.
- [3] M. P. Unterweger and L. S. Pibida, "Advances in radiation detection technologies for responders," *Health Physics*, vol. 89, no. 5, p. 485, 2005.
- [4] "Radiation Detection at US Ports and Borders," *Instrument Business Outlook*, October 31, 2006.
- [5] "Secretary Napolitano Announces Full Deployment of Radiation Scanning Technology to the Northern Border Ahead of Schedule," Department of Homeland Security Press Release, November 5, 2009, online at: http://www.dhs.gov/ynews/releases/pr_1257454349707.shtm.
- [6] "Nuclear Posture Review Report," United States Department of Defense, April 2010, online at http://www.defense.gov/npr/docs/2010_nuclear_posture_review_report.pdf.
- [7] M. S. Gordon, P. Goldhagen, K. P. Rodbell, T. H. Zabel, H. H. K. Tang, J. M. Clem, and P. Bailey, "Measurement of the flux and energy spectrum of cosmic-ray induced neutrons on the ground," *IEEE Transactions on Nuclear Science*, vol. 51, no. 6, pp. 3427–3434, 2004.
- [8] R. T. Kouzes, J. H. Ely, A. Seifert, E. R. Siciliano, D. R. Weier, L. K. Windsor, M. L. Woodring, J. Borgardt, E. Buckley, and E. Flumerfelt, "Cosmic-ray-induced ship-effect neutron measurements and implications for cargo scanning at

- borders,” *Nuclear Instruments and Methods in Physics Research Section A: Accelerators, Spectrometers, Detectors and Associated Equipment*, vol. 587, no. 1, pp. 89–100, 2008.
- [9] C. J. Bridgman, *Introduction to the Physics of Nuclear Weapons Effects*. Fort Belvoir, VA: Defense Threat Reduction Agency, 2001, vol. 8725.
 - [10] J. R. Parrington, H. D. Knox, S. L. Breneman, E. M. Baum, and F. Feiner, *Nuclides and Isotopes, Chart of the Nuclides*. San Jose, California: General Electric Company and KAPL, 1996, vol. 233705.
 - [11] “Chart of Nuclides,” National Nuclear Data Center, Brookhaven National Laboratory, online at: <http://www.nndc.bnl.gov>.
 - [12] G. F. Knoll, *Radiation Detection and Measurement*. Hoboken, NJ: John Wiley and Sons, 2000.
 - [13] “Tables of X-Ray Mass Attenuation Coefficients,” National Institute of Standards and Technology, online at: <http://www.nist.gov/physlab/data/xraycoef/index.cfm>.
 - [14] J. S. Lilley, *Nuclear Physics*. Hoboken, NJ: John Wiley and Sons, 2001.
 - [15] R. A. Knief, *Nuclear Engineering: Theory and Technology of Commercial Nuclear Power*. Taylor & Francis, 1992.
 - [16] C. A. Klein, “Bandgap dependence and related features of radiation ionization energies in semiconductors,” *Journal of Applied Physics*, vol. 39, no. 4, pp. 2029–2038, 1968.
 - [17] D. Kramer, “DOE begins rationing helium-3,” *Physics Today*, vol. 63, p. 22, 2010.
 - [18] D. S. McGregor, R. T. Klann, H. K. Gersch, and Y. H. Yang, “Thin-film-coated bulk GaAs detectors for thermal and fast neutron measurements,” *Nuclear Instruments and Methods in Physics Research Section A: Accelerators, Spectrometers, Detectors and Associated Equipment*, vol. 466, no. 1, pp. 126–141, 2001.
 - [19] A. N. Caruso, “The physics of solid-state neutron detector materials and geometries,” *Journal of Physics: Condensed Matter*, vol. 22, p. 443201, 2010.
 - [20] C. Lundstedt, A. Harken, E. Day, B. W. Robertson, and S. Adenwalla, “Modeling solid-state boron carbide low energy neutron detectors,” *Nuclear Instruments and Methods in Physics Research Section A: Accelerators, Spectrometers, Detectors and Associated Equipment*, vol. 562, no. 1, pp. 380–388, 2006.

- [21] A. Miresghhi, G. Cho, J. S. Drewery, W. S. Hong, T. Jing, H. Lee, S. N. Kaplan, and V. Perez-Mendez, "High efficiency neutron sensitive amorphous silicon pixel detectors," *IEEE Transactions on Nuclear Science*, vol. 41, no. 4 Part 1, pp. 915–921, 1994.
- [22] T. Aoyama, Y. Oka, K. Honda, and C. Mori, "A neutron detector using silicon PIN photodiodes for personal neutron dosimetry," *Nuclear Instruments and Methods in Physics Research Section A: Accelerators, Spectrometers, Detectors and Associated Equipment*, vol. 314, no. 3, pp. 590–594, 1992.
- [23] I. Ketsman, Y. B. Losovyj, A. Sokolov, J. Tang, Z. Wang, K. D. Belashchenko, and P. A. Dowben, "The n -type Gd-doped HfO_2 to silicon heterojunction diode," *Applied Physics A: Materials Science & Processing*, vol. 89, no. 2, pp. 489–492, 2007.
- [24] A. J. Peurrung, "Recent developments in neutron detection," *Nuclear Instruments and Methods in Physics Research Section A: Accelerators, Spectrometers, Detectors and Associated Equipment*, vol. 443, no. 2-3, pp. 400–415, 2000.
- [25] Z. W. Bell, D. A. Carpenter, S. S. Cristy, V. E. Lamberti, A. Burger, B. F. Woodfield, T. Niedermayr, I. D. Hau, S. E. Labov, and S. Friedrich, "Neutron detection with cryogenics and semiconductors," *Physica Status Solidi C*, vol. 2, no. 5, pp. 1592–1605, 2005.
- [26] D. S. McGregor and K. Shultis, "Spectral identification of thin-film-coated and solid-form semiconductor neutron detectors," *Nuclear Instruments and Methods in Physics Research Section A: Accelerators, Spectrometers, Detectors and Associated Equipment*, vol. 517, no. 1-3, pp. 180–188, 2004.
- [27] D. Schultz, B. Blasy, J. C. Santana, C. Young, J. C. Petrosky, J. W. McClory, D. LaGraffe, J. I. Brand, J. Tang, and W. Wang, "The K-shell Auger electron spectrum of gadolinium obtained using neutron capture in a solid state device," *Journal of Physics D: Applied Physics*, vol. 43, p. 075502, 2010.
- [28] D. S. McGregor, M. F. Ohmes, R. E. Ortiz, A. S. M. S. Ahmed, and J. K. Shultis, "Micro-pocket fission detectors (MPFD) for in-core neutron flux monitoring," *Nuclear Instruments and Methods in Physics Research Section A: Accelerators, Spectrometers, Detectors and Associated Equipment*, vol. 554, no. 1-3, pp. 494–499, 2005.
- [29] D. S. McGregor, M. D. Hammig, Y. H. Yang, H. K. Gersch, and R. T. Klann, "Design considerations for thin film coated semiconductor thermal neutron detectors—I: basics regarding alpha particle emitting neutron reactive films," *Nuclear Instruments and Methods in Physics Research Section A: Accelerators, Spectrometers, Detectors and Associated Equipment*, vol. 500, no. 1-3, pp. 272–308, 2003.

- [30] H. K. Gersch, D. S. McGregor, and P. A. Simpson, "The effect of incremental gamma-ray doses and incremental neutron fluences upon the performance of self-biased ^{10}B -coated high-purity epitaxial GaAs thermal neutron detectors," *Nuclear Instruments and Methods in Physics Research Section A: Accelerators, Spectrometers, Detectors and Associated Equipment*, vol. 489, no. 1-3, pp. 85–98, 2002.
- [31] D. S. McGregor, R. T. Klann, H. K. Gersch, E. Ariesanti, J. D. Sanders, and B. VanDerElzen, "New surface morphology for low stress thin-film-coated thermal neutron detectors," *IEEE Transactions on Nuclear Science*, vol. 49, no. 4 Part 1, pp. 1999–2004, 2002.
- [32] D. S. McGregor, S. M. Vernon, H. K. Gersch, S. M. Markham, S. J. Wojtczuk, and D. K. Wehe, "Self-biased boron-10 coated high-purity epitaxial GaAs thermal neutron detectors," *IEEE Transactions on Nuclear Science*, vol. 47, no. 4 Part 1, pp. 1364–1370, 2000.
- [33] D. S. McGregor, J. T. Lindsay, C. C. Brannon, and R. W. Olsen, "Semi-insulating bulk GaAs thermal neutron imaging arrays," *IEEE Transactions on Nuclear Science*, vol. 43, no. 3, pp. 1357–1364, 1996.
- [34] J. K. Shultis and D. S. McGregor, "Efficiencies of coated and perforated semiconductor neutron detectors," in *2004 IEEE Nuclear Science Symposium Conference Record*, vol. 7, 2004.
- [35] I. Ketsman, Y. B. Losovyj, A. Sokolov, J. Tang, Z. Wang, M. L. Natta, J. I. Brand, and P. A. Dowben, "Gd-doping of HfO_2 ," *Applied Surface Science*, vol. 254, no. 14, pp. 4308–4312, 2008.
- [36] Y. B. Losovyj, I. Ketsman, A. Sokolov, K. D. Belashchenko, P. A. Dowben, J. Tang, and Z. Wang, "The electronic structure change with Gd doping of HfO on silicon," *Applied Physics Letters*, vol. 91, p. 132908, 2007.
- [37] A. N. Caruso, P. A. Dowben, S. Balkir, N. Schemm, K. Osberg, R. W. Fairchild, O. B. Flores, S. Balaz, and A. D. Harken, "The all boron carbide diode neutron detector: Comparison with theory," *Materials Science and Engineering: B*, vol. 135, no. 2, pp. 129–133, 2006.
- [38] C. M. Young, "Gadolinium Oxide / Silicon Thin Film Heterojunction Solid-State Neutron Detector," Master's thesis, Air Force Institute of Technology, 2010.
- [39] B. R. Thomas, "Neutron Detection Using Gadolinium-Based Diodes," Master's thesis, Air Force Institute of Technology, 2011.
- [40] J. E. Bevins, "Characterization of a Boron Carbide Heterojunction Neutron Detection," Master's thesis, Air Force Institute of Technology, 2011.

- [41] T. Koubaa, M. Dammak, M. Kammoun, W. M. Jadwisienczak, and H. J. Lozykowski, “Crystal field and Zeeman parameters of substitutional Yb^{3+} ion in GaN,” *Journal of Alloys and Compounds*, vol. 496, no. 1-2, pp. 56–60, 2010.
- [42] T. Koubaa, M. Dammak, M. Kammoun, W. M. Jadwisienczak, H. J. Lozykowski, and A. Anders, “Spectra and energy levels of Yb^{3+} in AlN,” *Journal of Applied Physics*, vol. 106, no. 1, p. 013106, 2009.
- [43] W. M. Jadwisienczak and H. J. Lozykowski, “Optical properties of Yb ions in GaN epilayer,” *Optical Materials*, vol. 23, no. 1-2, pp. 175–181, 2003.
- [44] A. J. Kenyon, “Recent developments in rare-earth doped materials for optoelectronics,” *Progress in Quantum Electronics*, vol. 26, no. 4-5, pp. 225–284, 2002.
- [45] I. Ketsman, Y. B. Losovyj, A. Sokolov, J. Tang, Z. Wang, K. D. Belashchenko, and P. A. Dowben, “The n -type Gd-doped HfO_2 to silicon heterojunction diode,” *Applied Physics A: Materials Science & Processing*, vol. 89, no. 2, pp. 489–492, 2007.
- [46] R. F. Sabirianov, W. N. Mei, J. Lu, Y. Gao, X. C. Zeng, R. D. Bolskar, P. Jeppson, N. Wu, A. N. Caruso, and P. A. Dowben, “Correlation effects and electronic structure of Gd @ C60,” *Journal of Physics: Condensed Matter*, vol. 19, p. 082201, 2007.

II. Theory

This chapter discusses theory pertaining to the experimental techniques used during research, beginning with a general overview of photoelectron spectroscopy. Subsequent sections present applications of the theory, including temperature-dependent photoemission, resonant photoemission, and the photoemission response to metal overlayer deposition. Each technique was used during the research owing to its valuable insight to surface electronic structure. As devices continue to scale smaller, and as rare earth doped GaN optoelectronic devices continue to gain popularity, comprehensive understanding of their material surface properties becomes increasingly valuable to efficient device design and engineering.

2.1 Photoelectron Spectroscopy Models

In a general sense, photoelectron spectroscopy (PES) provides information about occupied states in an atom, molecule, or solid in that the spectroscopic techniques directly measure a system's orbital energies. The theoretical basis behind these techniques is photoemission, described by the photoelectric effect, which was first identified in 1887 by Hertz [2] and subsequently explained by Einstein [3]. Photoemission, depicted for an arbitrary solid in Figure 7, results from incident photon annihilation, which excites an electron from a bound state of a system (atom, molecule, solid) to a continuum state, such as the vacuum. For the process to occur, the photon energy $h\nu$ must be sufficient to provide the electron with enough energy to overcome the work function ϕ and the binding energy E_B of the bound state, such that, in a vacuum, the kinetic energy E_{kin} of a photoelectron is measured as

$$E_{\text{kin}} = h\nu - |E_B| - \phi. \quad (16)$$

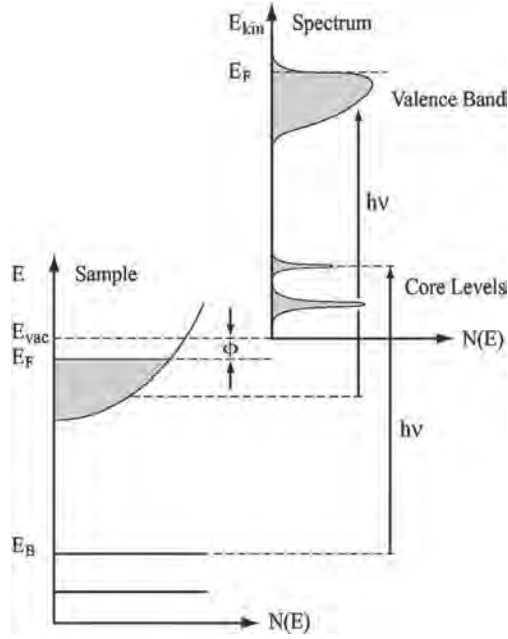


Figure 7. The photoelectron energy distribution produced by incoming photons and measured as a function of the kinetic energy E_{kin} of the photoelectrons (right) is more conveniently expressed in terms of the binding energy E_B (left) when one refers to the density of states inside the solid ($E_B = 0$ at E_F .) Adapted from [1].

Prior to discussing the photoemission techniques relevant to this research, an overview of the two generally accepted models of photoemission is required. The *one-step model* and *three-step model* explain the phenomenon in either a single or a three step process, as their names indicate.

The three-step model, developed by Berglund and Spicer [4], adequately and pedagogically explains the photoemission process as three independent and sequential processes. In the first step, the photon is absorbed locally and an electron is excited. In the second step, this electron travels through the sample to the surface. Finally, in the third step the electron escapes through the surface into the vacuum where it is detected. As expected, the one-step model treats the entire process as a single coherent step, but this model is mathematically rigorous and less conducive to a qualitative understanding of the photoemission process than its multi-step counterpart. Furthermore, although the separation of events is somewhat artificial in that

the entire process should be treated as a single step, the division of the process into three distinct steps yields results that are not very different from the conceptually unwieldy one-step model [1]. Thus, given the adequacy of a three-step model analysis and the unnecessary rigor of a one-step model examination, a detailed discussion of the one-step model is omitted in the interests of clarity and simplicity.

In addition to the three-step model's treatment of photoemission as sequential, independent steps, the model also assumes that the energy distribution of photoelectrons $N(E, h\nu)$ results from a distribution of primary unscattered electrons $N_{\text{pri}}(E, h\nu)$ and a distribution of background secondary electrons $N_{\text{sec}}(E, h\nu)$ that result from one or more scattering events, or

$$N(E, h\nu) = N_{\text{pri}}(E, h\nu) + N_{\text{sec}}(E, h\nu). \quad (17)$$

Furthermore, the primary photoelectron energy distribution results from the convolution of three independent functions, namely the transmission function, the escape function, and the internal energy distribution of photoelectrons N_{int} [5], each of which will be discussed in the following sections.

2.1.1 Optical Excitation of the Electron in the Solid.

The following three-step model theory is summarized from Hüfner [1]. The photocurrent produced in a PES experiment results from the excitation of electrons from an initial energy eigenstate with wave function Ψ_i to a continuum of final states with wave function Ψ_f by a photon field having the vector potential \mathbf{A} , and may be explained using time-dependent perturbation theory. Assuming a small perturbation H' , the transition probability per unit time w between the initial eigenstate Ψ_i and

the final electron state Ψ_f is given by Fermi's golden rule as

$$w \propto \frac{2\pi}{\hbar} |\langle \Psi_f | H' | \Psi_i \rangle|^2 \delta(E_f - E_i - h\nu) \quad (18)$$

where \hbar is Planck's constant divided by 2π , $|\langle \Psi_f | H' | \Psi_i \rangle|^2$ is the square of the transition matrix element of the time-dependent perturbing Hamiltonian operator H' , and the Kronecker delta function $\delta(E_f - E_i - h\nu)$ dictates that the initial and final states of the system must be energetically identical to ensure a non-zero transition probability. It should be noted that w must vary slowly enough to determine time intervals that satisfy the condition of time dependence, yet small enough to classify H' as a small perturbation [6]. Thus, an appropriate expression for the perturbing Hamiltonian H' is required to determine the transition rate and, hence, the internal energy distribution of photoexcited electrons.

In the most general form, the Hamiltonian H' of an electron in an arbitrary electromagnetic field is given by [6]

$$H' = \frac{e}{2mc} \left[(\mathbf{A} \cdot \mathbf{p} + \mathbf{p} \cdot \mathbf{A}) + \left(\frac{e}{c} \right) (\mathbf{A} \cdot \mathbf{A}) \right] - e\varphi, \quad (19)$$

where e and m are the electron mass and charge, respectively, c is the speed of light in a vacuum, \mathbf{A} is the vector potential, \mathbf{p} is the momentum operator $\mathbf{p} = i\hbar\nabla$, and φ is the scalar potential; the scalar potential φ is not to be confused with the work function ϕ . Using the commutation relation

$$[\mathbf{p}, \mathbf{A}] = (\mathbf{p} \cdot \mathbf{A}) - (\mathbf{A} \cdot \mathbf{p}) = -i\hbar(\nabla \cdot \mathbf{A}), \quad (20)$$

the first two terms in equation (19) reduce as

$$(\mathbf{A} \cdot \mathbf{p}) + (\mathbf{p} \cdot \mathbf{A}) = (\mathbf{p} \cdot \mathbf{A}) - (\mathbf{A} \cdot \mathbf{p}) + 2(\mathbf{A} \cdot \mathbf{p}) \quad (21)$$

$$= -i\hbar(\nabla \cdot \mathbf{A}) + 2(\mathbf{A} \cdot \mathbf{p}), \quad (22)$$

and H' can be re-written as

$$H' = \frac{e}{2mc} \left[2(\mathbf{A} \cdot \mathbf{p}) - i\hbar(\nabla \cdot \mathbf{A}) + \left(\frac{e}{c}\right) (\mathbf{A} \cdot \mathbf{A}) \right]. \quad (23)$$

The perturbing Hamiltonian H' in (23) can be simplified further by selecting the Coulomb gauge such that $\nabla \cdot \mathbf{A} = 0$, which is a valid assumption because of translational invariance in the solid [1]. A more physically intuitive justification would be that \mathbf{A} is constant over the atomic dimensions of the solid. For photons of energy $h\nu = 10$ eV one has wavelength $\lambda = 10^3$ Å and can therefore assume, at least for a wide range of experiments, that the wavelength is large compared to atomic distances; thus, \mathbf{A} can be assumed constant. If non-linear, two-photon processes are neglected, then the term $\mathbf{A} \cdot \mathbf{A}$ may also be ignored, and (23) reduces to

$$H' = \frac{e}{mc} (\mathbf{A} \cdot \mathbf{p}). \quad (24)$$

The electronic states in a solid are described by bands, which are typically plotted in the reduced zone scheme. Within this scheme, the bands outside of the first Brillouin zone are folded back into the first zone by adding the appropriate reciprocal lattice vector \mathbf{G} . Thus, in the reduced zone scheme, optical transitions between initial i and final f states are “vertical” such that $\mathbf{k}_f = \mathbf{k}_i$, where \mathbf{k} is the wave vector of the electronic state in the crystal, whereas in the extended zone scheme, $\mathbf{k}_f = \mathbf{k}_i + \mathbf{G}$. Neglecting the momentum of the photon, the internal energy distribution of photoexcited electrons $N_{\text{int}}(E, h\nu)$ where E is the final electron kinetic energy is

determined via summation over the initial and final states. Thus, if the the square of the transition matrix element of the perturbing Hamiltonian operator given in (24) is re-written as $|M_{fi}(\mathbf{k}_i, \mathbf{k}_f)|^2$, then $N_{\text{int}}(E, h\nu)$ is determined by [1]

$$N_{\text{int}}(E, h\nu) \propto \sum_{f,i} |M_{fi}(\mathbf{k}_i, \mathbf{k}_f)|^2 \delta(E_f(\mathbf{k}_f) - E_i(\mathbf{k}_i) - h\nu) \times \delta(E - [E_f(\mathbf{k}_f) - \phi]), \quad (25)$$

where $E_f(\mathbf{k}_f)$ and $E_i(\mathbf{k}_i)$ denote the energies of the final bands $|f, \mathbf{k}_f\rangle$ and the initial bands $|i, \mathbf{k}_i\rangle$, respectively. The first δ -function imposes energy conservation during excitation and the additional δ -function term $\delta(E - [E_f(\mathbf{k}_f) - \phi])$ accounts for the fact that only photoemitted electrons with an energy above the vacuum level ϕ can be experimentally detected. In other words, the kinetic energy measured outside the sample equals the final state energy inside minus the work function, as originally shown in (16).

2.1.2 Transport of the Electron to the Surface.

Following optical electronic excitation, scattering mechanisms, dominated by electron-electron interactions, reduce the number of photoexcited electrons that reach the sample surface with energy $E_f(\mathbf{k}_f)$. Photoelectrons that avoid these interactions during transport to the surface retain their momentum and energy and increase the likelihood of escape. If the scattering frequency $1/\tau$, where τ is the electron lifetime, is isotropic and dependent on E only, then the electron inelastic mean free path λ is directly proportional to the probability of successful transport to the surface such that

$$\lambda(E, k) = \tau v_g = \left(\frac{\tau}{\hbar}\right) \frac{dE}{dk}, \quad (26)$$

where v_g is the group velocity in the final state.

Berglund and Spicer [4] formulated a classical treatment of electron transport described by the transmission coefficient $d(E, k)$ as

$$d(E, k) \approx \frac{\alpha\lambda}{1 + \alpha\lambda}, \quad (27)$$

where α is the optical absorption coefficient of the photon and has units of inverse length. Qualitatively, α^{-1} describes the penetration depth of the photon, λ is the average distance traveled by the photoexcited electron, and $d(E, k)$ represents the fraction of photoelectrons created within one mean free path from the surface. For the energy range of most PES experiments, $\alpha^{-1} \approx 100 - 1000 \text{ \AA}$ and $\lambda \approx 10 - 20 \text{ \AA}$, which implies that $\alpha\lambda \ll 1$ [1]. In this limit, in which the mean free path of the electron is smaller than the penetration depth of the incident photon, inspection of (27) shows that $d(E, k) \rightarrow \alpha\lambda$, which corresponds to a range of approximately $0.1 - 0.01$ for $d(E, k)$. Using a typical density of states ($\sim 10^{23} \text{ cm}^{-3}$) and the dimensions of sample surfaces in PES experiments, the range of $d(E, k)$ would not be expected to significantly inhibit electron transport to the surface. Therefore, it is likely that a sufficient quantity of electrons will escape from the surface to be captured by the analyzer.

2.1.3 Escape of the Electron into Vacuum.

In a free electron model, escaping photoelectrons must have sufficient kinetic energy, normal to the surface, to overcome the surface potential barrier

$$\frac{\hbar^2 \mathbf{K}_\perp^2}{2m} \geq E_{\text{vac}} - E_0, \quad (28)$$

where \mathbf{K}_\perp is the perpendicular component, in the direction of the surface normal, of the photoelectron wave vector \mathbf{K} inside the crystal, and E_{vac} and E_0 are the energy levels of the vacuum and at the bottom of the valence band, respectively. It follows

that the minimum value of \mathbf{K}_\perp required to escape an assumed perfect crystal surface is

$$\mathbf{K}_{\perp \min} = \frac{\sqrt{2m}}{\hbar} (E_{\text{vac}} - E_0)^{1/2}. \quad (29)$$

It is a key assumption of the three-step model that electron transmission through the surface-vacuum interface leaves the parallel component of the wave vector conserved such that

$$\mathbf{p}_\parallel / \hbar = \mathbf{K}_\parallel = \mathbf{k}_\parallel + \mathbf{G}_\parallel, \quad (30)$$

where \mathbf{p}_\parallel is the photoelectron momentum in vacuum, \mathbf{K}_\parallel is the parallel component of the wave vector \mathbf{K} of the photoexcited electron inside the crystal, \mathbf{k}_\parallel is the parallel wave vector component of the electron initial state, and \mathbf{G}_\parallel is the parallel component of the reciprocal lattice. Equation (30) for the free electron model represents Snell's law, such that

$$\mathbf{k}_{f\parallel} = \sin \vartheta \left(\frac{2m}{\hbar^2} E_{\text{kin}} \right)^{1/2} = \sin \vartheta' \left[\frac{2m}{\hbar^2} (E_f - E_0) \right]^{1/2}, \quad (31)$$

where ϑ and ϑ' are the angles, with respect to the surface normal, outside and inside the crystal, respectively.

The photoelectron kinetic energy outside the crystal could be determined via knowledge of the parallel and perpendicular photoelectron momentum components in vacuum, \mathbf{p}_\parallel and \mathbf{p}_\perp , respectively, by

$$E_{\text{kin}} = \frac{\hbar^2}{2m} [(\mathbf{p}_\parallel / \hbar)^2 + (\mathbf{p}_\perp / \hbar)^2] = E_f(\mathbf{k}) - E_{\text{vac}}, \quad (32)$$

but \mathbf{p}_\perp cannot be determined explicitly from the above equations. Alternatively, in a free electron solid, the crystal potential depth $E_{\text{vac}} - E_0$ could be determined, from which \mathbf{K}_\perp , the full wave vector of the crystal \mathbf{k} , and mapping of the band structure $E(\mathbf{k})$ are determined. However, the free electron model is not accurate enough to

permit full determination of \mathbf{K}_\perp . Specifically, the model fails owing to the fact that the wave function $\Psi_f(\mathbf{k})$ of a state at $E_f(\mathbf{k})$ in a real solid is not a single plane wave, but a Bloch wave containing plane wave contributions from various reciprocal lattice vectors. Furthermore, the individual components can be attributed to photoelectrons emerging from the crystal in many possible directions, dictated by (31) and (32).

Plane wave components of an individual Bloch wave of final energy state E with identical values of $\mathbf{k}_\parallel + \mathbf{G}_\parallel$ leave the crystal in the same direction and are added coherently. For such a $\mathbf{k}_\parallel + \mathbf{G}_\parallel$, the total transmission factor $|T(E_f, \mathbf{K}_\parallel)|^2$ of final energy state E_f is expressed as the sum of reduced transmission factors $|t(E_f, \mathbf{K}_\parallel)|$ for each plane wave $u_f(\mathbf{G}, \mathbf{k})$ as

$$|T(E_f, \mathbf{k}_\parallel)|^2 = |t(E_f, \mathbf{K}_\parallel)|^2 \left| \sum_{(k+G_\perp)>0} u_f(\mathbf{G}, \mathbf{k}) \right|^2, \quad (33)$$

where the summation includes only those components propagating toward the surface $(k + G_\perp) > 0$. An expression for \mathbf{p}_\perp/\hbar can be found from (32)

$$\frac{\mathbf{p}_\perp^2}{2m} = E_f(\mathbf{k}) - E_{\text{vac}} - \frac{\mathbf{p}_\parallel^2}{2m}, \quad (34)$$

and inserting $\mathbf{p}_\parallel = \mathbf{k}_\parallel + \mathbf{G}$ from (30) yields a “classical” estimate for the reduced transmission factor $t_f(E_f, \mathbf{K}_\parallel)$ as

$$|t(E_f, \mathbf{K}_\parallel)|^2 = \begin{cases} 1 & \text{if } E_f(\mathbf{k}) - E_{\text{vac}} > \hbar^2(\mathbf{k}_\parallel + \mathbf{G}_\parallel)^2/2m \\ 0 & \text{if } E_f(\mathbf{k}) - E_{\text{vac}} \leq \hbar^2(\mathbf{k}_\parallel + \mathbf{G}_\parallel)^2/2m \end{cases}. \quad (35)$$

Although this is an overestimate as electrons experience inelastic scattering processes due to surface plasmons, meaning $t_f(E_f, \mathbf{K}_\parallel) < 1$, analysis of experimental data has shown that the three-step model is a useful and accurate approximation. Assembling the pieces gives a final expression for the angle resolved energy spectrum of primary

photoelectrons

$$\begin{aligned}
N(E, \mathbf{K}_{\parallel}, h\nu)_{\text{pri}} &\propto \sum_{f,i} |M_{fi}(\mathbf{k}_i, \mathbf{k}_f)|^2 d(E_f, \mathbf{k}_f) |T(E_f, \mathbf{K}_{\parallel})|^2 \\
&\times \delta(E_f(\mathbf{k}_f) - E_i(\mathbf{k}_i) - h\nu) \delta(E - [E_f(\mathbf{k}_f) - \phi]) \\
&\times \delta(\mathbf{k}_i + \mathbf{G} - \mathbf{K}) \delta(\mathbf{K}_{\parallel} - \mathbf{p}_{\parallel}(\vartheta, \varphi)/\hbar). \tag{36}
\end{aligned}$$

The last δ function ensures that the component of momentum parallel to the crystal surface is conserved inside and outside the crystal.

2.2 Resonant Photoemission Spectroscopy

Resonant photoemission spectroscopy (RPES) is an interesting application of PES that provides information about occupied electronic states in a system. However, the key value of resonant photoemission to the study of rare earth doped GaN thin films is to probe which valence bands of the semiconductors have strong $4f$ and/or rare earth weight [7–9]. Resonance occurs when one stimulates photoemission using photons of energy $h\nu$ near an absorption threshold of a core level electronic state of binding energy $h\nu_j$. For the rare earth dopants studied in this research, resonance results from a signal overlap between direct emission of photoelectrons from the $4f$ state

$$4d^{10}4f^N + h\nu \longrightarrow 4d^{10}4f^{N-1} + e^-, \tag{37}$$

and Auger-like electrons emitted in a super Coster-Kronig process [10, 11]

$$4d^{10}4f^N + h\nu \longrightarrow [4d^94f^{N+1}]^* \longrightarrow 4d^{10}4f^{N-1} + e^-, \tag{38}$$

where $[]^*$ denotes an excited state. The final states for both the direct and recombination processes are identical.

Figure 8 depicts a general schematic of the process for a hypothetical solid, using a photon energy approaching the $4d$ core absorption threshold, and is explained as follows. Direct photoemission occurs from the $4f$ state, as shown in Figure 8(a)

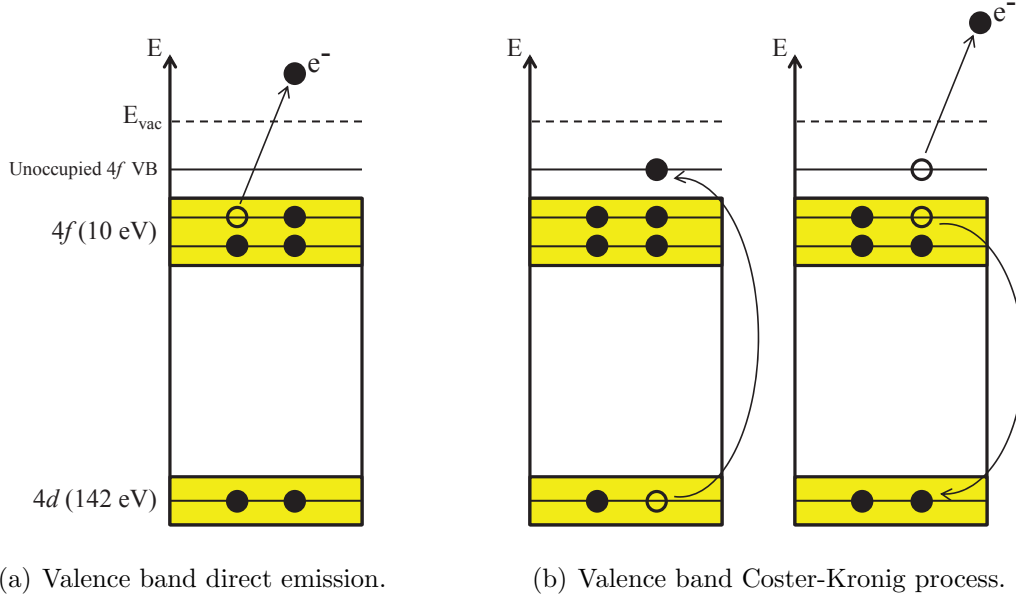


Figure 8. Schematic molecular-orbital diagram of the resonant photoemission process for a hypothetical solid.

and the emission process (37). Additionally, electrons from the $4d$ core state absorb photons and are excited to a bound, unoccupied $4f$ valence band state. The $4d$ hole is subsequently occupied by a $4f$ electron (de-excitation), and, if the energy difference between the $4f$ and $4d$ states is sufficient, $4f$ electron emission occurs as depicted in Figure 8(b) and process (38). The result is an enhanced photoemission signal due to the overlap between direct emission of the valence band electrons and the Auger-like electron emission following excitation and decay between the core electronic level and the bound valence band state; both processes result in an identical final state of the system.

The transitions of Figure 8(b) represent a special case of the Auger process, referred to as a Coster-Kronig transition [10, 11], in which the vacancy is filled by a higher electron subshell of the same electron shell. When the emitted electron also

belongs to the same shell, as shown in Figure 8(b), the process is called a super Coster-Kronig transition. Thus, the schematic shows both resonant photoemission and a super Coster-Kronig transition.

The intensity of the valence band features for which the direct and super Coster-Kronig processes overlap is described as a function of photon energy $h\nu$ by the Fano lineshape [11, 12] as

$$N(h\nu) \cong \frac{(\epsilon + q)^2}{\epsilon^2 + 1}, \quad \epsilon = \frac{h\nu - h\nu_j}{\Gamma}, \quad (39)$$

where $h\nu_j$ is the photon energy equal to the specified core level absorption threshold binding energy, q is the line profile index fitting parameter for the core level and is related to the Coulomb and dipole matrix elements [12], and $\Gamma = \Delta(h\nu_j)/2$ where $\Delta(h\nu_j)$ is the width (FWHM) of the core level. Thus, fitting (39) with experimental data is a common analytical technique.

Figure 9 displays the functional form of (39) and highlights the importance of the fitting parameter q . Inspection of (39) shows that as $h\nu \rightarrow h\nu_j$, $N(E, h\nu) \rightarrow q^2$. It follows in Figure 9 that the difference between $N(h\nu \approx 140)$ and $N(h\nu \ll 140)$ is approximately $q^2 = 4$, such that the fitting parameter q provides an estimate of the relative photoemission signal between values of $h\nu$ nearby and far from $h\nu_j$. Therefore, when analyzing the data, special attention should be given to the fitting parameter q , as an indicator of the resonant photoemission strength.

Resonant photoemission can be used to confirm or deny the presence of intended or unintended impurity ions in a solid. When coupled with other PES measurements, such as angle-resolved ultraviolet photoemission spectroscopy (ARUPS) or temperature-dependent X-ray photoemission spectroscopy, inferences can be made about the surface concentration of impurities, as well as the location of impurities in a crystal structure as either interstitial or substitutional ions, as will be discussed in the next section.

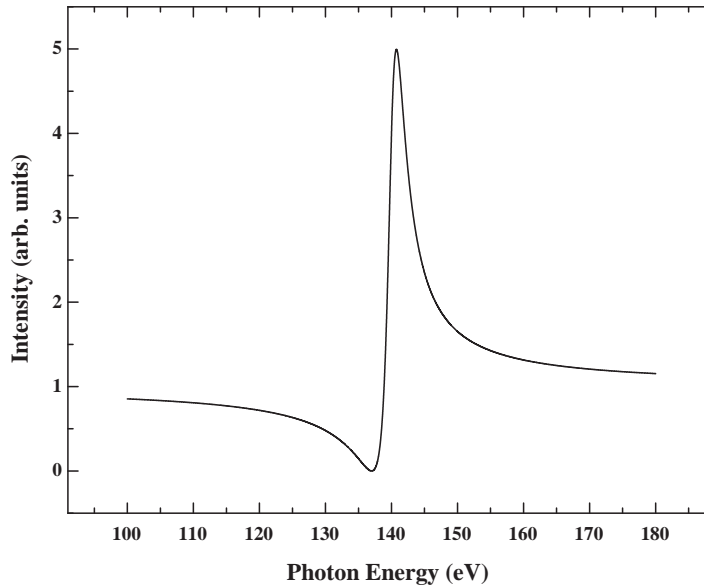


Figure 9. Plot of Fano function from (39) using $h\nu_j = 140$ eV, $\Delta h\nu_j = 3$ eV, and $q = 2$.

2.3 Temperature-Dependent X-ray Photoemission Spectroscopy

PES experiments are often performed at room temperature, which is sufficient to vibrationally excite atoms or molecules in a crystal structure. These vibrations can couple to atomic electrons via electron-phonon interactions and influence the PES data. Specifically, if PES is considered, phenomenologically, as an electron scattering process by the ions of a crystal, then detected electrons must reflect the effect of the lattice vibrations.

A free electron model treatment of valence electrons creates a minor pedagogical problem as free electrons, being only slightly perturbed by the crystal potential, are hardly influenced by lattice vibrations. However, if a tight-binding approach is considered, such that the electrons are rigidly attached to the vibrating ion cores, the effect of lattice vibrations is introduced and the pedagogical problem becomes somewhat transparent. Under this approximation, the transition matrix element of

the perturbing Hamiltonian from the Golden Rule (18) is calculated [1] as

$$\langle f | \mathbf{H}' | i \rangle \propto \sigma_{pe} S, \quad (40)$$

where σ_{pe} is the photoabsorption cross section and S is the scattering factor

$$S = \sum_{\mu, \nu} \exp[i\Delta \mathbf{k} \cdot (\mathbf{R}_\mu - \mathbf{R}_\nu)]; \quad \Delta \mathbf{k} = \mathbf{k}_f - \mathbf{k}_i. \quad (41)$$

Indices μ and ν span the atomic sites, not the electron initial and final states, and $\mathbf{R}_{\mu, \nu}$ represents the coordinate of the atom. Thus, lattice vibrations are accounted for as

$$\mathbf{R}_{\mu, \nu}(T) = \mathbf{R}_{\mu, \nu} + \mathbf{u}_{\mu, \nu}(T), \quad (42)$$

where $\mathbf{u}_{\mu, \nu}$ is the displacement of the respective ion. The temperature-dependent photocurrent is then determined as

$$N(E, h\nu, T) \propto |\sigma_{pe}|^2 \left\{ \underbrace{\exp[-\Delta k^2 u_0^2(T)] \sum_{\mathbf{G}} \delta(\Delta \mathbf{k} - \mathbf{G})}_{\text{direct PE current}} + \underbrace{N(1 - \exp[-\Delta k^2 u_0^2(T)])}_{\text{indirect PE current}} \right\}. \quad (43)$$

The direct current term represents the temperature-dependent attenuated photoemission signal, N is the number of atoms that contribute to the signal, and the indirect current results from phonon assisted momentum transitions that occur at a finite temperature.

Qualitatively, as the temperature of a solid is increased, lattice vibrations increase, which reduce an electron's ability to traverse through the material, escape, and get detected. Quantitatively, the intensity of an emitted or scattered electron beam decays exponentially, due to increased thermal vibrations from increased tem-

perature as [1, 13]

$$I = I_0 e^{-2W}, \quad (44)$$

where I_0 is the reference intensity, which is typically the lowest temperature spectrum. The Debye-Waller factor W is expressed as

$$2W = \Delta k^2 \langle u_0 \rangle^2, \quad (45)$$

where Δk is the wave vector transfer and $\langle u_0 \rangle^2$ is the mean square displacement of the atoms. Within the Debye model of thermal vibrations, in the case of isotropic vibrations, W is described as

$$2W = \frac{3\hbar^2 (\Delta k)^2 T}{m k_B \Theta_D^2}. \quad (46)$$

In (46), $\hbar(\Delta k)$ is the electron momentum transfer due to phonon coupling, m is the mass of the scattering ion, k_B is the Boltzmann constant, and Θ_D is the Debye temperature. Δk is calculated from the experimentally measured electron kinetic energy E_{kin} as

$$(\Delta k)^2 = \frac{2 m_e E_{\text{kin}}}{\hbar^2}, \quad (47)$$

where m_e is the electron mass. From equations (44) and (46),

$$\begin{aligned} \ln \left[\frac{I}{I_0} \right] &= -2W \\ &= -\frac{3\hbar^2 (\Delta k)^2 T}{m k_B \Theta_D^2} \propto -\frac{T}{\Theta_D^2}. \end{aligned} \quad (48)$$

Therefore, when plotted, the slope $|S|$ of the logarithm of relative intensity I/I_0 as a function of temperature is inversely proportional to the square of the Debye

temperature, as

$$|S| = \frac{3\hbar^2(\Delta k)^2}{m k_B \Theta_D^2}. \quad (49)$$

As mentioned, resonant photoemission can be combined with temperature-dependent XPS to draw conclusions about the presence and location of impurity ions in a crystal structure. As an example, consider a ternary compound semiconductor $A_xB_{1-x}C$ where ion A is intended to be substitutional for ion B in $x\%$ of B sites within the lattice structure BC. Resonant photoemission can effectively confirm the presence of ion A by scanning through photon energies near an absorption threshold of a core level electronic state of A. By graphing the intensities of the resulting spectral features and analyzing the energetically allowed electronic transitions, one can make inferences about the occupied states of the ternary compound. If this analysis shows an enhancement of spectral features located at electron binding energies that are consistent with ion A, then one may conclude that the ion was successfully incorporated into the compound, and inferences about band hybridization can be made. However, the precise location of ion A within the crystal structure would be undetermined. Temperature-dependent XPS analysis and calculation of the Debye temperatures for ions A and B permits inferences about the location of ion A. Specifically, if Θ_D for A and B are equal, within experimental uncertainty, then one may conclude that the electron-phonon interactions for both ions are identical, and one may classify ion A as substitutional for ion B in the structure. On the other hand, if the ions' Debye temperatures are not equal, then one may conclude that ion A is vibrating from an interstitial location within the crystal structure.

2.4 The Schottky Barrier

The metal-semiconductor interface spans the subject of surface science and semiconductor theory, as techniques from both fields can effectively measure interface

properties. One such property, the Schottky barrier, is a potential barrier that exists at the interface between a metal and semiconductor and is related, roughly, to the difference in work functions between materials. This barrier is responsible for controlling current conduction and capacitance behavior and therefore warrants careful consideration.

As an example, the interface electronic properties of many metal/GaN systems have been directly measured and studied using photoemission spectroscopy and other techniques. Specifically, Cs, Mg, Al, Ti, Ni, Au, Pd, and Pt on GaN surfaces have been reported [14–26] and, more recently, Xiao *et al.* presented an original study of rare-earth metals (Gd) on GaN [27].

Alternatively, electronic measurement of interface properties via current-voltage (I-V) and capacitance-voltage (C-V) characteristics also facilitate Schottky barrier height calculation. However, the benefit of direct surface barrier height measurement is avoidance of complications associated with other experimental techniques. For example, defects at the metal-semiconductor interface can lead to complications in I-V measurements of the surface barrier height [28,29]. Similarly, C-V determination of the barrier height can be complicated by these defects, which alter the space charge region and affect the measured flat band voltage [28,29]. Accordingly, the sections that follow will discuss the theoretical models, underlying assumptions, and experimental techniques associated with direct spectroscopic measurement and indirect electronic measurement of the Schottky barrier height of a metal-semiconductor interface. The final section will discuss the Schottky barrier relevance for radiation detector designers.

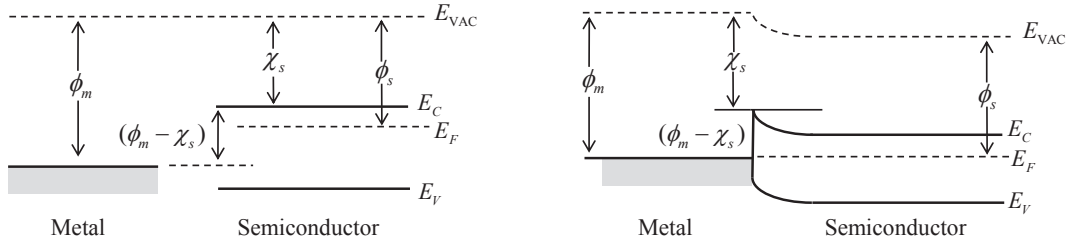
2.4.1 Schottky-Mott Model.

The Schottky-Mott model, which is the most simplistic physical model and assumes intimate and abrupt contact as shown in Figure 10, predicts a barrier height

at the metal to n -type semiconductor interface $\Phi_{B,n}$ of

$$\Phi_{B,n} = \phi_m - \chi_s, \quad (50)$$

where ϕ_m and χ_s are the metal work function and semiconductor electron affinity, respectively. Closer inspection of Figure 10(b) shows that an alternate expression



(a) Energy band diagram of an isolated metal adjacent to an n -type semiconductor under thermal non-equilibrium condition.

(b) Energy band diagram of a metal-semiconductor contact in thermal equilibrium.

Figure 10. Ideal Schottky barrier formation.

for $\Phi_{B,n}$ is

$$\Phi_{B,n} = E_g - (E_F - E_V), \quad (51)$$

where E_g , E_F , and E_V are the band gap, surface Fermi, and surface valence band maximum energies, respectively, of the semiconductor. Photoemission spectroscopy permits direct measurement of these energy levels, the surface valence band bending, and, therefore, the Schottky barrier height as metal overlayers are deposited on a semiconductor surface.

In practice, the simple theoretical expression for barrier height as given by equation (50) is never realized experimentally. Specifically, an unavoidable interface layer between the metal and semiconductor surfaces as well as the presence of semiconductor surface states alter the measured Schottky barrier from the ideal value calculated by the Schottky-Mott model. Furthermore, on an atomic scale, the transition is

not abrupt but gradual, with local fields varying from atom to atom. One model used to explain practical interfaces is the metal induced gap states (MIGS) model which claims that defects due to metal deposition and the presence of semiconductor surface states result in interface traps that trap charge and change the ideal barrier height.

2.4.2 Metal Induced Gap States Model.

When seeking a more complete theoretical model to compare with the measured results, both chemical bonding and physical concepts must be considered. Extensive measurements using photoemission spectroscopy indicate that for most covalent semiconductors, and specifically III-V compounds, the Schottky barrier formation is due mainly to defects generated near the metal-semiconductor interface by deposition of the metal [30]. On several compound semiconductors such as GaAs, GaSb, and InP, the surface Fermi-level positions obtained from various metals are pinned at an energy level quite independent of the metal [31]. Thus, the Fermi level pinning explains the fact that the barrier height in covalent semiconductors is essentially independent of the metal work function.

For ionic semiconductors, the barrier height generally depends strongly on the metal and a correlation has been found between interface behavior and the electronegativity difference between the metal and semiconductor materials [32, 33]. Specifically, the interface bonds at metal-semiconductor contacts are partly ionic, as are all heteropolar bonds [33]. Generalizing Pauling's concept [34] that the ionicity of covalent single bonds is described by the electronegativity difference between the atoms, the charge transfer at a metal-semiconductor interface is characterized by the electronegativity difference between the materials.

Using simple physical arguments as a basis, Heine [35] pointed out that wave functions of the metal electrons tail into the semiconductor in the energy range where

the metal conduction band overlaps the semiconductor band gap. He concluded that this continuum of metal induced gap states represents the fundamental mechanism that determines Schottky barrier height. The schematic energy diagram in Figure 11 shows a practical metal-semiconductor interface with an interface layer of width δ between the surfaces.

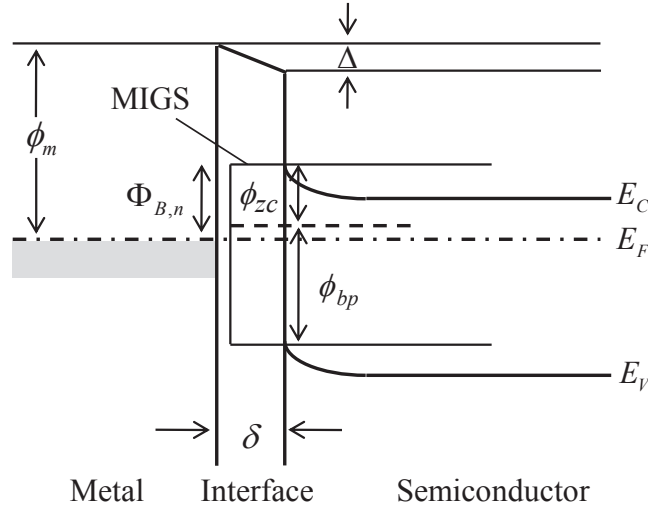


Figure 11. Schematic energy diagram of a practical metal-semiconductor interface with a continuum of interface states.

The MIGS arise from nearby bands and are predominantly donor-like (charge neutral when occupied, positively charged when unoccupied), closer to the valence band maximum and mostly acceptor-like (charge neutral when unoccupied, negatively charged when occupied), nearer to the conduction band minimum. The energy level ϕ_{bp} above the valence band maximum at which the dominant behavior changes is called the branch point. Consequently, when ϕ_{bp} is above, coincides with, or is below the Fermi level, the net charge in these interface states is positive, vanishes, or negative, respectively. Lastly, from the schematic diagram, the zero-charge transfer

barrier height ϕ_{zc} is calculated as

$$\phi_{zc} = E_g - (\phi_{bp} - E_V). \quad (52)$$

When the density of interface traps D_{it} in the region δ is large ($D_{it} \rightarrow \infty$), the Schottky barrier height approaches the value given by equation (52). Inspection of the equation indicates that barrier height is independent of the metal work function and is determined entirely by the interface properties of the semiconductor. In this case, the Fermi level at the interface is said to be *pinned* by the surface states at a value ϕ_{bp} above the valence band maximum [36]. In the other limiting case ($D_{it} \rightarrow 0$), the Schottky barrier height approaches the value given by the Schottky-Mott model in equation (50).

For the case $0 < D_{it} < \infty$, the Schottky barrier height is linearly corrected from (52) by factors that are dependent upon material properties of both the metal and the semiconductor. Specifically, in combining the physical argument of MIGS and the chemical concept of partly ionic interface bonds, Mönch [33] predicted Schottky barrier heights $\Phi_{B,n}$ to be larger or smaller than the zero-charge transfer barrier height ϕ_{zc} if the electronegativity difference between the metal and semiconductor ($X_m - X_s$) was positive or negative, respectively, as given by

$$\Phi_{B,n} = \phi_{zc} + S_X(X_m - X_s). \quad (53)$$

The relationship in (53) simply states that the Schottky barrier varies linearly as a function of the electronegativity difference where S_X is the slope parameter as determined by

$$\frac{A_X}{S_X} - 1 \approx 0.1(\epsilon_\infty - 1)^2. \quad (54)$$

Here A_X is calculated from the MIGS model as either 0.86 eV/Miedema-unit or

1.79 eV/Pauling-unit when using the Miedema or Pauling values for electronegativity, and ϵ_∞ is the optical dielectric constant of the bulk valence electrons of the semiconductor [33]. Thus, a theoretical value for $\Phi_{B,n}$ can be determined from equation (53) using material properties and by calculating the branch point energy above the valence band maximum in order to solve (52).

At first glance, the relationship between barrier height, the slope parameter S_X , and the semiconductor ϵ_∞ might appear unconvincing. Full theoretical development of (54) requires a rather rigorous analysis of the charge transfer dynamics at the metal-semiconductor interface, which can be found elsewhere [36, 37]. While this analysis elucidates the connection between the physical relationship and the governing parameters, the association between them may be better understood graphically, as is done within the reported literature. As an example, Figure 12 displays the relationship between the electronegativity difference $X_m - X_s$ at the hypothetical metal to semiconductor interface between various low and high work function metals and n -type silicon. Just as with silicon in the example, these figures and theoretical relationships are determined by experimentally measuring barrier heights between various metals for a given semiconductor surface. Careful attention must be given to semiconductor growth, sample and surface preparation, metal deposition method, and barrier height measurement, in order to ensure consistent experimental conditions; thus, generating a theoretical MIGS relationship via data extrapolation is a significant undertaking. However, these theoretical relationships are valuable in determining whether or not MIGS play a role at a particular metal-semiconductor interface.

Whether or not metal induced gap states play a role at the metal to GaN thin film interface is a subject of debate. Kurtin, McGill, and Mead [38] suggested that the Schottky barrier height on GaN should depend directly on the work function or electronegativity difference between the metal electrode and GaN. Foresi and Mous-

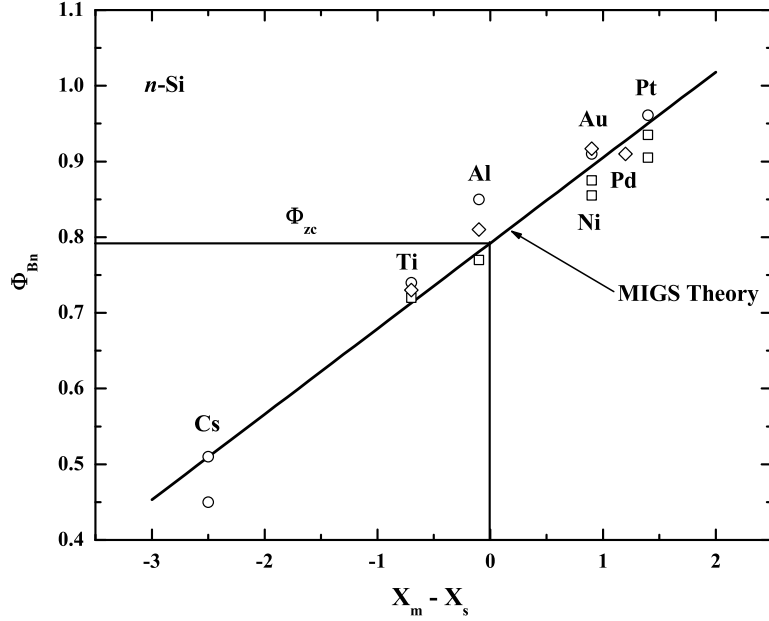


Figure 12. Barrier heights of various metal to n -Si contacts as a function of electronegativity difference. The theoretical MIGS line (solid) is drawn using a least squares fit of the data with $\Phi_{zc} = 0.792$ and $S_X = 0.113$. Adapted from [1].

takas [39] observed this direct correlation experimentally, while Guo *et al.* [40] and Mori *et al.* [41] observed only a weak dependence of the Schottky barrier height on the metal work function for n -type GaN and p -type GaN, respectively. The 1998 review of metal-GaN contact technology by Liu and Lau [42] reported that, for a variety of contact metals with both low and high work functions, Schottky barrier heights at the metal-GaN interface varied with metal work function, within the experimental scatter. Subsequent work by Rickert *et al.* [28] supported a modified Schottky-Mott model at the metal-GaN interface for Ni, Pd, and Al, yet more “complex” behavior when Au, Ti, and Pt were used as the contact metals. Additional experiments by Barinov *et al.* [22,23] reported Schottky barrier heights at the Au-GaN interface that exceeded both work function difference (Schottky-Mott) and electronegativity difference (metal induced gap states) models. Thus, a point worth emphasizing is that regardless of the particular metal-GaN interface studied, experimentally measured barrier heights vary considerably.

The final section of this chapter discusses a method of Schottky barrier height calculation, which was not conducted in this research, but is common in the literature. This section is presented for several reasons. First, the Schottky barrier heights at the metal to rare earth doped GaN interfaces, determined using photoemission spectroscopy, will be compared with previously reported results that were derived from both spectroscopic data and device I-V and C-V characteristics. For this reason, a cursory understanding of current transport in Schottky barrier devices is necessary. Additionally, the application of the results to devices, and particularly to radiation detectors, requires at least a brief discussion. Lastly, the topic and its application represent areas for potential future research in the field of rare earth doped GaN thin films.

2.4.3 Current Transport in Schottky Barrier Devices.

Current transport across a Schottky barrier results from thermionic emission of majority carriers from the semiconductor over the electrostatic potential barrier into the metal, or from carrier tunneling through the barrier, and measurement of device I-V properties allows calculation of this barrier.

In thermal equilibrium, and considering an n -type semiconductor, the emission of electrons from the semiconductor into the metal is balanced by the flow of electrons from the metal into the semiconductor. The concentration of electrons n_{th} that possess sufficient energy to traverse the barrier $\Phi_{B,n}$ is [43]

$$n_{th} = N_C \exp \left[-\frac{\Phi_{B,n}}{k_B T} \right], \quad (55)$$

where N_C is the effective density of states in the conduction band, k_B is Boltzmann's constant, and T is the temperature.

At thermal equilibrium, the current density conditions described above are ex-

pressed as

$$\begin{aligned}
|J_{m \rightarrow s}| &= |J_{s \rightarrow m}| \propto n_{th} \\
|J_{m \rightarrow s}| &= |J_{s \rightarrow m}| = C_1 N_C \exp \left[-\frac{\Phi_{B,n}}{k_B T} \right], \tag{56}
\end{aligned}$$

where C_1 is a proportionality constant, and $J_{m \rightarrow s}$ and $J_{s \rightarrow m}$ are the current densities from the metal to the semiconductor and from the semiconductor to the metal, respectively.

An applied forward bias V_F at the contact reduces the electrostatic potential difference across the barrier and increases the electron density across the interface to

$$n_{th} = N_C \exp \left[-\frac{(\Phi_{B,n} - qV_F)}{k_B T} \right]. \tag{57}$$

The current density on the semiconductor side of the interface $J_{s \rightarrow m}$ is altered by the same amount, but the electron current density remains unchanged from the metal to the semiconductor because the barrier remains at its equilibrium value from the viewpoint of electrons on the metal side of the interface. Therefore, under forward bias, the net current density is

$$\begin{aligned}
J &= J_{s \rightarrow m} - J_{m \rightarrow s} \\
&= C_1 N_C \exp \left[-\frac{(\Phi_{B,n} - qV_F)}{k_B T} \right] - C_1 N_C \exp \left[-\frac{\Phi_{B,n}}{k_B T} \right] \\
&= C_1 N_C \exp \left[-\frac{\Phi_{B,n}}{k_B T} \right] \left(\exp \left[\frac{qV_F}{k_B T} \right] - 1 \right). \tag{58}
\end{aligned}$$

The same argument for the reverse bias condition produces an identical expression to (58), except that V_F is replaced by $-V_R$. It should be noted that, in addition to the electron (majority carrier) current, a hole (minority carrier) current exists from the metal to the semiconductor due to the minority carrier injection. However, typical

minority carrier currents are orders of magnitude smaller than those of minority carriers, which characterizes Schottky diodes as single carrier conduction, or unipolar, devices [43].

The coefficient $C_1 N_C$ in equation (58) can be shown to be equal to $A^* T^2$ where A^* is the effective Richardson constant, in units of $\text{A/K}^2\text{-cm}^2$, and depends directly on the electron effective mass in the semiconductor material. Therefore, the current-voltage characteristic of a metal-semiconductor contact is

$$J = J_s \left(e^{qV/k_B T} - 1 \right) , \quad (59)$$

$$J_s = A^* T^2 e^{-\Phi_{B,n}/k_B T} , \quad (60)$$

where J_s is the saturation current. In (59) V can be either V_F or $-V_R$, depending on bias conditions.

Experimental calculation of Schottky barrier heights via equations (59) and (60) is done as follows. Current density versus applied forward voltage is plotted and extrapolated to $V = 0$, yielding a value for J_s , from which the barrier height is obtained via (60) and knowledge of the effective Richardson constant. This device parameter has critical implications with regard to radiation detector devices.

Schottky contacts serve an important function as rectifying contacts in general semiconductor device design, but an often critical function for semiconductor-based radiation detectors. Despite efforts to limit current flow due to leakage, and maximize the charge collection volume, the generated signal due to radiation-induced currents can prove difficult to detect above noise due to leakage currents. In such situations, Schottky contacts are desirable to reduce the noise associated with leakage currents and maximize the signal of the radiation-induced currents. Quantitatively,

the contact resistance ρ_c is determined by the surface barrier height [28] as

$$\rho_c = \frac{k_B}{qA^*T} \exp \left[\frac{\Phi_{B,n}}{k_B T} \right]. \quad (61)$$

It is evident from (61) that small reductions in the surface barrier height will have a large effect in reducing the contact resistance at the Schottky contact, which adversely affects the signal-to-noise ratio and performance of a diode radiation detector.

References

- [1] S. Hüfner, *Photoelectron Spectroscopy: Principles and Applications*. Springer-Verlag, 2003.
- [2] H. Hertz, “On the influence of ultraviolet light on the electric discharge,” *Ann Physik*, vol. 31, pp. 983–1000, 1887.
- [3] A. B. Arons and M. B. Peppard, “Einstein’s proposal of the photon concept - a translation of the Annalen der Physik paper of 1905,” *Annalen der Physik*, pp. 367–374, 1965.
- [4] C. N. Berglund and W. E. Spicer, “Photoemission studies of copper and silver: Theory,” *Physical Review*, vol. 136, no. 4A, pp. 1030–1044, 1964.
- [5] M. Cardona and L. Ley, *Photoemission in Solids: General Principles*. Springer-Verlag New York, 1978.
- [6] C. Cohen-Tannoudji, B. Diu, and F. Laloe, *Quantum Mechanics. vol. 1-2*. New York: John Wiley and Sons, 1977.
- [7] I. Ketsman, Y. B. Losovyj, A. Sokolov, J. Tang, Z. Wang, K. D. Belashchenko, and P. A. Dowben, “The n -type Gd-doped HfO_2 to silicon heterojunction diode,” *Applied Physics A: Materials Science & Processing*, vol. 89, no. 2, pp. 489–492, 2007.
- [8] R. F. Sabirianov, W. N. Mei, J. Lu, Y. Gao, X. C. Zeng, R. D. Bolskar, P. Jeppson, N. Wu, A. N. Caruso, and P. A. Dowben, “Correlation effects and electronic structure of Gd @ C60,” *Journal of Physics: Condensed Matter*, vol. 19, p. 082201, 2007.

- [9] I. Ketsman, Y. B. Losovyj, A. Sokolov, J. Tang, Z. Wang, M. L. Natta, J. I. Brand, and P. A. Dowben, “Gd-doping of HfO₂,” *Applied Surface Science*, vol. 254, no. 14, pp. 4308–4312, 2008.
- [10] D. Coster, L. Kronig, and R. De, “New type of Auger effect and its influence on the X-ray spectrum,” *Physica*, vol. 2, no. 1-12, pp. 13–24, 1935.
- [11] G. Wendin, *Breakdown of the One-Electron Pictures in Photoelectron Spectra, Structure and Bonding Vol. 45*. Springer-Verlag, Berlin, 1981.
- [12] U. Fano, “Effects of configuration interaction on intensities and phase shifts,” *Physical Review*, vol. 124, no. 6, pp. 1866–1878, 1961.
- [13] L. J. Clarke, *Surface Crystallography*. New York: John Wiley and Sons, 1985.
- [14] T. U. Kampen, M. Eyckeler, and W. Mönch, “Electronic properties of cesium-covered GaN (0001) surfaces,” *Applied Surface Science*, vol. 123, pp. 28–32, 1998.
- [15] M. Eyckeler, W. Mönch, T. U. Kampen, R. Dimitrov, O. Ambacher, and M. Stutzmann, “Negative electron affinity of cesiated *p*-GaN (0001) surfaces,” *Journal of Vacuum Science & Technology B: Microelectronics and Nanometer Structures*, vol. 16, p. 2224, 1998.
- [16] V. M. Bermudez, “Study of the growth of thin Mg films on wurtzite GaN surfaces,” *Surface Science*, vol. 417, no. 1, pp. 30–40, 1998.
- [17] C. I. Wu and A. Kahn, “Investigation of the chemistry and electronic properties of metal/gallium nitride interfaces,” *Journal of Vacuum Science & Technology B: Microelectronics and Nanometer Structures*, vol. 16, p. 2218, 1998.
- [18] V. M. Bermudez, T. M. Jung, K. Doverspike, and A. E. Wickenden, “The growth and properties of Al and AlN films on GaN(0001) – (1 × 1),” *Journal of Applied Physics*, vol. 79, no. 1, p. 110, 1996.
- [19] V. M. Bermudez, R. Kaplan, M. A. Khan, and J. N. Kuznia, “Growth of thin Ni films on GaN(0001) – (1 × 1),” *Physical Review B*, vol. 48, no. 4, pp. 2436–2444, 1993.
- [20] A. Barinov, L. Gregoratti, B. Kaulich, M. Kiskinova, and A. Rizzi, “Defect-induced lateral chemical heterogeneity at Ni/GaN interfaces and its effect on the electronic properties of the interface,” *Applied Physics Letters*, vol. 79, p. 2752, 2001.
- [21] A. Barinov, L. Gregoratti, and M. Kiskinova, “Direct experimental evidence of insensitivity of local Schottky barriers to lateral chemical inhomogeneity in case studies of metal/GaN (0001) interfaces,” *Physical Review B*, vol. 64, no. 20, p. 201312, 2001.

- [22] A. Barinov, L. Casalis, L. Gregoratti, and M. Kiskinova, “Stages of formation and thermal stability of a gold- n -GaN interface,” *Journal of Physics D: Applied Physics*, vol. 34, pp. 279–284, 2001.
- [23] L. Casalis, A. Barinov, L. Gregoratti, and M. Kiskinova, “Au/GaN interface: initial stages of formation and temperature-induced effects,” *Physical Review B*, vol. 63, no. 8, p. 85308, 2001.
- [24] T. G. G. Maffei, M. C. Simmonds, S. A. Clark, F. Peiro, P. Haines, and P. J. Parbrook, “Near ideal, high barrier, Au- n -GaN Schottky contacts,” *Journal of Physics D: Applied Physics*, vol. 33, no. 20, pp. L115–L118, 2000.
- [25] P. J. Hartlieb, A. Roskowski, R. F. Davis, W. Platow, and R. J. Nemanich, “Pd growth and subsequent Schottky barrier formation on chemical vapor cleaned p -type GaN surfaces,” *Journal of Applied Physics*, vol. 91, p. 732, 2002.
- [26] S. M. Gasser, E. Kolawa, and M. A. Nicolet, “Thermal reaction of Pt film with $\langle 110 \rangle$ GaN epilayer,” *Journal of Vacuum Science & Technology A: Vacuum, Surfaces, and Films*, vol. 17, p. 2642, 1999.
- [27] W. Xiao, Q. Guo, Q. Xue, and E. G. Wang, “Gd on GaN(0001) surface - Growth, interaction, and Fermi level movement,” *Journal of Applied Physics*, vol. 94, p. 4847, 2003.
- [28] K. A. Rickert, A. B. Ellis, J. K. Kim, J. L. Lee, F. J. Himpsel, F. Dzikusuma, and T. F. Kuech, “X-ray photoemission determination of the Schottky barrier height of metal contacts to n -GaN and p -GaN,” *Journal of Applied Physics*, vol. 92, p. 6671, 2002.
- [29] D. K. Schroder, *Semiconductor Material and Device Characterization*. New York: John Wiley and Sons, 1990.
- [30] W. E. Spicer, P. W. Chye, C. M. Garner, I. Lindau, and P. Pianetta, “The surface electronic structure of III-V compounds and the mechanism of Fermi level pinning by oxygen (passivation) and metals (Schottky barriers),” *Surface Science*, vol. 86, pp. 763–788, 1979.
- [31] W. E. Spicer, I. Lindau, P. Skeath, C. Y. Su, and P. Chye, “Unified mechanism for Schottky-barrier formation and III-V oxide interface states,” *Physical Review Letters*, vol. 44, no. 6, pp. 420–423, 1980.
- [32] W. Mönch, *Electronic Properties of Semiconductor Interfaces*. Springer-Verlag, 2004.
- [33] —, “Barrier heights of real Schottky contacts explained by metal-induced gap states and lateral inhomogeneities,” *Journal of Vacuum Science & Technology B: Microelectronics and Nanometer Structures*, vol. 17, p. 1867, 1999.

- [34] L. Pauling, *The Nature of the Chemical Bond*. Ithica, NY: Cornell University Press, 1960, no. 3.
- [35] V. Heine, “Theory of surface states,” *Physical Review*, vol. 138, no. 6A, pp. 1689–1696, 1965.
- [36] S. M. Sze and K. N. Kwok, *Physics of Semiconductor Devices*. Hoboken, NJ: John Wiley and Sons, 2007.
- [37] W. Mönch, *Semiconductor surfaces and interfaces*. Springer Verlag, 2001.
- [38] S. Kurtin, T. C. McGill, and C. A. Mead, “Fundamental transition in the electronic nature of solids,” *Physical Review Letters*, vol. 22, no. 26, pp. 1433–1436, 1969.
- [39] J. S. Foresi and T. D. Moustakas, “Metal contacts to gallium nitride,” *Applied Physics Letters*, vol. 62, no. 22, p. 2859, 1993.
- [40] J. D. Guo, M. S. Feng, R. J. Guo, F. M. Pan, and C. Y. Chang, “Study of Schottky barriers on *n*-type GaN grown by low-pressure metalorganic chemical vapor deposition,” *Applied Physics Letters*, vol. 67, p. 2657, 1995.
- [41] T. Mori, T. Kozawa, T. Ohwaki, Y. Taga, S. Nagai, S. Yamasaki, S. Asami, N. Shibata, and M. Koike, “Schottky barriers and contact resistances on *p*-type GaN,” *Applied Physics Letters*, vol. 69, no. 23, pp. 3537–3539, 1996.
- [42] Q. Z. Liu and S. S. Lau, “A review of the metal-GaN contact technology,” *Solid-State Electronics*, vol. 42, no. 5, pp. 677–691, 1998.
- [43] S. M. Sze, *Semiconductor Devices: Physics and Technology*. Hoboken, NJ: John Wiley and Sons, 2002.

III. Experimental Procedures

This chapter discusses general experimental procedures used during research. Additional details pertaining to the individual experiments can be found in Chapters IV, V, and VI. The ultrahigh vacuum conditions needed for photoemission experiments required that all experiments occur at either the Center for Advanced Microstructures and Devices (CAMD) at Louisiana State University in Baton Rouge, LA or at the Nebraska Center for Materials and Nanoscience at the University of Nebraska (Lincoln) campus. Altogether, 13 experiments (8 resonant photoemission, 4 Schottky barrier measurement, 1 surface Debye temperature) were conducted during 14 total weeks spanning November 2009–December 2010.

3.1 Sample Growth and Characterization

The rare earth doped gallium nitride thin films were prepared at the University of Puerto Rico and the University of Nebraska (Lincoln) using plasma assisted molecular beam epitaxy [1]. Molecular beam epitaxy is a relatively slow deposition rate process (< 1000 nm/hour), shown schematically in Figure 13, and takes place in high or ultra high vacuum. Vacuum conditions limit the introduction of unwanted impurities during the growth process and maximize the mean free paths of the individual atoms in order to minimize their interactions between the respective effusion cells and the substrate wafer. During film growth, ultra-pure solid-form elements are heated in separate effusion cells to their appropriate sublimation temperatures. In their gaseous forms and within the nitrogen-rich environment indicated by the figure, the gaseous elements condense epitaxially on the substrate wafer. During operation, reflection high energy electron diffraction (RHEED) monitors crystal layer growth, and computer-controlled shutters in front of each effusion cell allow precise control of layer thickness. Details pertaining to the specific growth parameters for GaN:RE

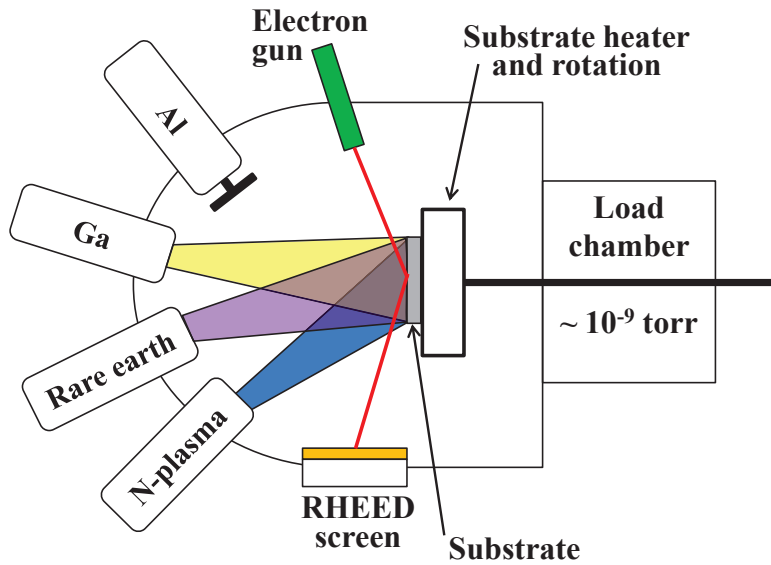


Figure 13. Typical molecular beam epitaxy schematic.

thin film deposition will be discussed in Chapters IV, V, and VI.

Another technique which was used to prepare samples is pulsed laser deposition [2], depicted in Figure 14. During the growth process, a laser beam strikes the surface of the source (target) material, and the deposited energy from the laser evaporates the target's surface. The short laser pulses, typically less than 50 ns in duration, cause the surface temperature of the target to rise rapidly, while the bottom of the target remains cooler. The nonequilibrium heating produces a flash of evaporants that deposit on the substrate, producing a film with composition identical to that of the target surface. This ability to replicate the composition of the source in the film is perhaps the greatest benefit of PLD. Whereas thermal evaporation techniques, such as molecular beam epitaxy, produce vapor compositions dependent upon the vapor pressures of the elements in the target material, the laser-induced expulsion of material from pulsed laser deposition yields a plume of material with stoichiometry identical to the target. Lastly, although the schematic in Figure 14 shows only a single target material, experimental configurations capable of positioning multiple

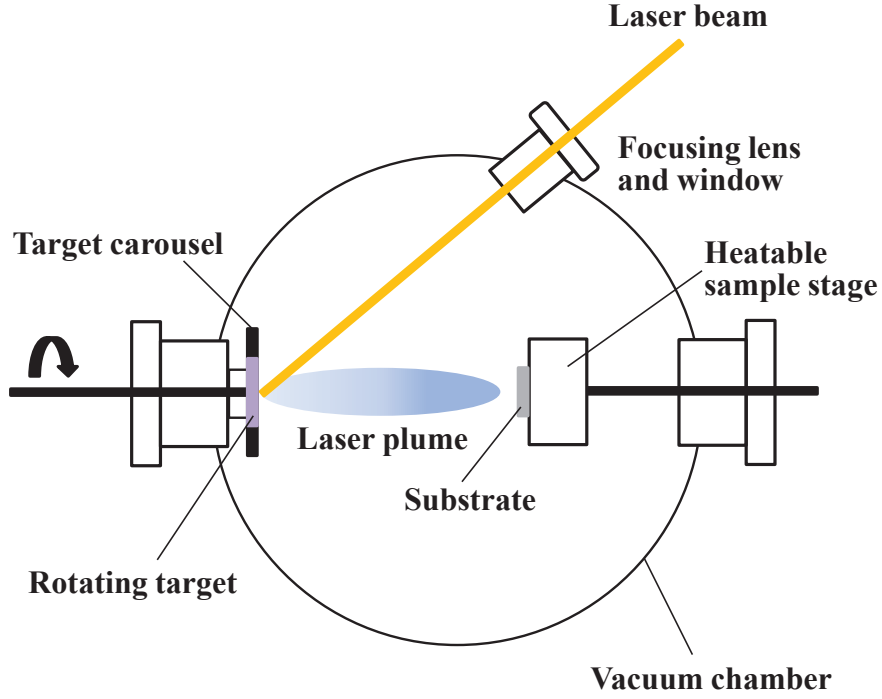


Figure 14. Typical pulsed laser deposition schematic.

targets within the laser beam exist.

Following growth, film thickness was measured with a surface profilometer, and X-ray diffraction (XRD) analysis verified orientation, crystal structure, and film purity. XRD was conducted either using a Siemens D5000 or Rigaku θ -2D X-ray diffractometer, using a copper target X-ray tube that produced radiation at the Cu K_α wavelength ($\lambda = 1.5406 \text{ \AA}$). The sample and detector were rotated with respect to the incident beam angle θ and spectra were collected.

Figure 15 shows the X-ray diffraction pattern of a GaN:Yb film grown on Si(111) substrates. The Bragg formalism predicts that diffraction maxima between parallel planes of ions spaced a distance d apart occur when incident light of wavelength λ :

- (1) reflects from a crystal plane where the angle of incidence θ equals the angle of reflection;
- (2) results in constructive interference of reflected rays from successive planes.

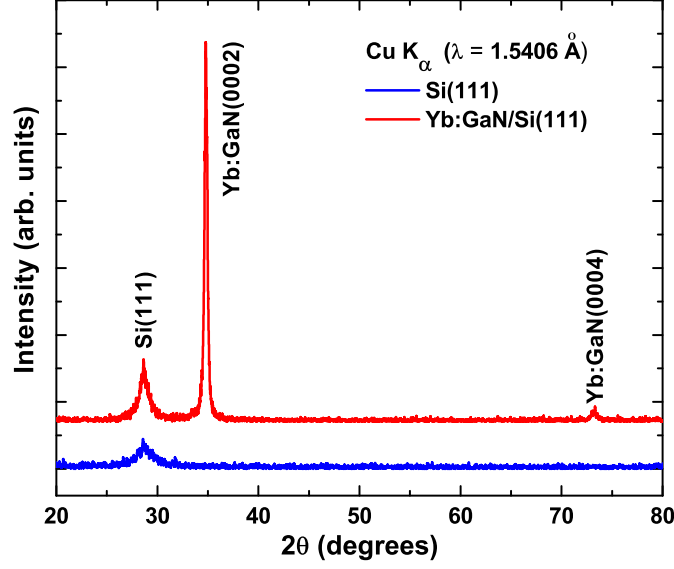


Figure 15. The X-ray diffraction (XRD) pattern of a GaN:Yb film grown on Si(111) substrates. The films show c -axis orientation of the texture growth and a high level of crystallinity. The presence of any secondary phases or spurious peaks has not been observed [3].

The condition for a sharp peak in the intensity of scattered radiation from a crystal is

$$n\lambda = 2d_{hkl} \sin(\theta), \quad (62)$$

where d_{hkl} is the distance between planes of Miller indices (hkl)

$$d_{hkl} = \left[\frac{h^2}{a^2} + \frac{k^2}{b^2} + \frac{l^2}{c^2} \right]^{-1/2}, \quad (63)$$

and a , b , and c are the lattice dimensions. The diffraction maxima in Figure 15 occur for the GaN:Yb(0002) and GaN:Yb(0004) planes at $2\theta = 34.66^\circ$ and $2\theta = 73.14^\circ$, respectively. From (63), $d_{0002} = c/2$ and $d_{0004} = c/4$. Substituting these values into

(62) and letting $n = 1$ gives

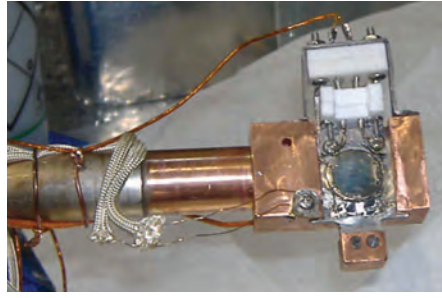
$$\begin{aligned}
(0002) : \quad c &= \left(\frac{\lambda}{\sin \theta} \right) = \left(\frac{1.5406}{\sin(34.66/2)} \right) \\
&= 5.172 \text{ \AA}, \\
(0004) : \quad c &= \left(\frac{2\lambda}{\sin \theta} \right) = \left(\frac{2(1.5406)}{\sin(73.14/2)} \right) \\
&= 5.172 \text{ \AA},
\end{aligned}$$

which is slightly larger, but in good agreement, with the undoped GaN c -axis length of 5.166 Å. The same analysis of other GaN:RE samples produced similar results.

3.2 Sample Surface Preparation

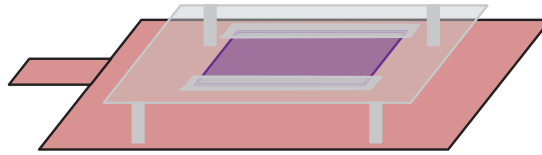
The physical dimensions of the sample holder ($\sim 8 \text{ mm} \times 8 \text{ mm}$) required some thin films to be cut using a South Bay Technologies Model 650 low-speed diamond wheel saw. The GaN:RE thin film samples were then rinsed in ethanol and air-dried. Next, electrical contact was established between the thin film sample, tantalum mounting plate, and molybdenum sample holder using several spot welds. Figure 16 shows a typical configuration of the above mentioned contacts. The sample holder was then loaded into a preparation chamber and vacuum conditions to $\sim 10^{-9}$ Torr were established, which typically required 6–10 hours. Next, a manipulator arm transferred the sample holder from the preparation chamber to the sample chamber and inserted the holder into the copper receiving block. Finally, vacuum conditions to $\sim 10^{-10}$ Torr were established, which typically required less than one hour.

Atomically clean sample surfaces were obtained by several sputtering and annealing cycles. Typically, sputtering occurred via Ar^+ ion bombardment at $\pm 45^\circ$ with respect to the sample normal for 20 minutes in each orientation. Next, resistive heat-



(a) Top view of sample holder.

- Molybdenum sample holder
- Tantalum plate / strips
- Sample film



(b) Side view schematic of sample holder.

Figure 16. Sample mounting technique used at the Center for Advanced Microstructures and Devices.

ing to a temperature of approximately 500 K via a tungsten filament located behind the sample holder, followed by gradual return to room temperature, annealed the sample surface.

3.3 Photoemission Spectroscopy Considerations

Many of the considerations discussed here are specific to the experimental setup at the Center for Advanced Microstructures and Devices, but most apply to the XPS experiment conducted at the University of Nebraska (Lincoln), as well.

Every photoemission experiment begins with a photon source. At the CAMD synchrotron, electron packets are accelerated through an underground linear accelerator into a current storage ring inside the experimental hall. Within the storage ring, magnetic fields impart a Lorentz force on the electrons, which are subsequently turned and accelerated. This acceleration results in photon emission perpendicular

to the direction of electron propagation. Next, the photons travel through a series of optics, which produce monochromatic, linearly polarized light that is used to irradiate a sample. Figure 17 shows a cross section sketch of the 3-meter toroidal grating monochromator (3m TGM) experimental setup used for all experiments conducted at CAMD.

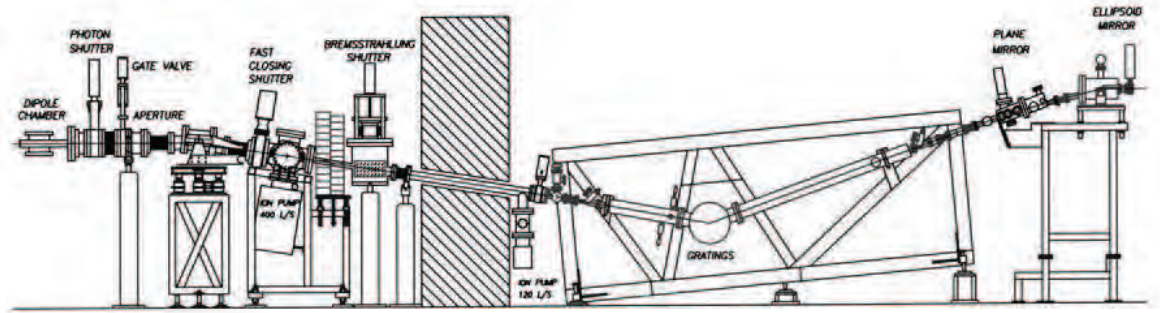


Figure 17. Schematic of the 3-meter Toroidal Grating Monochromator (3m TGM) beamline at the Center for Advanced Microstructures and Devices [4].

Sample irradiation results in photoelectron emission with a range of energies and directions, and there are several components required to efficiently filter these electron kinetic energies, as depicted schematically in Figure 18. The electron optics, which are typically a set of electrostatic or magnetic lenses, allow a portion of the photoelectrons at the correct acceptance angle and of a given energy, referred to as the pass energy, to arrive at the analyzer entrance slit. More specifically, photoelectrons of the specified pass energy are measured by setting voltages for the lens system that both focus electrons onto the entrance and that retard the electron velocity so that their kinetic energy after passing through the transfer lenses matches the pass energy of the hemispherical analyzer. Therefore, in order to record an electron kinetic energy spectrum over a range of energies, it is necessary to scan the voltages applied to the transfer lenses, referred to as a lens function.

Photoelectrons that pass through the entrance slit travel through the hemispherical electron energy analyzer, subject to the applied $1/r$ field between the two concen-

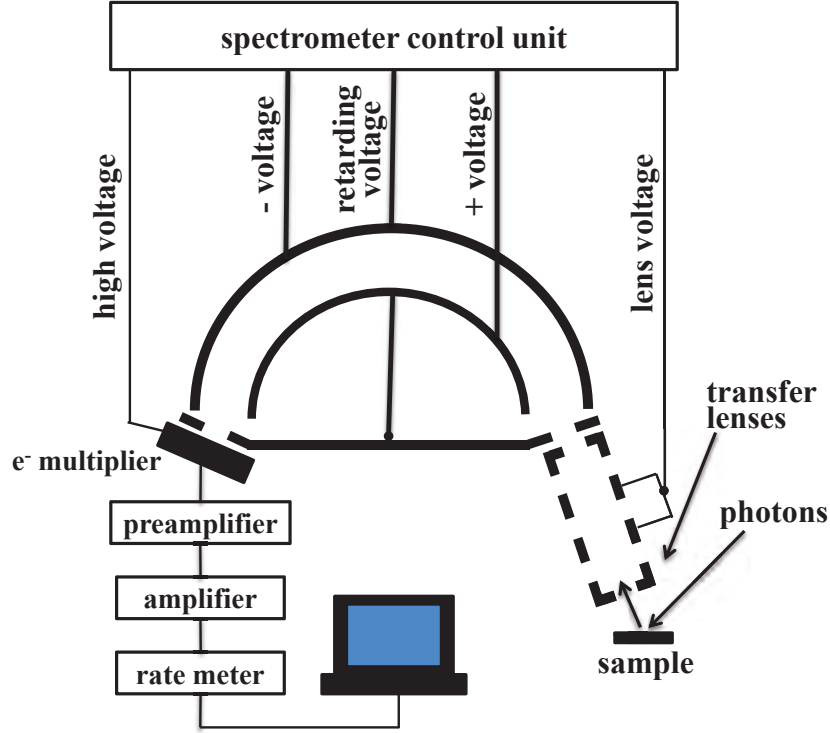


Figure 18. Typical layout for electron kinetic energy analysis.

tric hemispheres, and depart through the analyzer exit slit. The departing electrons are then multiplied via an electron multiplier and counted via electronics and data collection software.

The energy resolution of the analyzer ΔE is dependent on the slit width W , mean radius R , acceptance angle α , and pass energy E_p as [5]

$$\Delta E = E_p \left(\frac{W}{2R} + \frac{\alpha^2}{2} \right). \quad (64)$$

The 3m TGM configuration is equipped with a 50 mm hemispherical electron energy analyzer [4] with an acceptance angle of $\pm 1^\circ$; pass energy was typically set to 15 V. The operational range is 15–200 eV, and the combined resolution of the photoemission configuration, to include the monochromator, all optics, and the electron analyzer is about 70 meV for photon energies up to 140 eV. At higher photon

energies, the combined beamline/analyzer resolution is about 150 meV [4].

3.4 Photoemission Spectra Conditioning

3.4.1 Conversion to Binding Energy.

Photoemission spectroscopy requires establishing a meaningful reference level to set the energy scale. Although the kinetic energies of photoelectrons are measured, spectra are typically displayed in binding energies relative to the Fermi edge of the sample. In a semiconductor, the Fermi level is not the best reference level, as it shifts around in the bandgap at the surface due to changes in band bending and doping (n or p) type. However, the Fermi level of a metal is not susceptible to these variations. Thus, the accepted practice [6–9] is to use a clean metal foil to determine the conversion from the measured kinetic energy to the binding energy, as depicted graphically in Figures 19–21.

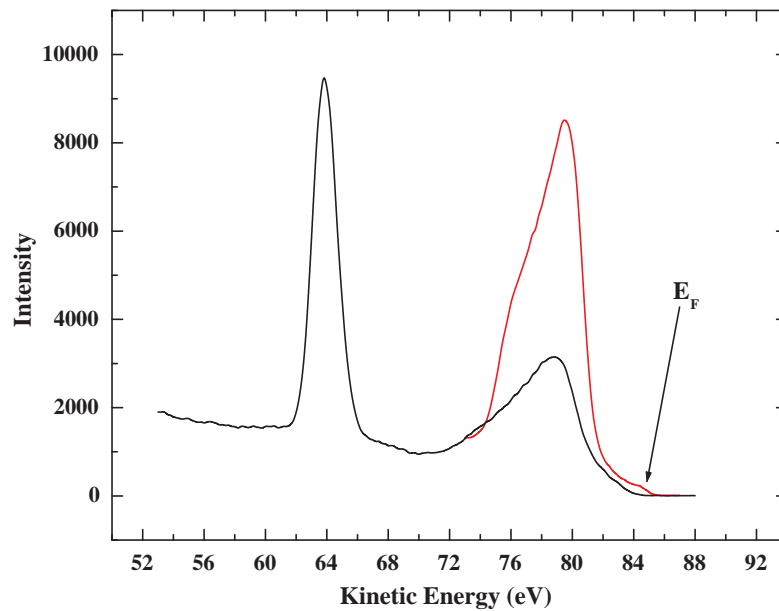


Figure 19. Raw spectra of intensity versus kinetic energy for GaN:Yb (black) and tantalum foil (red) using 90 eV photons.

Figure 19 shows the raw spectra of intensity versus kinetic energy for GaN:Yb and a clean tantalum foil. The spectrum for tantalum indicates the presence of a density of states nearby 85 eV that resembles the Fermi-Dirac distribution

$$f(E) = \frac{1}{e^{(E-E_F)/k_B T} + 1} . \quad (65)$$

Inspection of (65) shows that $f(E_F) = 1/2$. Thus, fitting (65) against the experimental data at the appropriate temperature and such that $f(E) = 1/2$ at $E = E_F$ provides a good estimate of the kinetic energy of the Fermi level, as shown in Figure 20 at $T = 300$ K. The kinetic energy of the Fermi level E_F permits shifting from a

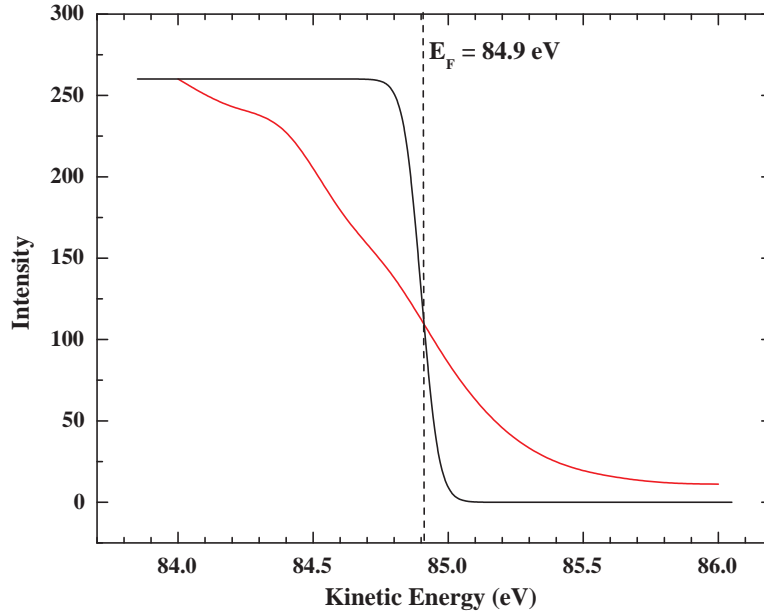


Figure 20. Kinetic energy of spectrometer Fermi level using 90 eV photons. The Fermi level is established at the intersection between the Fermi-Dirac distribution (65) at $T = 300$ K (black) and the experimentally observed tantalum density of states (red).

kinetic energy to a binding energy scale as

$$E_B = E_{\text{kin}} - E_F , \quad (66)$$

such that $E_B = 0$ at the Fermi level with all other binding energies expressed as negative values. The converted GaN:Yb spectrum of intensity versus binding energy is shown in Figure 21. The valence band maximum, which is determined by

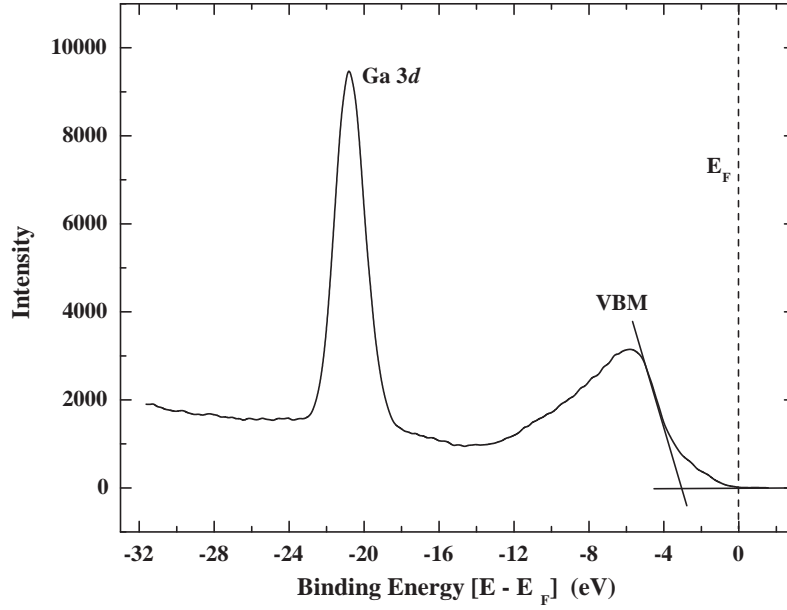


Figure 21. Raw spectrum of intensity versus binding energy for GaN:Yb using 90 eV photons. The valence band maximum (VBM) is located by linear extrapolation of the high kinetic energy edge of the spectrum at the intersection of zero background.

linear extrapolation of the high kinetic energy edge of the spectrum, is located at approximately 2.7 eV below the Fermi level for the GaN:Yb sample shown. Also, the dominant spectral feature located at a binding energy of approximately -20.5 eV is the Ga 3d shallow core electronic level. Therefore, the separation between the valence band maximum and the Ga 3d shallow core level in GaN:Yb is consistent with the accepted value of 17.7 eV for wurtzite GaN [8–10].

The detailed method of fitting the Fermi-Dirac distribution to the experimental data is shown for completeness. In practice, visual interpolation of the Fermi level is sufficient and was the method used. Additionally, the kinetic energy corresponding to the Fermi level is a unique photon energy dependent value. Thus, in theory, the

Fermi level would need to be determined for every photon energy used during an experiment. In practice, however, the 3m TGM beamline historical files contain a calibration database which provides the Fermi level kinetic energy for various photon energies throughout the operating range, such that values not included in the database are easily interpolated. During this research, the calibration database was both verified and updated, in order to ensure accuracy.

3.4.2 Removal of Background and Secondary Electron Signals.

After converting spectra to a binding energy scale, the background was adjusted to zero and secondary electron influence was removed. Electrons with binding energies above E_F in a semiconductor should not be collected during photoemission, so photoemission intensities at values greater than E_F were subtracted from the spectra. The secondary electron signal I_s influences PES spectra by increasing exponentially with decreasing kinetic energy, as

$$I_s(\text{KE}) = Ae^{-(B \cdot \text{KE})}, \quad (67)$$

where A and B are fitting parameters. Therefore, a parametric fit for (67) can be determined by using several intensity values at locations away from primary spectral features, and the resulting equation can be subtracted from each spectrum. In practice, this was accomplished using the Origin Baseline Toolkit with 6–10 values, dependent upon the GaN:RE sample spectra, and the resulting baseline was subtracted from all spectra associated with the specific sample. Figure 22 illustrates this technique.

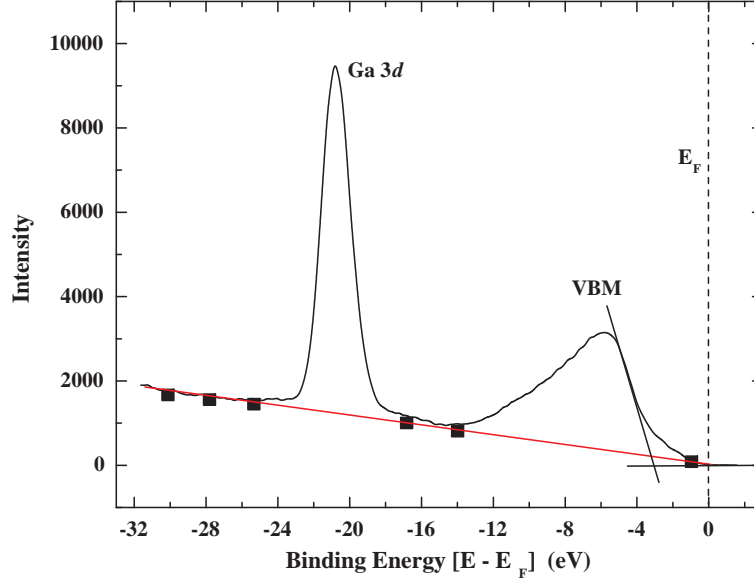


Figure 22. Removal of secondary electron influence using Origin Baseline Toolkit. Several intensity values (squares) are used to fit a baseline (red) via (67), which is subtracted from the sample spectra.

3.4.3 Spectra Normalization.

The next step of the spectral conditioning process requires spectra to be adjusted for intensity variations caused by the experimental conditions. The electron ring current at CAMD experiences an exponential decay during normal operation, which requires regular (typically 3 times per day) electron re-injections. Hence, the absolute intensities of both the ring current and the photon flux at the 3m TGM beamline endstation vary greatly during experiments. However, as both the resonant photoemission and Schottky barrier experiments required comparison of the relative intensities of many spectra, each individual spectrum was normalized to points away from the major spectral features.

Using Figure 22 as an example, the saddle between the valence band and the Ga 3d shallow core level was identified as the reference level for that spectrum. Next, the average absolute intensity of three data points within 0.3 eV was used to calculate

the intensity of the spectrum at the reference point as I_{rp} ; this process was repeated for each individual spectrum. The largest value of intensity at the reference point for all spectra was then designated as $I_{\text{rp, max}}$. Finally, the absolute intensity of each individual spectrum I_0 was scaled to I_S as

$$I_S = R \cdot I_0; \quad R = \frac{I_{\text{rp, max}}}{I_{\text{rp}}} \quad (68)$$

where R is the scaling factor.

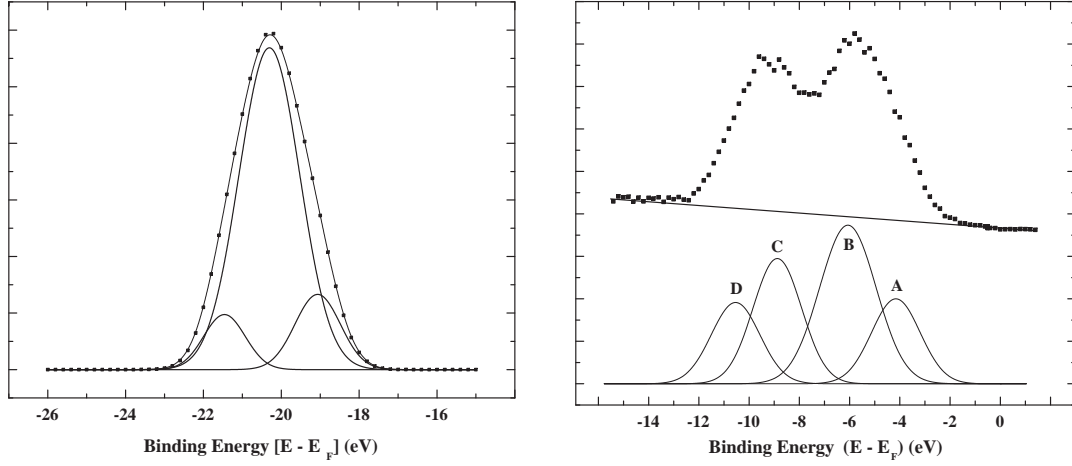
The technique presented here for Figure 22 applied to the GaN:Yb sample only. Each rare earth doped GaN thin film had unique spectral features, so the reference points used to normalize spectra were slightly different for the different rare earth dopants studied, as would be expected. Lastly, the intensities presented in Chapters IV, V, and VI are relative intensities, unless stated otherwise.

3.4.4 Spectral Feature Deconvolution.

The final step of PES spectra conditioning is to deconvolute the features of each spectrum into their subpeaks. Photoemission from the core level of an atom produces a Lorentzian lineshape, where the lifetime of the state determines linewidth [11]. In a metal, the intrinsic process of electron-hole pair production via photoemission leads to the selection of an asymmetric Doniach-Sunjic [12] or Mahan [13] lineshape to represent the core level. However, in a semiconductor (insulator), the asymmetric lineshapes are difficult to observe as differential charging adds a symmetric contribution to linewidth [11]. Moreover, the influence of Heisenberg's uncertainty principle to the lifetime of a state, combined with the effects of electron-phonon coupling further broaden the core level and yield a more symmetric lineshape. Therefore, the collective effects of these processes on GaN:RE core levels indicated a least squares fitting of Gaussian line shapes as the logical choice to represent spectral feature

subpeaks.

Figures 23(a) and 23(b) show the Ga $3d$ shallow core level and valence band deconvolution for two different rare earth doped GaN samples. The full width at



(a) Deconvolution of Ga $3d$ shallow core level from GaN:Gd photoemission spectrum. (b) Deconvolution of GaN:Er valence band spectrum using multiple Gaussian subpeaks.

Figure 23. Deconvolution of valence band and shallow core level lineshapes from example GaN:RE photoemission spectra.

half peak maximum for all Gaussians exceeded the overall system resolution of 0.5 eV for all experiments. Further justification for the number, location, and identification (surface, core, alloy) of valence band and shallow core level subpeaks for the different rare earth doped GaN thin films will be discussed in Chapters V and VI.

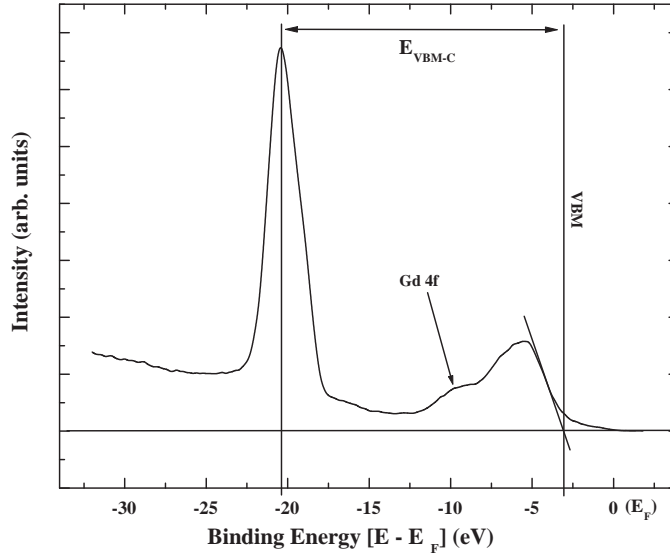
Discussions presented here and in Chapters IV and V provide all details pertaining to data analysis for the respective experiments. However, a few special considerations for Schottky barrier height measurement require additional explanation.

3.5 Schottky Barrier Considerations

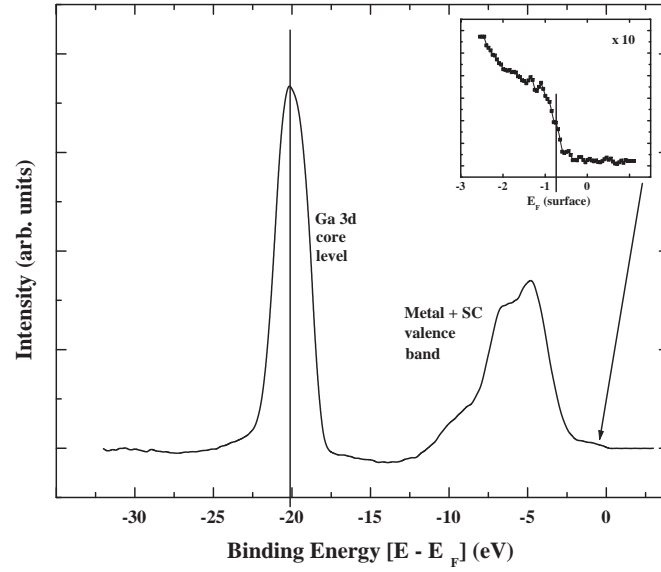
Recall from Chapter II that the Schottky barrier height at the metal-semiconductor interface may be determined experimentally as

$$\Phi_{B,n} = E_g - (E_F - E_V). \quad (69)$$

During metal deposition, alignment of the metal and semiconductor Fermi levels results in an upward valence band bending, as shown in Figure 10 of Chapter II. Band bending may be expected to manifest in the photoemission spectra as a shift of the valence band maximum toward the Fermi level with increased metal deposition, from which $\Phi_{B,n}$ can be calculated via (69). However, the difficulty in interpreting mixed metal-semiconductor photoemission spectra lies in the fact that as metal is deposited onto the semiconductor surface, the semiconductor valence band edge becomes obscured by the metal overlayer signal. Surface Fermi level movement and valence band bending were determined by monitoring the Ga $3d$ core level shift as a function of Au coverage. Figure 24(a) shows the Ga $3d$ core level and the valence band region spectra on the surface for a clean GaN:Gd surface. The energy between these two levels, $E_{\text{VBM-C}}$, is considered a bulk property of the material and is, therefore, independent of metal coverage [6,8,9]. When metal is evaporated on the sample surface, as shown in Figure 24(b), the edge of the semiconductor valence band maximum is obscured by the signal originating from the metal overlayer. Whereas the Fermi level of the metal, which coincides with the surface Fermi level of the semiconductor, can now be observed (Figure 24(b) inset), the valence band maximum of the semiconductor is no longer visible. However, owing to the fact that $E_{\text{VBM-C}}$ is constant, the Ga $3d$ core shift results in an equivalent valence band bending at the semiconductor surface, from which the Schottky barrier height is calculated via (69).



(a) Photoemission spectrum, in binding energy, for a clean GaN:Gd thin film showing the Ga 3d core level peak and the valence band region. A least squares fit is used to determine the valence band maximum (VBM). The value of $E_{\text{VBM-C}}$, shown by the double arrow, is determined from these features.



(b) Photoemission spectrum for GaN:Gd thin film with $\sim 3 \text{ \AA}$ Au coverage. The Fermi edge of the metal (inset) indicates the Fermi level position at the semiconductor surface. The core level shift, as compared with the clean spectrum, determines the semiconductor valence band surface band bending.

Figure 24. Semiconductor surface valence band bending via core level shift.

References

- [1] R. C. Jaeger, *Introduction to Microelectronic Fabrication*. Prentice Hall, 2002.
- [2] D. B. Chrisey and G. K. Hubler, *Pulsed laser deposition of thin films*. New York: John Wiley and Sons, 1994.
- [3] S. R. McHale, J. W. McClory, J. C. Petrosky, J. Wu, R. Palai, P. A. Dowben, and I. Ketsman, “The effective surface debye temperature of Yb:GaN,” *Materials Letters*, vol. 65, p. 1476, 2011.
- [4] Y. Losovyj, I. Ketsman, E. Morikawa, Z. Wang, J. Tang, and P. Dowben, “Optimization of the 3m TGM beamline, at CAMD, for constant initial state spectroscopy,” *Nuclear Inst. and Methods in Physics Research, A*, vol. 582, no. 1, pp. 264–266, 2007.
- [5] “Alpha 110 Hemispherical Electron Energy Analyzer Application Note AN30054 E,” Thermo Electron Corporation, online at http://www.datacompscientific.com/TVGS/A110_AN31054_DS.pdf.
- [6] K. A. Rickert, A. B. Ellis, J. K. Kim, J. L. Lee, F. J. Himpsel, F. Dwikusuma, and T. F. Kuech, “X-ray photoemission determination of the Schottky barrier height of metal contacts to *n*-GaN and *p*-GaN,” *Journal of Applied Physics*, vol. 92, p. 6671, 2002.
- [7] C. I. Wu and A. Kahn, “Investigation of the chemistry and electronic properties of metal/gallium nitride interfaces,” *Journal of Vacuum Science & Technology B: Microelectronics and Nanometer Structures*, vol. 16, p. 2218, 1998.
- [8] A. Barinov, L. Casalis, L. Gregoratti, and M. Kiskinova, “Stages of formation and thermal stability of a gold-*n*-GaN interface,” *Journal of Physics D: Applied Physics*, vol. 34, pp. 279–284, 2001.
- [9] L. Casalis, A. Barinov, L. Gregoratti, and M. Kiskinova, “Au/GaN interface: initial stages of formation and temperature-induced effects,” *Physical Review B*, vol. 63, no. 8, p. 85308, 2001.
- [10] M. H. Kim, S. N. Lee, C. Huh, S. Y. Park, J. Y. Han, J. M. Seo, and S. J. Park, “Interfacial reaction and Fermi level movement induced by sequentially deposited metals on GaN: Au/Ni/GaN,” *Physical Review B*, vol. 61, no. 16, pp. 10 966–10 971, 2000.
- [11] S. Hüfner, *Photoelectron Spectroscopy: Principles and Applications*. Springer-Verlag, 2003.
- [12] S. Doniach and M. Sunjic, “Many-electron singularity in X-ray photoemission and X-ray line spectra from metals,” *Journal of Physics C: Solid State Physics*, vol. 3, p. 285, 1970.

- [13] G. D. Mahan, “Collective excitations in x-ray spectra of metals,” *Physical Review B*, vol. 11, no. 12, p. 4814, 1975.

IV. The Effective Surface Debye Temperature of Yb:GaN

The contents of this chapter were published in reference [1]. The effective Debye temperatures of ytterbium and gallium in Yb:GaN thin films have been obtained using X-ray photoemission spectroscopy. The vibrational motion normal to the surface results in a diminution of photoemission intensities from which we have estimated the effective Debye temperatures of 221 ± 30 K and 308 ± 30 K for Yb and Ga, respectively. The difference between the measured values for Yb and Ga suggests that the Debye temperatures are influenced by the local environment. The smaller effective surface Debye temperature for Yb correlates to a soft, strained surface, possibly due to an increased Yb–N bond length as compared to the Ga–N bond length.

4.1 Introduction

During the past decade, rare earth doped semiconductors have generated considerable attention for their application in new optoelectronic devices [2–5]. The favorable thermal, chemical, and electronic properties of wide band gap, III-nitride semiconductors suggest device feasibility using lanthanide doped AlN and GaN. Moreover, the tunable bandgaps of these III-nitride alloys offer device applications across the visible spectrum through the ultra-violet range, to include optically stimulated lasers [6], $p - n$ junction light emitting diodes [7], and thin film electroluminescence of phosphors [8–10].

Phonon mediated exciton decay can lead to line broadening and spectral deformation. While phonons can affect excited state lifetimes, so too can the carrier concentration and local structural deformation. A signature of phonon mediated processes would be a low effective Debye temperature. The true surface Debye temperature, containing the in-plane and anharmonic motions, is difficult to measure in most surface spectroscopies [11]. However, the effective surface Debye temperature

is readily obtained using X-ray photoemission spectroscopy (XPS) and ultraviolet photoemission, low energy electron diffraction, inverse photoemission spectroscopy, and other surface sensitive techniques [12–22]. The experimentally derived effective surface Debye temperature is dominated by the dynamic motion of vibrational modes normal to the surface and tends to be independent of surface orientation [11, 19]. Increased thermal vibrations dictate that the intensity of an emitted or scattered electron beam decays exponentially with increasing temperature as [12–22]

$$I = I_0 \exp(-2W), \quad (70)$$

where W is the Debye-Waller factor and is given by

$$2W = |\Delta k|^2 \langle u_0 \rangle^2, \quad (71)$$

where Δk is the wave vector transfer and $\langle u_0 \rangle^2$ is the mean square displacement of the atoms. Within the Debye model of thermal vibrations, in the case of isotropic vibrations, W is described as

$$2W = \frac{3\hbar^2(\Delta k)^2 T}{m k_B \Theta_D^2}, \quad (72)$$

where $\hbar(\Delta k)$ is the electron momentum transfer, T is the temperature of the sample (in Kelvin), m is the mass of the scattering center, k_B is the Boltzmann constant, and Θ_D is the effective surface Debye temperature. In the case of photoemission spectroscopy, the momentum transfer is equal to the momentum of the emitted electron [12–22], and the scattering center mass is the mass of the specific element from which the emitted photoelectron originates [17]. This chapter reports the effective surface Debye temperatures of Ga and Yb via XPS spectra taken from Yb:GaN thin films and correlates the results with thin film strain.

4.2 Experimental

Thin films of $\text{Yb}_x\text{Ga}_{1-x}\text{N}$ (50–300 nm) were fabricated on Si(111) substrates by RF plasma (EPI 620) assisted molecular beam epitaxy (MBE). The growth parameters for the deposition of Yb doped (*in situ*) GaN thin films were base pressure of $\sim 10^{-11}$ Torr, nitrogen flux of 0.75–1.0 SCCM, RF power of 500 W, substrate temperature of 850–900 °C, Ga cell temperature of 850 °C, and Yb cell temperature of 500–850 °C. Thickness of the films was measured with a surface profilometer. The orientation, crystal structure, and phase purity of the films were established by Cu K_α ($\lambda=1.5406$ Å) radiation X-ray diffraction, as shown in Figure 25, using a Siemens D5000 X-ray diffractometer.

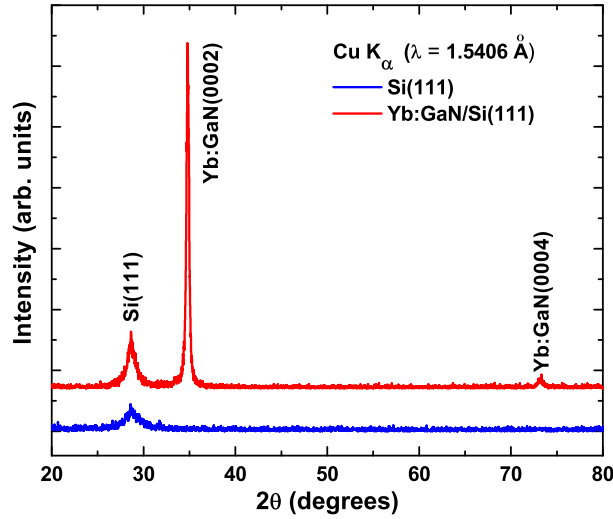


Figure 25. The X-ray diffraction (XRD) pattern of a GaN:Yb film grown on Si(111) substrates. The films show *c*-axis orientation of the texture growth and a high level of crystallinity. The presence of any secondary phases or spurious peaks has not been observed.

Surface adsorbates were removed by several preparatory sputtering and thermal annealing cycles in ultra high vacuum (UHV). The resulting surfaces were characterized by core level XPS and found to be free of oxygen. The XPS studies were performed in an UHV chamber with a hemispherical electron analyzer (Thermo VG

Scientific VG100AX). The combined resolution of the system was about 1.1 eV using a Mg K_α line (1253.6 eV) from a fixed anode X-ray source. Surface temperature was controlled by a combination of resistive heating and cooling with liquid nitrogen. The temperature was monitored with a W-5%Re/W-26%Re thermocouple with an accuracy of 5 K. The photoemission spectra were taken with a 45° incidence angle and normal emission, with binding energies referenced to the Fermi level of a clean Ta foil.

4.3 Results and Discussion

As anticipated, the core level photoemission intensities decrease with increasing temperature, as shown in Figures 26(a) and 26(b). Figure 27 shows the logarithm of the core peak photoemission intensities for Ga 3*p* and Yb 4*d* as a function of temperature. The kinetic energy of the outgoing photoelectron is calculated as

$$E_{\text{kin}} = h\nu - |E_B| - \phi_a, \quad (73)$$

where $h\nu$ is the incident photon energy, $|E_B|$ is the binding energy of the emitted photoelectron, and ϕ_a is the electron analyzer work function (4.5 eV). Thus, Δk values in Figure 27 are calculated from

$$(\Delta k)^2 = \frac{2m_e E_{\text{kin}}}{\hbar^2}, \quad (74)$$

where m_e is the electron mass. From (70) and (72), the slope S for each XPS data set in Figure 27 determines Θ_D from

$$|S| = \frac{3\hbar^2(\Delta k)^2}{m k_B \Theta_D^2}. \quad (75)$$

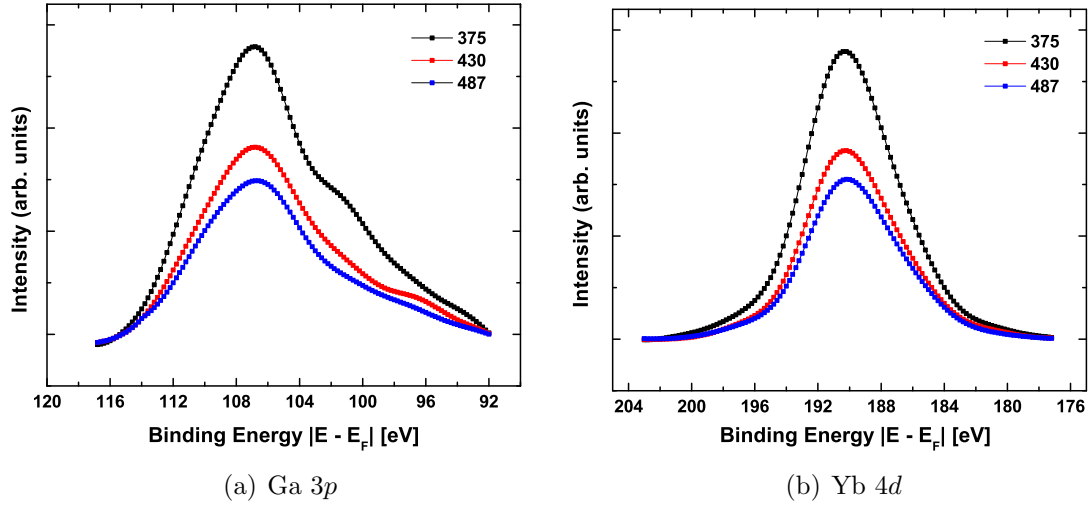


Figure 26. Temperature dependent X-ray photoemission spectra of the indicated core levels after background subtraction.

The fact that the effective Debye temperature is different for ytterbium and gallium in a Yb:GaN thin film indicates that this effective Debye temperature is influenced by the local environment, not exclusively by the overall rigidity of the thin film lattice. The difference between the measured effective Debye temperatures for Ga and Yb provides an indication of the surface rigidity and lattice strain. In a simple picture, examination of equations (71) and (72) predicts an inverse relationship between atomic displacement and surface Debye temperature such that an increased Θ_D predicts lower atomic displacement, or a “rigid” surface. It follows that a decreased Θ_D is indicative of a “soft” surface. Thus, our respective values of 221 ± 30 K and 308 ± 30 K for the effective Yb and Ga Debye temperatures in Yb:GaN reflect softening from the introduction of Yb atoms into the GaN wurtzite crystal structure.

If our measured effective Debye temperatures for Yb and Ga were identical, within experimental uncertainty, it would be indicative of a substitutional occupation of a Ga site by a Yb ion. Although the measured effective Debye temperatures were not identical, the experimental uncertainty indicates that the Yb and Ga Debye

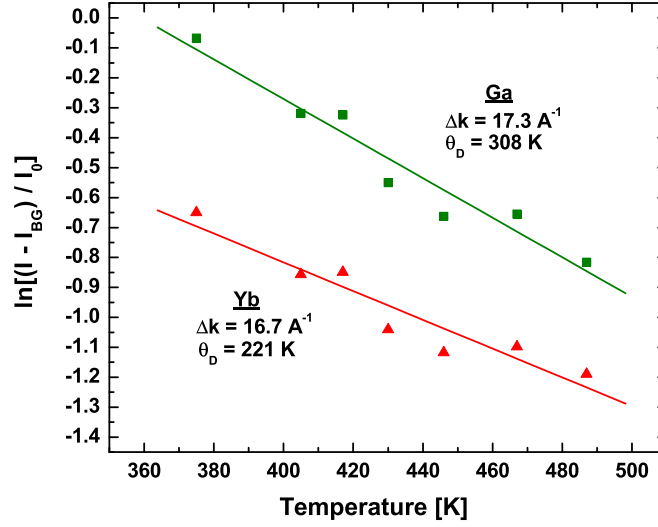


Figure 27. Logarithm of the core peak photoemission intensities for Yb and Ga as a function of temperature following background (I_{BG}) subtraction and normalization to the peak intensity at the lowest temperature I_0 . The experimental values were fitted (solid line) with the Debye-Waller factor.

temperatures could differ by as little as 27 K. This similarity between the Yb and Ga Debye temperatures suggests that Yb doping does occur by Ga site substitution. Experimental data and crystal-field calculations have confirmed that rare earth ions in a GaN host occupy relaxed substitutional Ga sites [2,3]. To explain the slight difference in the Debye temperatures, strain should be considered.

From the standpoint of bond length, shorter bonds have higher binding energies than longer ones, which implies that decreasing the bond distance reflects stiffening and increasing bond distance reflects softening. Thus, the slightly lower calculated effective Debye temperature for Yb in Yb:GaN reveals a softened surface, and we contend that this softening arises from a lengthening of the Yb–N bond distance, as compared with the Ga–N distance, which would manifest as thin film strain. The decrease in Debye temperature should be reflected in a decrease in exciton lifetime as this means that new phonon decay channels are opened. This in turn should lead to an increase in fluorescence peak widths.

From Figure 25, the c -axis length of our Yb:GaN thin films was found to be

approximately 5.172 Å, which is slightly larger than the widely reported and accepted c -axis length of undoped GaN (5.166 Å). The XRD data are limited because the films are so very nearly crystalline, that is to say highly textured. There will be changes to the a - and b -axis lengths in response to contraction or transverse strain, as dictated by Poisson’s ratio. However, the implementation of Poisson’s ratio depends on the details of the stress-strain tensor, which cannot be determined accurately from our experimental data. Thus, the values for the a -axis and b -axis cannot be accurately established from our data, but would require additional measurements like grazing incidence X-ray scattering. However, the small increase in c -axis lattice constant, and hence thin film strain, can be explained due to the fact that the Yb^{3+} ion has a larger ionic radius than the Ga^{3+} ion by at least 40%.

The tetrahedral arrangement of four nearest neighbors in wurtzite GaN yields a Ga^{3+} ionic radius of 0.47 Å according to [23], and others. Regarding Yb doping in GaN, references have not been found for the Yb^{3+} ionic radius in the same configuration. However, the available data indicate ionic radii for Yb^{3+} ranging from 0.87–1.04 Å for a coordination number of VI-IX. Similarly, the range of ionic radii for Ga^{3+} are 0.47–0.62 Å for a coordination number of IV-VI. Therefore, in the absence of a Yb^{3+} data point with coordination = 4, then the most conservative comparison using the largest possible documented ionic radius for Ga^{3+} (0.62 Å) and the smallest possible documented ionic radius for Yb^{3+} (0.87 Å) further supports the claim of doping-induced thin film strain due to increased Yb–N bond length, compared with the Ga–N bond length.

4.4 Conclusions

X-ray photoemission spectroscopy has been used to determine the effective Debye temperatures of gallium and ytterbium in Yb:GaN thin films. The similarity between their measured values suggests that substitutional occupation of a Ga site by a Yb

ion occurs, which supports experimental data and theoretical calculations. Careful comparison of the Ga and Yb values indicates that the slightly smaller effective Debye temperature of the Yb atom reflects a surface that is softened and strained, possibly due to an increased Yb–N bond length as compared to the Ga–N bond length.

References

- [1] S. R. McHale, J. W. McClory, J. C. Petrosky, J. Wu, R. Palai, P. A. Dowben, and I. Ketsman, “The effective surface debye temperature of Yb:Ga_N,” *Materials Letters*, vol. 65, p. 1476, 2011.
- [2] T. Koubaa, M. Dammak, M. Kammoun, W. M. Jadwisieniczak, and H. J. Lozykowski, “Crystal field and Zeeman parameters of substitutional Yb³⁺ ion in GaN,” *Journal of Alloys and Compounds*, vol. 496, no. 1-2, pp. 56–60, 2010.
- [3] T. Koubaa, M. Dammak, M. Kammoun, W. M. Jadwisieniczak, H. J. Lozykowski, and A. Anders, “Spectra and energy levels of Yb³⁺ in AlN,” *Journal of Applied Physics*, vol. 106, no. 1, p. 013106, 2009.
- [4] W. M. Jadwisieniczak and H. J. Lozykowski, “Optical properties of Yb ions in GaN epilayer,” *Optical Materials*, vol. 23, no. 1-2, pp. 175–181, 2003.
- [5] A. J. Kenyon, “Recent developments in rare-earth doped materials for optoelectronics,” *Progress in Quantum Electronics*, vol. 26, no. 4-5, pp. 225–284, 2002.
- [6] J. H. Park and A. J. Steckl, “Effect of process conditions on gain and loss in GaN: Eu cavities on different substrates,” *Physica Status Solidi A*, vol. 205, no. 1, pp. 26–29, 2008.
- [7] A. Nishikawa, T. Kawasaki, N. Furukawa, Y. Terai, and Y. Fujiwara, “Room-temperature red emission from a p-type/europium-doped/n-type gallium nitride light-emitting diode under current injection,” *Applied Physics Express*, vol. 2, no. 7, p. 1004, 2009.
- [8] A. J. Steckl, J. Heikenfeld, D. S. Lee, and M. Garter, “Multiple color capability from rare earth-doped gallium nitride,” *Materials Science and Engineering B*, vol. 81, no. 1-3, pp. 97–101, 2001.
- [9] J. H. Tao, N. Perea-Lopez, J. McKittrick, J. B. Talbot, K. Klinedinst, M. Raukas, J. Laski, K. C. Mishra, and G. Hirata, “Synthesis of rare-earth activated AlN and GaN powders via a three-step conversion process,” *Physica Status Solidi C*, vol. 5, no. 6, pp. 1889–1891, 2008.

- [10] J. Shi, M. V. S. Chandrashekhara, J. Reiherzer, W. Schaff, J. Lu, F. Disalvo, and M. Spencer, "High intensity red emission from Eu doped GaN powders," *Physica Status Solidi C*, vol. 5, no. 6, pp. 1495–1498, 2008.
- [11] C. Waldfried, D. N. McIlroy, J. Zhang, P. A. Dowben, G. A. Katrich, and E. W. Plummer, "Determination of the surface Debye temperature of Mo (112) using valence band photoemission," *Surface Science*, vol. 363, no. 1-3, pp. 296–302, 1996.
- [12] K. Fukutani, N. Lozova, S. M. Zuber, P. A. Dowben, P. Galiiy, and Y. B. Losovyj, "Order-disorder transition for corrugated Au layers," *Applied Surface Science*, vol. 256, p. 4796–4800, 2010.
- [13] D. Q. Feng, P. A. Dowben, R. Rajesh, and J. Redepenning, "The anomalous stiffness of biphenyldimethyldithiol," *Applied Physics Letters*, vol. 87, p. 181918, 2005.
- [14] H. K. Jeong, R. Skomski, C. Waldfried, T. Komesu, P. A. Dowben, and E. Vescovo, "The effective spin dependent Debye temperature of Gd (0001)," *Physics Letters A*, vol. 324, no. 2-3, pp. 242–246, 2004.
- [15] Y. B. Losovyj, I. N. Yakovkin, H. K. Jeong, D. Wisbey, and P. A. Dowben, "Lattice-stiffening transition in gadolinium chains on furrowed (112) surfaces," *Journal of Physics: Condensed Matter*, vol. 16, p. 4711, 2004.
- [16] P. V. Schwartz, D. J. Lavrich, and G. Scoles, "Overlayers of long-chain organic molecules physisorbed on the surface of self-assembled monolayers of alkylthiols on Au (111)," *Langmuir*, vol. 19, no. 12, pp. 4969–4976, 2003.
- [17] H. K. Jeong, T. Komesu, P. A. Dowben, B. D. Schultz, and C. J. Palmstrøm, "The anomalous effective surface Debye temperature of ErAs (100)," *Physics Letters A*, vol. 302, no. 4, pp. 217–223, 2002.
- [18] C. N. Borca, T. Komesu, H. Jeong, P. A. Dowben, D. Ristoiu, C. Hordequin, J. Pierre, and J. P. Nozieres, "Effective surface Debye temperature for NiMnSb (100) epitaxial films," *Applied Physics Letters*, vol. 77, p. 88, 2000.
- [19] C. N. Borca, J. Choi, S. Adenwalla, S. Ducharme, P. A. Dowben, L. Robertson, V. M. Fridkin, S. P. Palto, and N. Petukhova, "Influence of dynamical scattering in crystalline poly (vinylidene fluoride-trifluoroethylene) copolymers," *Applied Physics Letters*, vol. 74, p. 347, 1999.
- [20] N. Camillone, C. E. D. Chidsey, G. Liu, T. M. Putvinski, and G. Scoles, "Surface structure and thermal motion of n-alkane thiols self-assembled on Au (111) studied by low energy helium diffraction," *The Journal of Chemical Physics*, vol. 94, p. 8493, 1991.

- [21] B. P. Tonner, H. Li, M. J. Robrecht, Y. C. Chou, M. Onellion, and J. L. Erskine, “Temperature dependence of photoelectron scattering from a monolayer,” *Physical Review B*, vol. 34, no. 6, pp. 4386–4389, 1986.
- [22] R. S. Williams, P. S. Wehner, J. Stöhr, and D. A. Shirley, “Thermally induced breakdown of the direct-transition model in copper,” *Physical Review Letters*, vol. 39, no. 5, pp. 302–305, 1977.
- [23] “Database of ionic radii,” online at <http://abulafia.mt.ic.ac.uk/shannon/ptable.php>.

V. Resonant Photoemission of Rare Earth Doped GaN Thin Films

The contents of this chapter were accepted for publication in reference [1]. The $4d \rightarrow 4f$ Fano resonances for various rare earth doped GaN thin films (RE = Gd, Er, Yb) were investigated using synchrotron photoemission spectroscopy. The resonant photoemission Fano profiles show that the major Gd and Er rare earth $4f$ weight is at about 5–6 eV below the valence band maximum, similar to the $4f$ weights in the valence band of many other rare earth doped semiconductors. For Yb, there is very little resonant enhancement of the valence band of Yb doped GaN, consistent with a largely $4f^{14}$ occupancy.

5.1 Introduction

During the past decade, rare earth doped semiconductors have generated considerable attention for their application in new optoelectronic devices [2–5]. III-nitride semiconductors, such as AlN, GaN, and InN offer tunable bandgaps and favorable thermal, chemical, and electronic properties, which facilitate various device applications [6–10] from the ultraviolet through the visible spectrum to the infrared range. Moreover, thin film electroluminescent phosphors with red, blue, and green emissions [8–16] imply the promise of full color (white) light capability. Rare earth doping GaN might have a number of advantages: there is the promise that Eu or Er doping will improve the light output. Luminescence due to the Er intra- $4f$ -shell transition from the $^4I_{13/2}$ excited state to the $^4I_{15/2}$ ground state is known to be particularly intense and, above all, efficient. Due to their highly localized $4f$ electrons [17,18], the direct $f-f$ interactions between the neighboring rare earth atoms are very weak and nonexistent in a weakly doped semiconductor host. In addition, rare earth doping is seen to increase the gold electrode Schottky barrier heights significantly [19] thereby

decreasing leakage currents in particle type detector devices.

While numerous resonant photoemission studies of rare earth metals have been reported, the resonant processes resulting from photon interaction with III-nitride semiconductors are significantly less understood. Plucinski *et al.* [20] reported a resonant photoemission process at the Ga $3p$ absorption threshold in GaN and compared the results to those reported for GaP and GaAs [21,22]. Lastly, Maruyama *et al.* [23] reported on Eu doped GaN using X-ray photoelectron spectroscopy (XPS) and resonant photoemission spectroscopy (RPES) and concluded, via $4d \rightarrow 4f$ resonant photoemission measurements, that the transition from trivalent to divalent Eu ions occurred near the surface of GaN. The key value of resonant photoemission, however, is to probe what valence bands of the semiconductors have strong $4f$ and/or rare earth weight [24–26]. Of course, such photon energy dependent studies must be disentangled from bulk band structure effects, so there is considerable value in studying the resonant photoemission process of a semiconductor with several different rare earths; each is likely to dope the semiconductor in a similar fashion, but the resonant enhancement of the valence band will occur at different photon energies.

Although likely to locally strain the lattice, the $4f$ rare earths will tend to adopt substitutional sites for Ga [2,3,27] in GaN while significantly altering magnetic [28–35] and optical properties [8–15], and it is therefore of considerable interest to know whether even low concentrations of a rare earth in the GaN host can alter the surface electronic structure. This is likely, as although rare earths are isoelectronic with Ga^{3+} , they may be associated with other defects [36,37]. With these considerations in mind, we have engaged in investigations of the surface electronic structure and interface properties of the $\text{RE}_x\text{Ga}_{1-x}\text{N}$ ($\text{RE} = \text{Gd}, \text{Er}, \text{Yb}$) semiconductors.

5.2 Experimental

The $\text{RE}_x\text{Ga}_{1-x}\text{N}$ thin films (50–300 nm) were fabricated on Si(111) (RE = Gd, Yb) and sapphire Al_2O_3 (RE = Er) substrates by RF plasma (EPI 620) assisted molecular beam epitaxy (MBE). The growth parameters for the deposition of RE-doped (*in situ*) GaN thin films were base pressure of $\sim 10^{-11}$ Torr, nitrogen flux of 0.75–1.0 SCCM (Gd, Yb) and 2.0 SCCM (Er), RF power of 500 W, substrate temperature of 850–900 °C, Ga cell temperature of 850 °C, and RE cell temperatures of 1050–1100 °C (Gd), 1000–1100 °C (Er), and 500–850 °C (Yb). The thickness of the films was measured with a surface profilometer and atomic force microscopy.

The orientation, crystal structure, and phase purity of the films were established by Cu K_α ($\lambda = 1.5406$ Å) radiation X-ray diffraction using a Siemens D5000 X-ray diffractometer. The X-ray diffraction (XRD) patterns of Gd, Er, and Yb doped GaN films show *c*-axis orientation and a high degree of crystallinity. The presence of any secondary phases or spurious peaks has not been observed, as described elsewhere [19]. Slight shifts in diffraction peak positions towards lower Bragg angles has been observed with Er doped GaN grown on $\text{Al}_2\text{O}_3(0001)$ substrates and $\text{RE}_x\text{Ga}_{1-x}\text{N}$ thin films (50–300 nm) fabricated on Si(111) (RE = Gd, Yb), which is indicative of some lattice expansion, as is expected [27]. The *c*-axis length of GaN:Yb was found to be 5.172 Å [27], which is very close to the widely reported and accepted *c*-axis length (5.166 Å) of undoped GaN.

The elemental compositions of the rare earth doped GaN thin films grown under different conditions were characterized by energy dispersive spectroscopy (EDS) and a VG Microtech XPS attached to the MBE growth system (VG Microtech). The measured concentrations were found to be at 1–2%, as confirmed from the Ga $2p_{3/2}$, Er $4d$, Gd $4d$, Yb $4d$, and N $1s$ core level XPS intensities using an Al K_α (1486.8 eV) X-ray source. The typical values for Er concentrations were found to be $\sim 5\%$,

higher than the EDS- and XPS-derived Gd and Yb concentrations. In the rare earth doped GaN samples, surface segregation cannot be excluded and may well be likely, at least in the selvedge region of the surface.

The photoemission experiments were conducted on the 3m TGM beamline [38] at the Center for Advanced Microstructures and Devices at Louisiana State University [39–41]. The beamline is equipped with a photoemission endstation with a 50 mm hemispherical electron energy analyzer, with a resolution of about 70 meV, as described elsewhere [38, 42]. Photoemission spectra were taken with a 45° incidence angle and the photoelectrons collected along the sample normal. All spectra presented are normalized to the photon flux, and the secondary electron background has been subtracted. The position of the Fermi level was established using a clean Ta foil as reference. All binding energies reported here are with respect to this common Fermi level in terms of $E - E_F$, so that occupied state binding energies are negative. Energy distribution curves (EDCs) were obtained by fixing the photon energy $h\nu$ and sweeping electron kinetic energy E_{kin} , thus measuring binding energies. Constant initial state spectra were obtained by simultaneously sweeping $h\nu$ and E_{kin} , so as to hold binding energy fixed.

Atomically clean GaN:RE surfaces were obtained by several preparatory cycles of Ar^+ ion sputtering and annealing, as described elsewhere [19, 27]. This will create a number of point defects, but photoemission is generally insensitive to such defects. The photoemission spectra from the clean sample surfaces indicated that the surfaces were free of contaminants.

5.3 Results and Discussion

5.3.1 The $4f$ Contributions to the Valence Band of Doped GaN.

The effects of band hybridization and dopant induced strain between the various rare earth dopants and the GaN surfaces are not identical. The valence band spectra for Gd and Er doped GaN are very similar as seen in Figures 28 and 29, while for Yb doped GaN (Figure 30), the valence band is significantly broader extending from -2 eV to nearly -14 eV. The spectra do change with with photon energy and significant enhancements of some of the valence band features are seen at some photon energies. Figures 28, 29, and 30 (RE = Gd, Er, Yb) show the valence band photoemission spectra at various photon energies in the vicinity of the respective rare earth dopant $4d$ absorption thresholds. For the rare earth dopants studied, resonance results from a signal overlap between direct emission of photoelectrons from the $4f$ state

$$4d^{10}4f^N + h\nu \longrightarrow 4d^{10}4f^{N-1} + e^-, \quad (76)$$

and Auger-like electrons emitted in a super Coster-Kronig process [43]

$$4d^{10}4f^N + h\nu \longrightarrow [4d^94f^{N+1}]^* \longrightarrow 4d^{10}4f^{N-1} + e^-, \quad (77)$$

where $[]^*$ denotes an excited state. The final states for both the direct and recombination processes are identical.

For Gd doped GaN (GaN:Gd), Figure 28 shows that the intensity of the spectral features near 8–9 eV below the Fermi level first increase slightly at ~ 144 eV, followed by a rapid and considerable enhancement, with maximum intensity at a photon energy of ~ 148 eV. Figure 29 shows a similar, albeit not identical, response for GaN:Er. As with the GaN:Gd thin film, the spectral feature at an approximate binding energy of -9 eV in GaN:Er resonates in the range of the Er $4d$ absorption

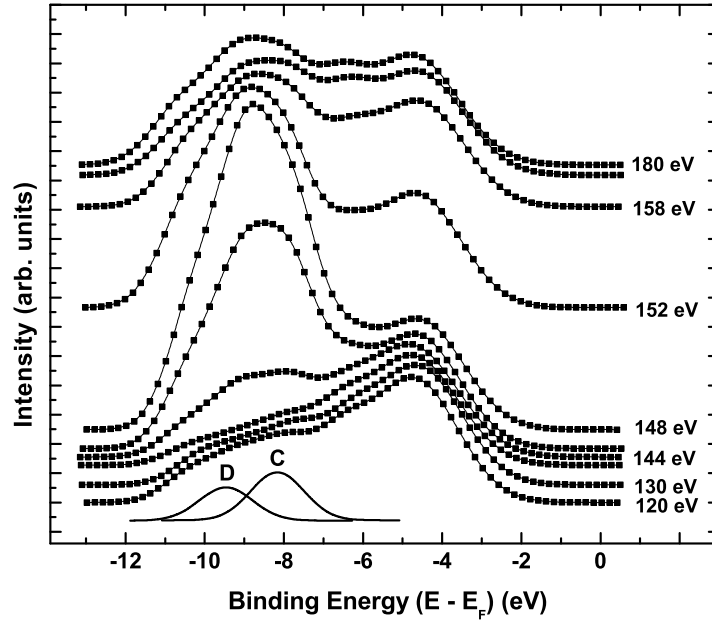


Figure 28. Energy distribution curves of GaN:Gd for various incident photon energies, as shown for each spectrum. The strong surface and bulk $4f$ Gd components of the GaN:Gd valence band are illustrated. Resonating components C (-8.1 eV) and D (-9.6 eV), used for the constant initial state curves in Figure 31, are shown at the bottom.

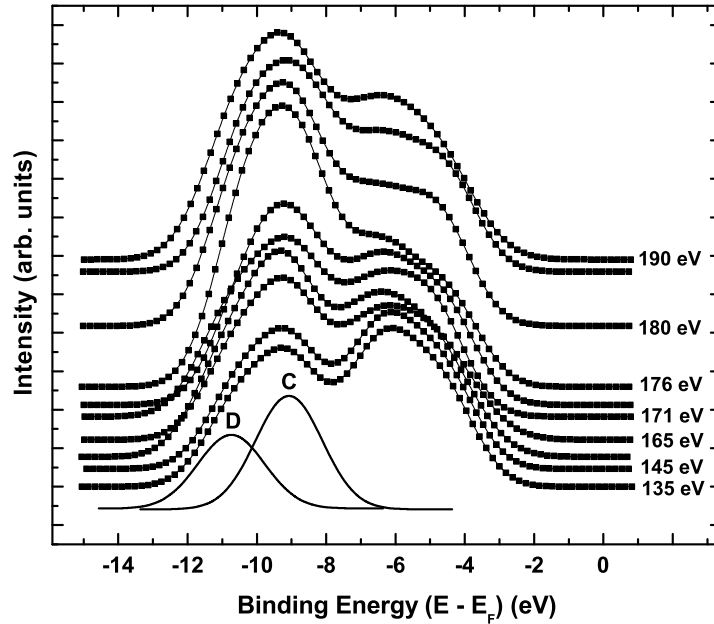


Figure 29. Energy distribution curves of GaN:Er for various incident photon energies, as shown for each spectrum. The resonating components C (-8.9 eV) and D (-10.7 eV), used for the constant initial state curve in Figure 32, are shown at the bottom.

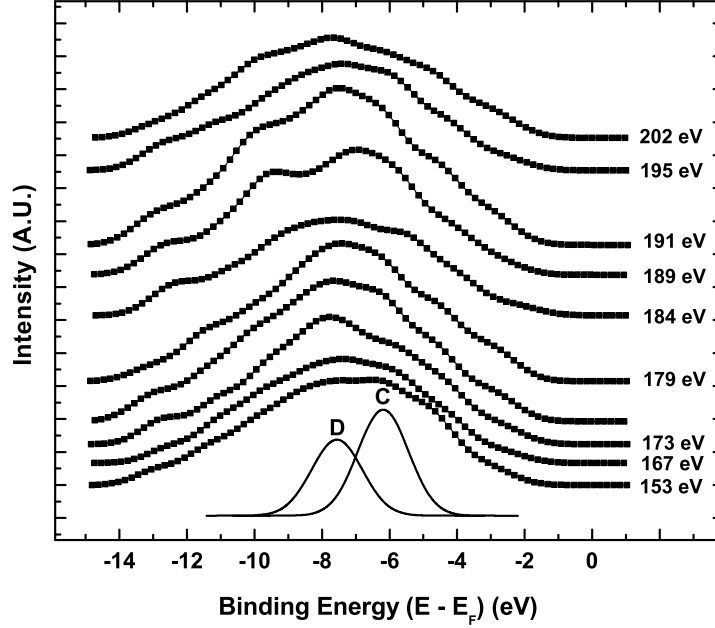


Figure 30. Energy distribution curves of GaN:Yb for various incident photon energies, as shown for each spectrum. Resonating components C (-6.2 eV) and D (-7.6 eV), used for the constant initial state curve in Figure 33, are shown at the bottom.

threshold. However, Figure 29 shows that the features near the bottom of the valence band increase in intensity considerably first at ~ 165 eV and then again at ~ 176 eV for GaN:Er. Lastly, Figure 30 (GaN:Yb) reveals that the intensity of spectral features at binding energy ~ 7 eV increase slightly at ~ 178 eV, and slightly again at ~ 190 eV.

The intensity of the valence band features for which the direct and super Coster-Kronig processes overlap is described as a function of photon energy $h\nu$ by the Fano lineshape [43, 44] as

$$N(h\nu) \cong \frac{(\epsilon + q)^2}{\epsilon^2 + 1}, \quad \epsilon = \frac{h\nu - h\nu_j}{\Gamma}, \quad (78)$$

where $h\nu_j$ is the photon energy equal to the core level absorption threshold binding energy, q is a fitting parameter for the core level, and $\Gamma = \Delta(h\nu_j)/2$ where $\Delta(h\nu_j)$ is the width (FWHM) of the core level.

5.3.2 The $4f$ Contributions to the Valence Band of GaN:Gd.

The GaN:Gd valence band components, at binding energies in the region of -8 to -10 eV, represent the valence band features that strongly resonate at photon energies in the vicinity of 147 eV, as plotted in Figure 31. These intensity resonances (Figure 31) are very similar to those observed for Gd_2O_3 [45] and Gd doped HfO_2 [24, 45]. Not only are the resonant photon energies similar, but the features at the bottom of the valence band contain a strong feature at about -8 eV binding energy and a weaker shoulder in the vicinity of -10 eV binding energy. This suggests a surface and bulk component for the Gd in GaN, in spite of the low Gd concentrations. Figure 31 displays the constant initial state spectra and the calculated Fano profiles for GaN:Gd. The weighted oscillator strength, gf , relates directly to the electric dipole transition probability and, hence, line intensity. Theoretical interpretations of resonant photoemission in lanthanide metals at the $4d$ absorption threshold via gf calculations have been reported [46] and have been shown to agree well with experimental results [47]. The resonance peak, at roughly 147.5 eV for the GaN:Gd Fano line profile in Figure 31, illustrates reasonable agreement with the Gd gf calculations of Sugar [46], which indicated a strong absorption peak centered at 149.0 eV. This agreement supports further the assertion that the GaN:Gd spectral features at the bottom of the valence band, in the region of -8 to -10 eV in Figure 28, are of strong Gd $4f$ weight or represent bands that strongly hybridize with the rare earth. This is expected based on the Gd occupied $4f$ level placement in GdN [28, 48].

5.3.3 The $4f$ Contributions to the Valence Band of GaN:Er.

Similarly, for GaN:Er, the valence band features, again at the bottom of the valence band at binding energies of roughly -8.9 and -10.7 eV, strongly resonate at photon energies of 166 and 173 eV, as plotted in Figure 32. Two Fano line shapes

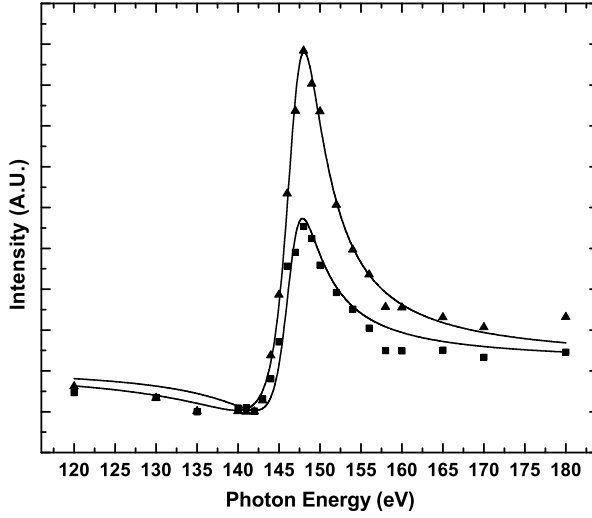


Figure 31. Constant initial state curves and Fano fit (solid lines) for feature C (squares) at -8.1 eV and feature D (triangles) at -9.6 eV in GaN:Gd. The fitting component, q , for feature C was calculated as 1.91; for feature D it was 2.79.

were used to fit the experimental results for GaN:Er, shown in Figure 32. The GaN:Er Fano line profile in Figure 32 also shows reasonable agreement with the gf calculations [46]. Specifically, Sugar reported the separation between oscillator strength maxima at 167.2 eV and 174.8 eV to be 7.6 eV for Er [46]. Our experimentally observed separation is roughly 7 to 7.5 eV between absorption peaks at 166 eV and 173 eV for GaN:Er. The ratio of the Er computational peak maxima reported by Sugar is $\sim 1 : 2.6$ [46], somewhat larger than the ratio of the peak maxima at roughly 166 eV and 173 eV of about $1.55^2/2.14^2$ or $\sim 1 : 1.9$ for GaN:Er, as plotted in Figure 32. Although inspection of equation (78) predicts that when $h\nu \rightarrow h\nu_j$, $N(h\nu) \rightarrow q^2$, nonetheless, the resonant photoemission of the GaN:Er thin film at absorption thresholds of roughly 166 eV and 173 eV represents reasonable agreement with the Er 4d shallow core (167.2 eV, 174.8 eV) binding energies. Thus, unlike the case of the Gd doped GaN, there are spin-orbit interactions that separate out the $4d_{3/2}$ and $4d_{5/2}$ in GaN:Er.

While there are indications that the occupied density of states would have the spectral weight density at the bottom of the valence band, although complexed with

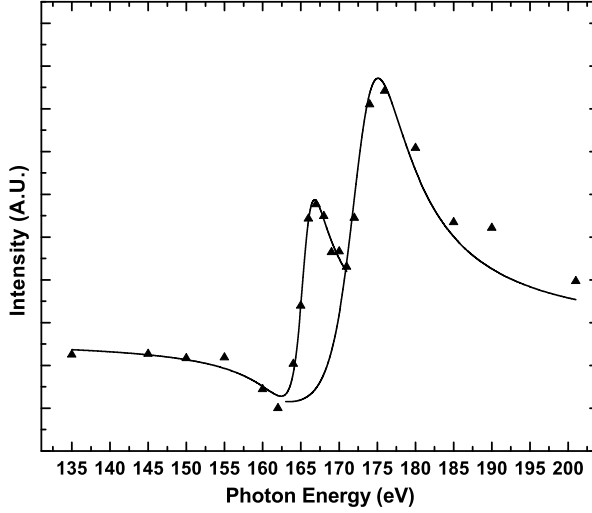


Figure 32. Constant initial state curve (triangles) and Fano fit (solid lines) for the valence band feature in the vicinity of -9 eV binding energy, for GaN:Er. The fitting component, q , in the region of the Er $4d_{5/2}$ absorption threshold (166 eV) was calculated as 1.55; in the region of the Er $4d_{3/2}$ absorption threshold (173 eV) it was 2.14.

a vacancy defect, contributions at the top of the valence band might also be expected [37]. In fact, the f removal energies calculated for Er placed in GaN are seen to be very similar to those noted for Gd in GaN [49]. This differs from the relative position of the Gd and Er $4f$ levels in GaAs [49]. Judging by ErAs [50], we would expect $4f$ contributions at both the bottom and the top of the valence band of GaN. The region of 4–6 eV binding energy should be dominated by the $4f_{7/2}$ (mainly the 5I_8 and 5I_7 multiplet components [50–52]), while the bottom of the valence band should be dominated by the $4f_{5/2}$ (mainly the $^3M_{10}$ and 3L_9 multiplet components [50–52], although there are many others). Strong hybridization of the $4f$ states, possibly modified by intra-atomic $f-d$ and $f-s$ hybridizations [50, 53–55] can lead to a much more delocalized core exciton, and a decrease in the resonant photoemission intensities [56].

5.3.4 The $4f$ Contributions to the Valence Band of GaN:Yb.

To test the possibility of intra-atomic $f - d$ and $f - s$ hybridizations [50, 53–55], or extra-atomic $4f$ hybridization with the Ga and N, we also looked at the resonant enhancement of the valence band of GaN:Yb, as seen in Figures 30 and 33. Although much weaker than the resonant enhancements observed for GaN:Gd (Figure 31) and GaN:Er (Figure 32), there is a resonant enhancement of the valence band, particularly in the region of approximately -6 to -7 eV binding energy, as plotted in Figure 33. Although Yb metal should have an electronic configuration

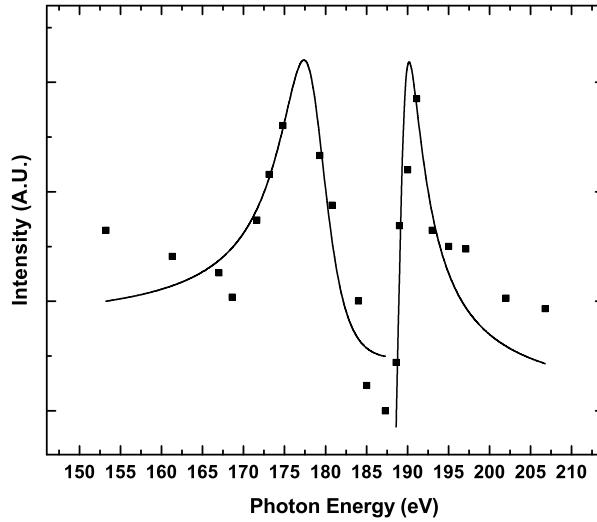


Figure 33. Constant initial state curve (squares) and Fano fit (solid lines) for the valence band features in the vicinity of -7 eV binding energy, for GaN:Yb. The fitting component, q , in the region of the Yb $4d_{5/2}$ absorption threshold (179 eV) was calculated as 0.33; in the region of the Yb $4d_{3/2}$ absorption threshold (189 eV) it was 1.15.

of $4d^{10}4f^{14}$, such that an excited $4d$ electron has no unfilled $4f$ state to occupy, partial $4f$ occupancy is still possible. Previous experimental results [57, 58] using the oxidation-induced valence change of Yb ($4f^{14} \rightarrow 4f^{13}$) determined that the data for Yb_2O_3 were well described by Fano’s theory of interaction between discrete and continuum states. There are similar expectations for Er doped GaSb [59]. Despite

the relative weakness of the observed Fano line shapes for GaN:Yb, we note that the enhancements in spectral features in the valence band do exhibit photoemission resonances at photon energies in the vicinity of 179 eV and 189 eV. These absorption thresholds agree reasonably well with the Yb $4d_{5/2}$ (182.0 eV) and the Yb $4d_{3/2}$ (190.8 eV) shallow core level binding energies. Because it is not just the valence band maximum that exhibits the weak photoemission resonance in the expected location of the Yb $4f$ multiplets [51], the depletion of the $4f$ occupancy appears related to strong hybridization with the GaN lattice.

5.4 Summary and Conclusions

Resonant photoemission for GaN thin films doped with various rare earths (RE = Gd, Er, Yb) was investigated using synchrotron based photon energy dependent photoemission spectroscopy. The calculated Fano profiles predict the experimentally observed $4d \rightarrow 4f$ super Coster-Kronig processes and strong rare earth $4f$ weights were observed about 5–6 eV below the valence band maximum for Gd and Er doped GaN. For Yb, the photoemission resonance is much weaker, indicating that there is only a very little depletion of the $4f^{14}$ occupancy, but strong hybridization with GaN is implicated. There is also evidence from the selectivity of the resonant photoemission enhancement of the valence band that there is also strong $4f$ hybridization with the GaN valence bands, particularly within the Er $4f_{5/2}$ envelope. The results here on the placement of the occupied Gd, Er and Yb $4f$ levels, deep within the valence band, suggests that the intra-atomic f – f transitions may be more ‘blue’ than predicted by many theoretical models. The resonant photoemission results strongly support the predicted hybridization with the host lattice [55], and the expected f – s hybridization [50, 53–55].

References

- [1] S. R. McHale, J. W. McClory, J. C. Petrosky, J. Wu, R. Palai, Y. B. Losovyj, and P. A. Dowben, “Resonant photoemission of rare earth doped GaN thin films,” *European Physical Journal Applied Physics*, 2011, in press.
- [2] T. Koubaa, M. Dammak, M. Kammoun, W. M. Jadwisieniczak, and H. J. Lozykowski, “Crystal Field and Zeeman Parameters of Substitutional Yb³⁺ Ion in GaN,” *Journal of Alloys and Compounds*, vol. 496, no. 1-2, pp. 56–60, 2010.
- [3] T. Koubaa, M. Dammak, M. Kammoun, W. M. Jadwisieniczak, H. J. Lozykowski, and A. Anders, “Spectra and energy levels of Yb³⁺ in AlN,” *Journal of Applied Physics*, vol. 106, no. 1, p. 013106, 2009.
- [4] W. M. Jadwisieniczak and H. J. Lozykowski, “Optical Properties of Yb Ions in GaN Epilayer,” *Optical Materials*, vol. 23, no. 1-2, pp. 175–181, 2003.
- [5] A. J. Kenyon, “Recent Developments in Rare-Earth Doped Materials for Optoelectronics,” *Progress in Quantum Electronics*, vol. 26, no. 4-5, pp. 225–284, 2002.
- [6] J. H. Park and A. J. Steckl, “Effect of Process Conditions on Gain and Loss in GaN: Eu Cavities on Different Substrates,” *Physica Status Solidi(a)*, vol. 205, no. 1, pp. 26–29, 2008.
- [7] A. Nishikawa, T. Kawasaki, N. Furukawa, Y. Terai, and Y. Fujiwara, “Room-temperature red emission from a *p*-type/europium-doped/*n*-type gallium nitride light-emitting diode under current injection,” *Applied Physics Express*, vol. 2, no. 7, p. 1004, 2009.
- [8] A. J. Steckl, J. Heikenfeld, D. S. Lee, and M. Garter, “Multiple color capability from rare earth-doped gallium nitride,” *Materials Science and Engineering B*, vol. 81, no. 1-3, pp. 97–101, 2001.
- [9] J. H. Tao, N. Perea-Lopez, J. McKittrick, J. B. Talbot, K. Klinedinst, M. Raukas, J. Laski, K. C. Mishra, and G. Hirata, “Synthesis of rare-earth activated AlN and GaN powders via a three-step conversion process,” *Physica Status Solidi (c)*, vol. 5, no. 6, pp. 1889–1891, 2008.
- [10] J. Shi, M. V. S. Chandrashekhar, J. Reiherzer, W. Schaff, J. Lu, F. Disalvo, and M. Spencer, “High Intensity Red Emission from Eu Doped GaN Powders,” *Physica Status Solidi (c)*, vol. 5, no. 6, pp. 1495–1498, 2008.
- [11] W. Jadwisieniczak, K. Wisniewski, M. Spencer, T. Thomas, and D. Ingram, “Optical properties, luminescence quenching mechanism and radiation hardness of Eu-doped GaN red powder phosphor,” *Radiation Measurements*, vol. 45, no. 3-6, pp. 500–502, 2010.

- [12] H. Okada, Y. Nakanishi, A. Wakahara, A. Yoshida, and T. Ohshima, “380 keV proton irradiation effects on photoluminescence of Eu-doped GaN,” *Nuclear Instruments and Methods in Physics Research Section B: Beam Interactions with Materials and Atoms*, vol. 266, no. 5, pp. 853–856, 2008.
- [13] Y. Nakanishi, A. Wakahara, H. Okada, A. Yoshida, T. Ohshima, and H. Itoh, “Effect of 3 MeV electron irradiation on the photoluminescence properties of Eu-doped GaN,” *Applied Physics Letters*, vol. 81, no. 11, pp. 1943–1945, 2002.
- [14] T. Thomas, X. Guo, M. V. S. Chandrashekhar, C. B. Poitras, W. Shaff, M. Dreibelbis, J. Reiherzer, K. Li, F. J. DiSalvo, and M. Lipson, “Purification and mechanical nanosizing of Eu-doped GaN,” *Journal of Crystal Growth*, vol. 311, no. 19, pp. 4402–4407, 2009.
- [15] A. J. Steckl, J. H. Park, and J. M. Zavada, “Prospects for rare earth doped GaN lasers on Si,” *Materials Today*, vol. 10, no. 7-8, pp. 20–27, 2007.
- [16] Y. Q. Wang and A. J. Steckl, “Three-color integration on rare-earth-doped GaN electroluminescent thin films,” *Applied Physics Letters*, vol. 82, p. 502, 2003.
- [17] G. H. Dieke and H. M. Crosswhite, “The spectra of the doubly and triply ionized rare earths,” *Applied Optics*, vol. 2, no. 7, pp. 675–686, 1963.
- [18] S. H fner, K. A. Gschneidner, and L. R. Eyring, *Handbook on the Physics and Chemistry of Rare Earths*. North Holland, 1978.
- [19] S. R. McHale, J. W. McClory, J. C. Petrosky, J. Wu, A. Rivera, R. Palai, Y. B. Losovyj, and P. A. Dowben, “Schottky barrier formation at the Au to rare earth doped GaN thin film interface,” *European Physical Journal Applied Physics*, 2011, in press.
- [20] L. Plucinski, T. Learmonth, L. Colakerol, S. Bernardis, Y. Zhang, P. A. Glans, K. E. Smith, A. A. Zakharov, R. Nyholm, and I. Grzegory, “Resonant shake-up satellites in photoemission at the Ga 3*p* photothreshold in GaN,” *Solid State Communications*, vol. 136, no. 4, pp. 191–195, 2005.
- [21] T. C. Chiang and D. E. Eastman, “Resonant photoemission shake-up and Auger processes at the 3*p* photothreshold in Ga and GaP,” *Physical Review B*, vol. 21, no. 12, p. 5749, 1980.
- [22] S. Suzuki, T. Kiyokura, F. Maeda, K. G. Nath, Y. Watanabe, T. Saitoh, and A. Kakizaki, “Observation of Ga 3*d* two-hole states from GaAs surfaces,” *Journal of Electron Spectroscopy and Related Phenomena*, vol. 114, pp. 421–425, 2001.
- [23] T. Maruyama, S. Morishima, H. Bang, K. Akimoto, and Y. Nanishi, “Valence transition of Eu ions in GaN near the surface,” *Journal of Crystal Growth*, vol. 237, pp. 1167–1171, 2002.

- [24] I. Ketsman, Y. B. Losovyj, A. Sokolov, J. Tang, Z. Wang, K. D. Belashchenko, and P. A. Dowben, “The n -type Gd-doped HfO_2 to silicon heterojunction diode,” *Applied Physics A: Materials Science & Processing*, vol. 89, no. 2, pp. 489–492, 2007.
- [25] R. F. Sabirianov, W. N. Mei, J. Lu, Y. Gao, X. C. Zeng, R. D. Bolskar, P. Jeppson, N. Wu, A. N. Caruso, and P. A. Dowben, “Correlation effects and electronic structure of $\text{Gd}@ \text{C}_{60}$,” *Journal of Physics: Condensed Matter*, vol. 19, p. 082201, 2007.
- [26] I. Ketsman, Y. B. Losovyj, A. Sokolov, J. Tang, Z. Wang, M. L. Natta, J. I. Brand, and P. A. Dowben, “Gd-doping of HfO_2 ,” *Applied Surface Science*, vol. 254, no. 14, pp. 4308–4312, 2008.
- [27] S. R. McHale, J. W. McClory, J. C. Petrosky, J. Wu, R. Palai, P. A. Dowben, and I. Ketsman, “The effective surface debye temperature of Yb:GaN ,” *Materials Letters*, vol. 65, p. 1476, 2011.
- [28] C. G. Duan, R. F. Sabirianov, W. N. Mei, P. A. Dowben, S. S. Jaswal, and E. Y. Tsymbal, “Electronic, magnetic and transport properties of rare-earth mononictides,” *Journal of Physics: Condensed Matter*, vol. 19, p. 315220, 2007.
- [29] H. Asahi, Y. K. Zhou, M. Hashimoto, M. S. Kim, X. J. Li, S. Emura, and S. Hasegawa, “GaN-based magnetic semiconductors for nanospintronics,” *Journal of Physics: Condensed Matter*, vol. 16, p. S5555, 2004.
- [30] M. Takahashi, Y. K. Zhou, T. Nakamura, S. Emura, S. Hasegawa, and H. Asahi, “Magnetic Properties of GaGdN Studied by SX-MCD and XAFS,” *Journal of Superconductivity and Novel Magnetism*, vol. 23, no. 1, pp. 107–109, 2010.
- [31] S. Dhar, O. Brandt, M. Ramsteiner, V. F. Sapega, and K. H. Ploog, “Colossal magnetic moment of Gd in GaN ,” *Physical Review Letters*, vol. 94, no. 3, p. 37205, 2005.
- [32] L. Pérez, G. S. Lau, S. Dhar, O. Brandt, and K. H. Ploog, “Magnetic phases and anisotropy in Gd-doped GaN ,” *Physical Review B*, vol. 74, no. 19, p. 195207, 2006.
- [33] J. Hejtmánek, K. Knížek, M. Maryško, Z. Jiráček, D. Sedmidubský, Z. Sofer, V. Peřina, H. Hardtdegen, and C. Buchal, “On the magnetic properties of Gd implanted GaN ,” *Journal of Applied Physics*, vol. 103, no. 7, pp. 07D107–07D107–3, 2008.
- [34] S. Y. Han, J. Hite, G. T. Thaler, R. M. Frazier, C. R. Abernathy, S. J. Pearton, H. K. Choi, W. O. Lee, Y. D. Park, and J. M. Zavada, “Effect of Gd implantation on the structural and magnetic properties of GaN and AlN ,” *Applied Physics Letters*, vol. 88, p. 042102, 2006.

- [35] N. Teraguchi, A. Suzuki, Y. Nanishi, Y. K. Zhou, M. Hashimoto, and H. Asahi, “Room-temperature observation of ferromagnetism in diluted magnetic semiconductor GaGdN grown by RF-molecular beam epitaxy,” *Solid State Communications*, vol. 122, no. 12, pp. 651–653, 2002.
- [36] J. S. Filhol, R. Jones, M. J. Shaw, and P. R. Briddon, “Structure and electrical activity of rare-earth dopants in GaN,” *Applied Physics Letters*, vol. 84, p. 2841, 2004.
- [37] B. Hourahine, S. Sanna, B. Aradi, C. Köhler, and T. Frauenheim, “A theoretical study of erbium in GaN,” *Physica B: Condensed Matter*, vol. 376, pp. 512–515, 2006.
- [38] Y. Losovyj, I. Ketsman, E. Morikawa, Z. Wang, J. Tang, and P. Dowben, “Optimization of the 3m TGM beamline, at CAMD, for constant initial state spectroscopy,” *Nuclear Inst. and Methods in Physics Research, A*, vol. 582, no. 1, pp. 264–266, 2007.
- [39] J. Hormes, J. D. Scott, and V. P. Suller, “Facility update: the center for advanced microstructures and devices: a status report,” *Synchrotron Radiation News*, vol. 19, no. 1, pp. 27–30, 2006.
- [40] A. Roy, E. Morikawa, H. Bellamy, C. Kumar, J. Goetttert, V. Suller, K. Morris, D. Ederer, and J. Scott, “Status of the Center for Advanced Microstructures and Devices (CAMD)–2007,” *Nuclear Instruments and Methods in Physics Research Section A: Accelerators, Spectrometers, Detectors and Associated Equipment*, vol. 582, no. 1, pp. 22–25, 2007.
- [41] E. Morikawa, J. D. Scott, J. Goetttert, G. Aigeldinger, C. S. S. R. Kumar, B. C. Craft, P. T. Sprunger, R. C. Tittsworth, and F. J. Hormes, “Status of the Center for Advanced Microstructures and Devices (CAMD) – 2001,” *Review of Scientific Instruments*, vol. 73, p. 1680, 2002.
- [42] P. A. Dowben, D. LaGraffe, and M. Onellion, “Final-state symmetry effects in photoemission of thin Gd overlayers,” *Journal of Physics: Condensed Matter*, vol. 1, p. 6571, 1989.
- [43] G. Wendin, *Breakdown of the One-Electron Pictures in Photoelectron Spectra, Structure and Bonding Vol. 45*. Springer-Verlag, Berlin, 1981.
- [44] U. Fano, “Effects of configuration interaction on intensities and phase shifts,” *Physical Review*, vol. 124, no. 6, pp. 1866–1878, 1961.
- [45] Y. B. Losovyj, D. Wooten, J. C. Santana, J. M. An, K. D. Belashchenko, N. Lozova, J. Petrosky, A. Sokolov, J. Tang, and W. Wang, “Comparison of *n*-type Gd₂O₃ and Gd-doped HfO₂,” *Journal of Physics: Condensed Matter*, vol. 21, p. 045602, 2009.

- [46] J. Sugar, “Potential-barrier effects in photoabsorption. ii. interpretation of photoabsorption resonances in lanthanide metals at the $4d$ -electron threshold,” *Physical Review B*, vol. 5, no. 5, p. 1785, 1972.
- [47] T. M. Zimkina, V. A. Fomichev, S. A. Gribovskii, and I. I. Zhukova, “Anomalies in the character of the X-ray absorption of rare-earth elements of the lanthanide group.” *Soviet Physics - Solid State (English translation)*, vol. 9, p. 1447, 1967.
- [48] F. Leuenberger, A. Parge, W. Felsch, K. Fauth, and M. Hessler, “GdN thin films: Bulk and local electronic and magnetic properties,” *Physical Review B*, vol. 72, no. 1, p. 014427, 2005.
- [49] A. Svane, N. E. Christensen, L. Petit, Z. Szotek, and W. M. Temmerman, “Electronic structure of rare-earth impurities in GaAs and GaN,” *Physical Review B*, vol. 74, no. 16, p. 165204, 2006.
- [50] T. Komesu, H. K. Jeong, J. Choi, C. N. Borca, P. A. Dowben, A. G. Petukhov, B. D. Schultz, and C. J. Palmstrm, “Electronic structure of ErAs (100),” *Physical Review B*, vol. 67, no. 3, p. 035104, 2003.
- [51] J. K. Lang, Y. Baer, and P. A. Cox, “Study of the $4f$ and valence band density of states in rare-earth metals,” *Journal of Physics F: Metal Physics*, vol. 11, p. 121, 1981.
- [52] L. Stauffer, C. Pirri, P. Wetzel, A. Mharchi, P. Paki, D. Bolmont, G. Gewinner, and C. Minot, “Bulk electronic structure of AlB_2 -type erbium disilicide with and without Si vacancies,” *Physical Review B*, vol. 46, no. 20, p. 13201, 1992.
- [53] I. N. Yakovkin, T. Komesu, and P. A. Dowben, “Band structure of strained Gd (0001) films,” *Physical Review B*, vol. 66, no. 3, p. 035406, 2002.
- [54] P. Strange, A. Svane, W. M. Temmerman, Z. Szotek, and H. Winter, “Understanding the valency of rare earths from first-principles theory,” *Nature*, vol. 399, p. 756, 1999.
- [55] G. M. Dalpian and S. H. Wei, “Electron-induced stabilization of ferromagnetism in $\text{Ga}_{1-x}\text{Gd}_x\text{N}$,” *Physical Review B*, vol. 72, no. 11, p. 115201, 2005.
- [56] P. A. Dowben, “The metallicity of thin films and overlayers,” *Surface Science Reports*, vol. 40, no. 6-8, pp. 151–247, 2000.
- [57] L. I. Johansson, J. W. Allen, I. Lindau, M. H. Hecht, and S. B. M. Hagström, “Photoemission from Yb: Valence-change-induced Fano resonance,” *Physical Review B*, vol. 21, no. 4, pp. 1408–1411, 1980.
- [58] J. Schmidt-May, F. Gerken, R. Nyholm, and L. C. Davis, “Resonant photoemission of oxidized Yb: Experiment and theory,” *Physical Review B*, vol. 30, no. 10, pp. 5560–5565, 1984.

- [59] Y. M. Sun and M. C. Wu, “X-ray photoelectron spectroscopy and optoelectrical properties of low-concentration erbium-doped GaSb layers grown from Sb-rich solutions by liquid-phase epitaxy,” *Journal of Applied Physics*, vol. 78, no. 11, pp. 6691–6695, 1995.

VI. Schottky Barrier Formation at the Au to Rare Earth Doped GaN Thin Film Interface

The contents of this chapter were accepted for publication in reference [1]. The Schottky barriers formed at the interface between gold and various rare earth doped GaN thin films (RE = Yb, Er, Gd) were investigated *in situ* using synchrotron photoemission spectroscopy. The resultant Schottky barrier heights were measured as 1.68 ± 0.1 eV (Yb:GaN), 1.64 ± 0.1 eV (Er:GaN), and 1.33 ± 0.1 eV (Gd:GaN). We find compelling evidence that thin layers of gold do not wet and uniformly cover the GaN surface, even with rare earth doping of the GaN. Furthermore, the trend of the Schottky barrier heights follows the trend of the rare earth metal work function.

6.1 Introduction

During the past decade, rare earth doped semiconductors have generated considerable attention for their application in new optoelectronic devices [2–5]. The favorable thermal, chemical, and electronic properties of wide band gap, III-nitride semiconductors suggest device feasibility using lanthanide-doped AlN and GaN. Moreover, the tunable bandgaps of these III-nitride alloys offer device applications across the visible spectrum through the ultra-violet range, to include optically stimulated lasing [6] and p-n junction light emitting diodes in the red [7] using lanthanide-doped AlN and GaN, as well as in the blue. Lastly, the production of thin film electroluminescent phosphors with red, blue, and green emissions [8–10] offers the promise of full color (white) light capability.

The large band gap (~ 3.45 eV) of GaN minimizes the effects of thermal or visible (or longer wave length) light charge carrier generation, while alloying with a rare earth nitride should decrease the band gap. As a general rule, the rare-earth monopnictides have band gaps of 0.7 to 1.0 eV [11], and in many cases are

suspected to be semimetals, but if alloyed with AlN or GaN are of considerable interest as semiconductors. As a device material, $\text{RE}_x\text{Ga}_{1-x}\text{N}$ is unlikely in principle to result in significant changes to the barrier heights and the band gap of GaN, if the RE doping level is low. Although, if metal induced gap states play a significant role [12,13], even a small amount of rare earth could have a significant effect on the Schottky barrier heights. It is important to recognize that rare earth dopant induced strain, and a bulk concentration of even a dilute amount of rare earth atoms, can significantly alter the surface chemistry and the surface enthalpy leading to a means for adjusting Schottky barrier heights that can accompany an engineering of the GaN optical properties.

Although gold is generally considered unreactive [14] complications abound. Surface alloying can occur [15] and a large range of experimentally measured Schottky barrier heights has been reported (0.76 - 1.40 eV) at the Au to *n*-type GaN interface [14–30], using photoemission spectroscopy (PES), current-voltage (I-V) and capacitance voltage (C-V) characteristics, and internal photoemission [31]. However, the generally accepted value is about 1.08 eV [32]. Kurtin, McGill, and Mead [33] suggested that the Schottky barrier height on GaN should depend directly on the work function or electronegativity difference between the metal electrode and GaN. Foresi and Moustakas [34] observed this direct correlation experimentally, while Guo *et al.* [35] and Mori *et al.* [36] observed only a weak dependence of the Schottky barrier height on the metal work function for *n*-type GaN and *p*-type GaN, respectively. The 1998 review of metal-GaN contact technology by Liu and Lau [20] reported that, for a variety of contact metals with both low and high work functions, Schottky barrier heights at the metal-GaN interface varied with metal work function, within the experimental scatter. Subsequent work by Rickert *et al.* [24] supported a modified Schottky-Mott model at the metal-GaN interface for Ni, Pd, and Al, yet more ‘complex’ behavior when Au, Ti, and Pt were used as the contact

metals. Additional experiments by Barinov *et al.* [22, 23] reported Schottky barrier heights at the Au-GaN interface that exceeded both work function difference (Schottky-Mott) and electronegativity difference (metal induced gap states) models. Thus, a point worth re-emphasizing is that regardless of the particular metal-GaN interface studied, experimentally measured barrier heights can vary considerably.

Using photoemission to measure the surface barrier height is advantageous because the technique is both extremely surface sensitive, and one can avoid some of the complications associated with other experimental techniques. For example, when using traditional I-V and C-V measurements, defects at the metal-semiconductor interface can often lead to overestimates of the surface barrier height [24, 37].

Although likely to locally strain the lattice, the $4f$ rare earths will tend to adopt substitutional sites for Ga [2, 3, 38] in GaN while significantly altering magnetic and optical properties [11], and it is of considerable interest to know whether even low concentrations of a rare earth in the GaN host will routinely lead to high or low barrier height values at the Au-RE:GaN interface. With this in mind, we have engaged in investigations of the interface properties of $\text{RE}_x\text{Ga}_{1-x}\text{N}$ (RE = Yb, Er, Gd) semiconductors with Au metal overlayer deposition under UHV conditions. Our studies of the Au to $\text{RE}_x\text{Ga}_{1-x}\text{N}$ semiconductor interface properties were performed much in the manner of other studies of the Au to GaN interface [19, 21–24].

6.2 Experimental

The experimental details were identical to those discussed for resonant photoemission in Section 5.2, with the following exceptions:

- (1) The valence band and Ga $3d$ shallow core spectra were taken with a photon energy $h\nu = 90$ eV. Au $4f$ spectra were taken with a photon energy of $h\nu = 140$ eV.
- (2) Binding energies are shown as absolute values $|E - E_f|$, instead of negative values.

- (3) The Au deposition was made by thermal evaporation on the clean RE:GaN surfaces at room temperature. To prevent contamination, the background vacuum pressure was generally kept at $< 10^{-9}$ torr. The evaporation rate and average coverage, reported here in \AA , was monitored by means of a quartz crystal thickness monitor located in the evaporation chamber. A low deposition rate of $\sim 0.2 \text{ \AA}/\text{min}$ was used in a best effort to enhance uniform film growth and ensure accurate determinations of the average Au film thickness.

6.3 Results and Discussion

6.3.1 The Rare Earth Doped GaN Surfaces.

The relative position of the valence band, and changes due to the band bending, were determined by monitoring the Ga $3d$ core level shift as a function of Au coverage. The measured Ga $3d$ peaks in Figures 34(a), 35(a), and 35(b) are very similar to the photoemission spectra reported previously [21–23, 39, 40]. The Ga $3d$ shallow core level peaks are broad, with maxima at 17.7 eV (Yb:GaN), 17.1 eV (Er:GaN), and 17.4 eV (Gd:GaN) below the valence band maximum (VBM), in acceptable agreement with the expected value of 17.7 eV [22, 23, 39] for wurtzite GaN. The energy difference between the valence band maximum and a core level, $E_{\text{VBM-C}}$, is considered a bulk property of the material and is, therefore, independent of metal coverage [22–24]. The valence band maximum, determined by extrapolation of the high kinetic energy edge of the clean spectrum, as is the common practice [21–24, 40, 41], is at 2.7 eV below E_F for the Yb:GaN surface. Assuming that the low RE-doping levels (1–2 %) of our samples leaves the 3.45 eV band gap for GaN relatively unchanged, and given that E_F is approximately 50 meV below the conduction band minimum in the bulk of n -type GaN [21], determines the upward band bending at the clean Yb:GaN surface (bare surface barrier height) as 0.70 eV. A consequence of the high photon flux environment ($\geq 10^{11} \text{ photons-}\mu\text{m}^{-2}\text{-s}^{-1}$) required by photoelectron spectroscopy are surface photovoltage effects, which have been known to cause band flattening [22]. By varying the sample temperature in a separate experiment, we demonstrated that

surface photovoltage was negligible for our samples. Thus, we consider our measured bare surface barrier height to be in good agreement with values reported previously for UHV prepared *n*-type wurtzite GaN surfaces (0.50–1.40 eV) [21, 22, 40–42].

The ionization energy

$$\text{IE} = E_{\text{VAC}} - E_{\text{VBM}} = (E_F - E_{\text{VBM}}) + \phi_a, \quad (79)$$

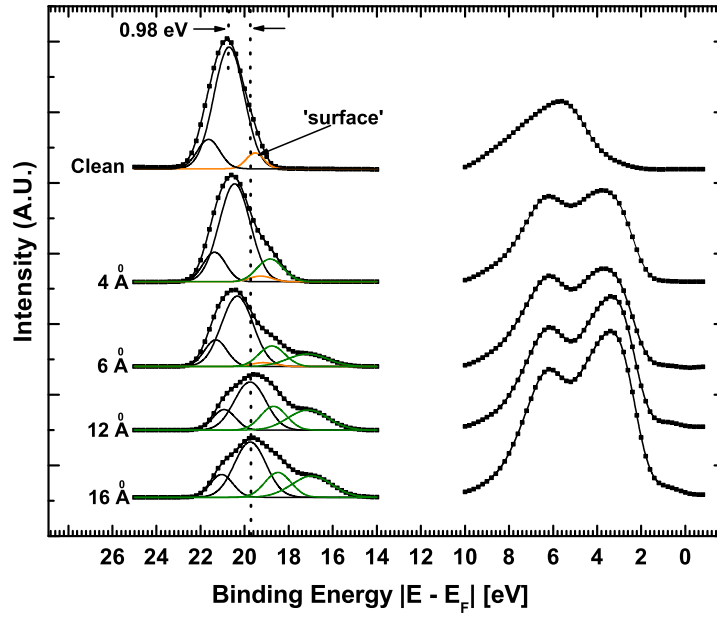
given the analyzer work function ϕ_a of 4.4 eV, is 7.1 ± 0.1 eV for Yb:GaN, which is in reasonable agreement with prior values (6.7–6.9 eV) [21, 42] for GaN. The electron affinity

$$\chi = \phi_a - [E_g - (E_F - E_{\text{VBM}})], \quad (80)$$

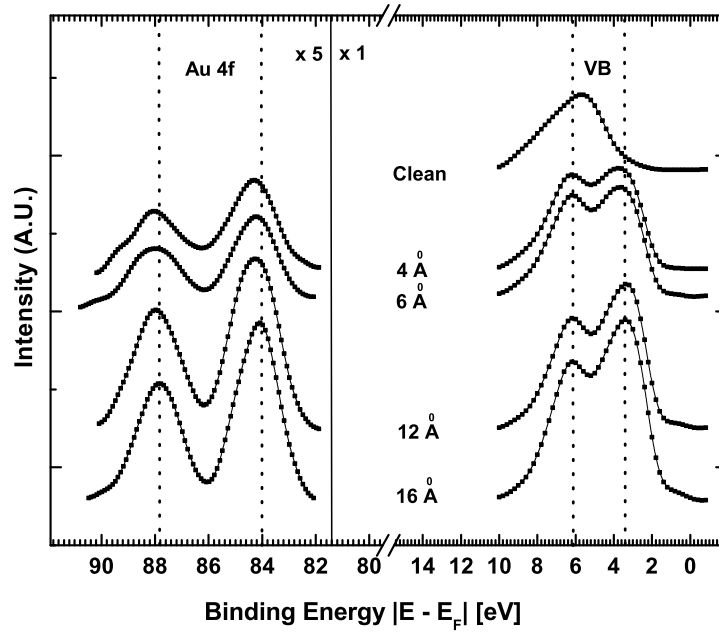
is thus 3.7 ± 0.1 eV for Yb:GaN, which is in reasonable agreement (2.2–4.1 eV) [21, 40, 42, 43] with previously reported results for GaN. Table 1 summarizes the experimentally measured surface electronic properties of each RE:GaN sample and indicates reasonable agreement, given the low RE-doping levels, between our samples and previously published GaN values.

Table 3. Measured properties of clean RE:GaN surfaces. Experimental uncertainties are listed only when explicitly stated within the indicated references.

Material	$E_F - E_{\text{VBM}}$	BSBH	IE	χ
Yb:GaN	2.70 ± 0.1	0.70 ± 0.1	7.10 ± 0.1	3.70 ± 0.1
Er:GaN	2.80 ± 0.1	0.60 ± 0.1	7.20 ± 0.1	3.80 ± 0.1
Gd:GaN	2.65 ± 0.1	0.75 ± 0.1	7.05 ± 0.1	3.65 ± 0.1
GaN	2.60 [21]	0.75 ± 0.1 [21]	6.90 ± 0.1 [21]	3.50 ± 0.1 [21]
GaN	2.80 ± 0.1 [22]	0.50 ± 0.1 [22]		
GaN	1.90 ± 0.2 [40]	1.40 ± 0.2 [40]		2.70 ± 0.2 [40]
GaN	2.70 [41]	0.70 [41]		2.20 - 4.10 [43]
GaN	2.50 [42]	0.90 [42]	6.70 [42]	3.30 [42]

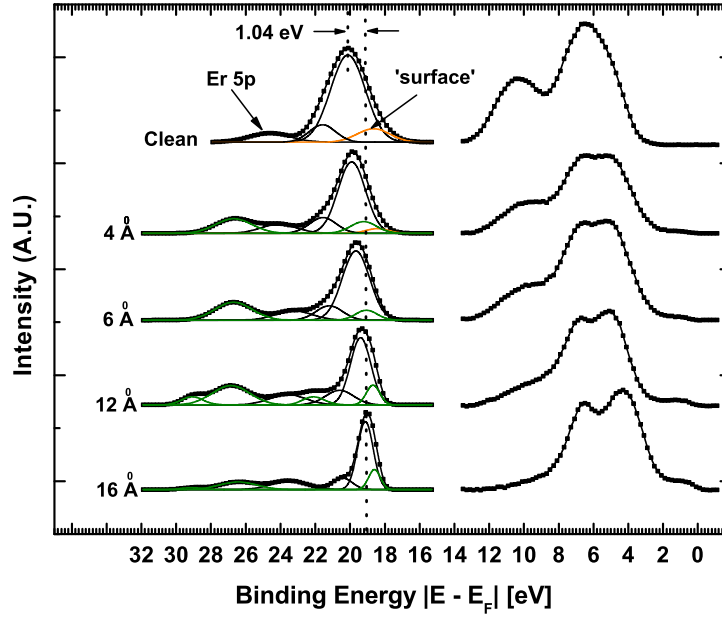


(a) Yb:GaN

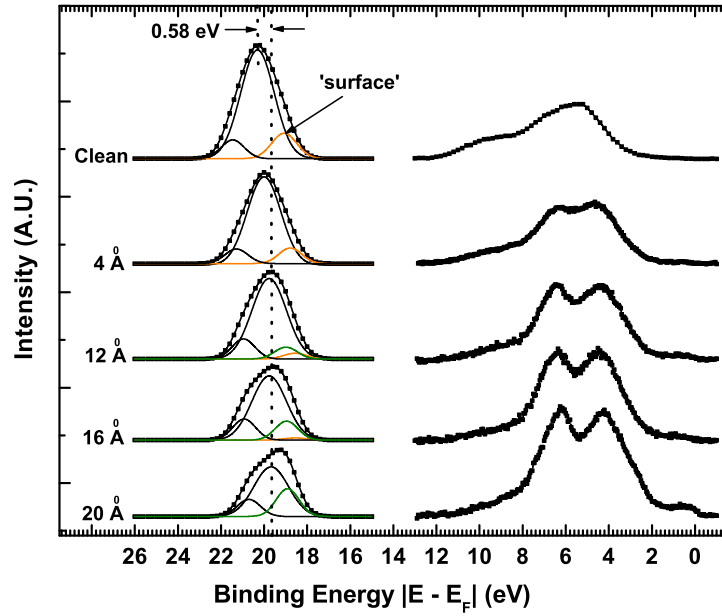


(b) Au 4f

Figure 34. Deconvolution of Ga 3d core-level spectra (a) and evolution of valence band and Au 4f bands (b) with increasing Au coverage on Yb:GaN thin film. The components attributed to bulk GaN features are shown with solid black lines. The lower binding energy 'surface' component, shown as the orange line, is removed with increasing Au coverage and is replaced with Au-GaN and Au-RE alloy features (solid green lines).



(a) Er:GaN



(b) Gd:GaN

Figure 35. Deconvolution of Ga 3d core-level spectra and valence band evolution with increasing Au coverage on Er:GaN (a) and Gd:GaN (b) thin films. The components attributed to bulk GaN features are shown with solid black lines. The lower binding energy 'surface' component, shown as the orange solid line, is removed with increasing Au coverage and is replaced with Au-GaN and Au-RE alloy features (solid green lines).

6.3.2 The Growth of Gold Overlayers on RE:GaN Surfaces.

Figure 34 shows the evolution of the valence band and Ga 3*d* spectra for a Yb:GaN sample with increasing Au coverage. The progressively metallic nature of the overlayer film is reflected in the valence band features by a density of states above the valence band maximum at a Au overlayer film thickness of about 6 Å, leading to emission at or near the Fermi level (E_F) at about 12 Å of Au. The valence band of the gold overlayer, as seen in the photoemission data, is dominated by the Au 5*d* weighted bands [44], as is expected, with the Au 5*d* levels at binding energies of 3.5 and 6.1 eV, in reasonable agreement with published values for bulk Au [45] and gold deposited on III-V semiconductors [46].

We also measured the Au 4*f*_{7/2} and Au 4*f*_{5/2} levels as a function of Au coverage, as shown in Figure 34(b). The Au 4*f* features appear, at a coverage of 4 Å, at binding energies that are approximately 0.3 eV greater than the Au 4*f*_{7/2} and Au 4*f*_{5/2} levels of 84.0 eV and 87.7 eV in metallic Au [47]. With increasing Au coverage up to 16 Å, these peaks sharpen, increase in intensity, and shift toward the lower binding energies of bulk Au. This decrease in the Au 4*f*_{7/2} and Au 4*f*_{5/2} levels, with increasing gold coverage, is one of many indicators that initial gold adsorption is not uniformly wetting the surface and that island growth is likely.

From photoemission work with Au alloys, it is known that Au surface distribution may be probed by following the details of the 5*d* bands [48]. When Au atoms are well dispersed, as in a dilute Au alloy, 5*d* bands are shifted toward higher binding energies, as compared to the bulk values. The splitting of the 5*d* valence band features should increase from the value for atomic Au (1.5 eV) to the bulk value (2.5 eV) with increased deposition. In our studies, we find the Au 5*d* band splitting is about 2.6 eV for Yb:GaN (Figure 34(b)) and Gd:GaN (Figure 35(b)), almost independent of Au overlayer coverage, indicative of rapid metallic Au island formation.

Attenuation of the Ga $3d$ core level in Figures 34(a), 35(a), and 35(b) (RE = Yb, Er, Gd) also indicates that the growth mode of the Au on the respective RE:GaN surfaces is not uniform (Frank-van der Merwe or layer-by-layer growth) but rather the Au overlayer growth follows Volmer-Weber (island growth) or Stranski-Krastanov growth. While the growth mode strongly depends on the particular metal-semiconductor pair and also on the experimental conditions such as substrate temperature and evaporation rate [49], the evidence for Volmer-Weber (island growth) or Stranski-Krastanov growth in describing Au on the respective RE:GaN surfaces is robust. If the gold were of uniform thickness, the Ga $3d$ core level photoemission signal would be absent at thicker Au overlayer coverages due to the limited mean free path of approximately 5 Å in Au [50, 51], estimated from the kinetic energy of a Ga $3d$ photoelectron using a photon energy of 90 eV.

Since the Ga $3d$ core levels are visible in the spectra up to 16 Å Au coverage, thin spots must exist in the Au overlayer film. The intensity of the Ga $3d$ core level before I_0 and after I_s deposition leads to a change in photoemission intensity, described by Volmer-Weber growth [24, 49, 52, 53], as

$$\frac{I_s}{I_0} = (1 - \theta) + \theta e^{-t/\lambda}, \quad (81)$$

where t is the film thickness, λ is the mean free path of the electrons, and θ represents the fractional surface coverage reached prior to island growth in three dimensions. Figure 36 shows the photoemission intensity ratios of the Ga $3d$ core level for each of the RE:GaN thin films studied. As expected, the fit parameter differs for each Au to RE:GaN interface studied, which reflects the strong growth mode dependence upon the particular metal-semiconductor pair.

The data indicate that Au is not growing in a layer-by-layer manner but rather by Volmer-Weber (island growth) or Stranski-Krastanov growth. Although layer-by-

layer growth for Au on GaN has been reported [19], there has also been evidence of island formation [19, 24, 54]. Here, we find compelling evidence that thin layers of gold do not wet and cover the GaN surface, even with rare earth doping of the GaN. We would expect that a dilute surface coverage of rare earth atoms would nucleate more uniform Au overlayer films, but this does not appear to be the case.

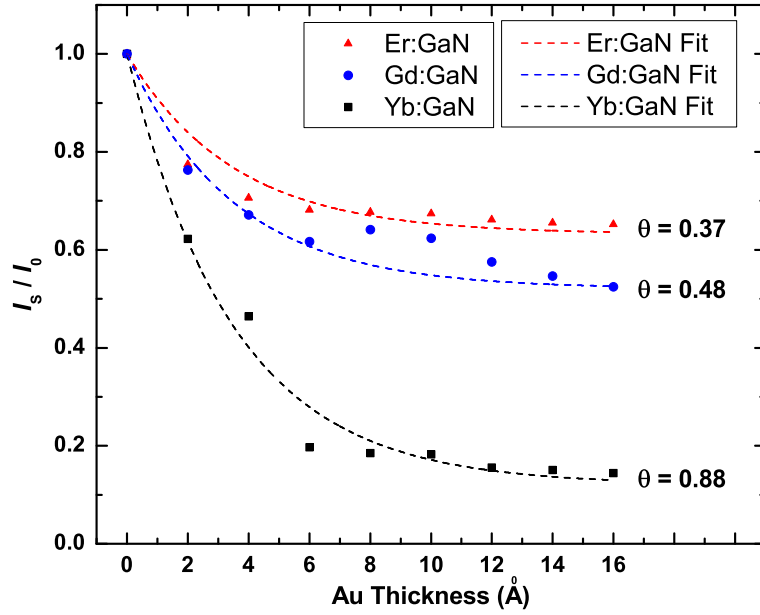


Figure 36. The intensity ratio of the Ga 3d core level before I_0 and after I_s Au deposition as a function of film thickness for the deposition of Au on RE:GaN, as indicated. The expected ratio as a function of thickness (dashed lines) is plotted using the Volmer-Weber growth mode.

6.3.3 Schottky Barrier Formation at RE:GaN Surfaces.

When metal is evaporated on the sample surface, the edge of the semiconductor valence band maximum is obscured by the signal originating from the metal overlayer. However, owing to the fact that $E_{\text{VBM-C}}$ is constant, the Ga 3d core shift is roughly equivalent to the valence band shift at the semiconductor surface, from which the

Schottky barrier height $\Phi_{B,n}$ is calculated as

$$\Phi_{B,n} = E_g - (E_F - E_{\text{VBM}}). \quad (82)$$

To describe the surface Fermi level movement and Schottky barrier formation during Au deposition, Ga 3*d* core levels were deconvoluted into surface and bulk components with Gaussian form. There exists some variation concerning the number of fitting components for the Ga 3*d* lineshape. Some authors choose a single, dominant bulk subpeak and one surface subpeak [39,55] to represent the surface to bulk core level shift that affects the Ga 3*d* lineshape, whereas other researchers deconvolute the lineshape using two bulk subpeaks and one surface subpeak [22,23,56]. We calculated Schottky barrier heights using both methods, and their differences proved negligible (< 0.05 eV) for all Au to RE:GaN interfaces. However, we present only our results using the latter method to deconvolute the Ga 3*d* peak, as this is deemed more reliable. We selected this method owing to the compelling arguments of Barinov *et al.* [22,23] and Lambrecht *et al.* [56] who demonstrated that the dominant and high binding energy components of the peak are intrinsic features of the Ga 3*d* semi-core levels of GaN and are related to hybridization effects [20], while the lower binding energy component behaves as a ‘surface’ component. In Figures 34(a), 35(a), and 35(b), black subpeaks represent bulk components and orange subpeaks represent the surface components. As Au coverage increases, Au forms a surface alloy with GaN and the RE metals on the sample surface, and their features are represented as green subpeaks. These features supplant the surface component of the Ga 3*d* core levels.

The effect of Au deposition on the various RE doped GaN surfaces is not identical, as inferred from the Ga 3*d* shallow-core spectra. The clean Yb:GaN Ga 3*d* shallow-core spectra in Figure 34(a) and the clean Gd:GaN Ga 3*d* shallow-core spectra in Figure 35(b) required three fitting components to represent the Ga 3*d* lineshape.

During Au deposition on Yb:GaN, the single surface component was replaced with two alloy/Au interface components that were separated, at lower binding energies, from the dominant bulk peak by 1.3 eV and 2.9 eV. During Au deposition on Gd:GaN, the single surface component was replaced with a single alloy/Au interface component that was separated, at a lower binding energy, from the dominant bulk peak by 0.7 eV.

The clean Er:GaN spectrum in Figure 35(a) required four subpeaks to deconvolute the Ga 3*d* lineshape. We associate the fourth subpeak, at binding energy 24.8 eV, with the Er 5*p* core level, which has a binding energy of 28.0 eV in bulk Er. During Au deposition, the single surface component was replaced with one alloy component that was separated, at a lower binding energy, from the dominant Ga 3*d* bulk peak by 0.6 eV. Additional fitting components were needed to deconvolute the spectral features that evolved around the Er 5*p* subpeak. One alloy component located, at a higher binding energy, from the Er 5*p* subpeak by 3.0 eV is present in all spectra from 4 Å – 16 Å Au coverage. The intensity of this Ga 3*d* shallow-core spectra component increases from 4 Å – 12 Å Au coverage, but is attenuated at 16 Å Au coverage, possibly the result of surface alloy formation. When this Ga 3*d* shallow-core spectra component is at maximum intensity at 12 Å Au coverage, precise spectral deconvolution requires two additional alloy components. These two additional alloy/Au interface components are separated from the Er 5*p* subpeak by lower and higher binding energies of 1.7 eV and 5.3 eV, respectively.

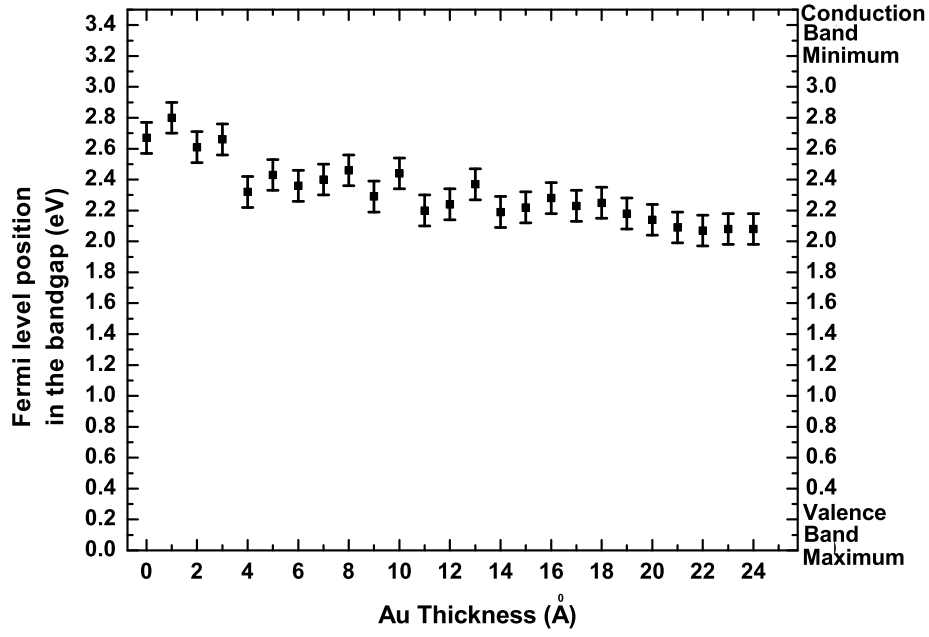
Fermi level movement, surface valence band bending, and Schottky barrier formation were determined by monitoring the binding energy shift of the dominant, bulk Ga 3*d* component during Au deposition. Figures 34(a), 35(a), and 35(b) show these measured shifts to be 0.98 eV (Yb:GaN), 1.04 eV (Er:GaN), and 0.58 eV (Gd:GaN). Figure 37 shows the surface Fermi level movement 37(a) and resultant Schottky barrier formation 37(b) for Gd:GaN, which was calculated as 1.33 ± 0.1 eV via (82).

The same methods and calculations described above yielded Schottky barrier heights of 1.64 ± 0.1 eV and 1.68 ± 0.1 eV for Er:GaN and Yb:GaN, respectively. These are generally far larger than the values found for undoped GaN, as measured via PES, I-V, C-V, and internal photoemission (IPE), and summarized in Table 4.

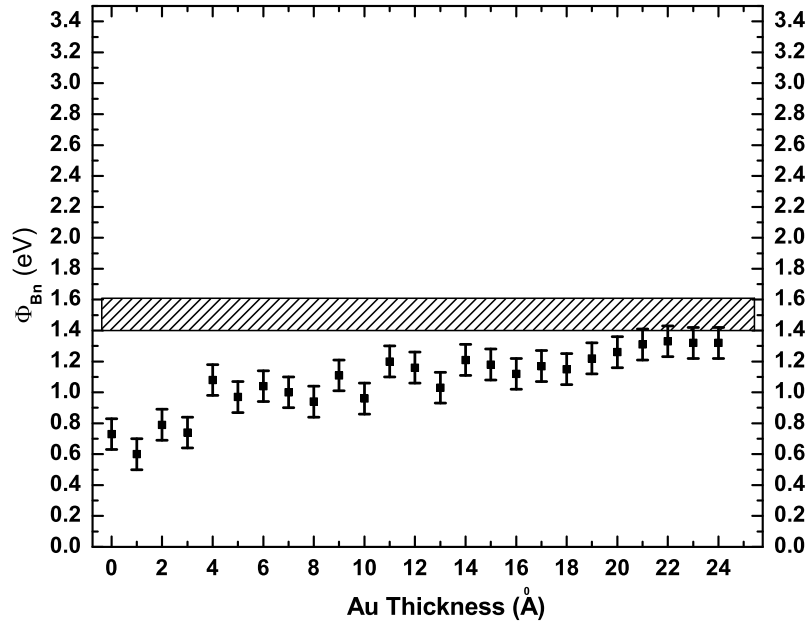
Table 4. Comparison between experimentally measured and theoretically predicted (Schottky-Mott) barrier heights. Experimental uncertainties are listed only when explicitly stated within the indicated references.

Material	χ_s [eV] via Table 3	$\Phi_{B, n}$ [eV] (theory)	$\Phi_{B, n}$ [eV] (measured)	Measurement technique
Yb:GaN	3.70 ± 0.1	1.45 ± 0.1	1.68 ± 0.1	PES
Er:GaN	3.80 ± 0.1	1.35 ± 0.1	1.64 ± 0.1	PES
Gd:GaN	3.65 ± 0.1	1.50 ± 0.1	1.33 ± 0.1	PES
GaN	4.10 [43]	1.05	1.15 [19]	PES
GaN			1.20 ± 0.1 [21]	PES
GaN			1.40 ± 0.1 [22, 23]	PES
GaN			0.90 ± 0.1 [24]	PES
GaN			1.18 ± 0.07 [26]	I-V
GaN			0.94 [16]	I-V
GaN			1.19 [17]	I-V
GaN			1.15 [17]	C-V
GaN			0.87 [18]	I-V
GaN			0.98 [18]	C-V
GaN			1.10 [14]	I-V
GaN			1.22 [15]	I-V
GaN			0.81 [29]	I-V
GaN			0.76 [29]	IPE
GaN			1.0 [30]	IPE
GaN			1.11 [25]	IPE
GaN			0.95 ± 0.04 [27]	IPE
GaN			0.97 ± 0.05 [28]	IPE

Because of the possible interfacial reactions between the Au and RE:GaN surfaces, the magnitude of the shift in the Ga $3d$ shallow-core spectra due to Au charge donation cannot be determined quantitatively. While we associate the Ga $3d$ core shift with band bending, we must be careful to state that other causes cannot be completely excluded by the data presented here.



(a) Gd:Ga_N Fermi level movement



(b) Gd:Ga_N Schottky barrier formation

Figure 37. Fermi level movement (a) and Schottky Barrier formation (b) at the surface of Gd:Ga_N based upon the binding energy of the bulk component of a Ga 3*d* core level taken at a photon energy of 90 eV. The filled region in (b) indicates the range of ideal barrier height values, as predicted by the Schottky-Mott model using our measured χ values from Table 3.

The Schottky-Mott relationship characterizes contacts for n -type semiconductors such that when the work function of the metal contact is greater than the work function of the semiconductor, i.e. $\phi_m > \phi_s$, the contact is rectifying. The work function ϕ_s for GaN has been calculated from photoemission experiments as 4.2 ± 0.2 eV [41], whereas the work function ϕ_m of Au is 5.15 eV [57]. The Schottky-Mott theory also predicts that for n -type semiconductors, with $\phi_m > \phi_s$, the surface barrier height is calculated as the difference between the contact metal work function and the electron affinity of the semiconductor sample χ_s as

$$\Phi_{B,n} = \phi_m - \chi_s. \quad (83)$$

The most commonly used [18,34,39] electron affinity for undoped GaN was reported as 4.1 eV [43], which yields a theoretical barrier height of 1.05 eV between Au and GaN. Our measured values for χ_s , determined from the clean RE:GaN bare surface barrier heights (Table 3), suggest higher theoretical Schottky barrier heights (1.45 ± 0.1 eV (Yb:GaN), 1.35 ± 0.1 eV (Er:GaN), 1.50 ± 0.1 eV (Gd:GaN) than for undoped GaN (Table 2). Thus, both measured and theoretically predicted Au-RE:GaN Schottky barrier heights are larger than those for the Au-GaN interface. Given a constant electrode metal work function, either a decreased semiconductor electron affinity (83) or decreased semiconductor work function (increased contact potential) due to rare earth doping of GaN would produce higher barrier heights than for undoped GaN, but more likely, both occur.

We note that, in general, the trend of the Schottky barrier heights follows the trend of the rare earth metal work function, so that although the RE ion occupies a Ga site in the GaN [2,3,38], perturbation of the rare earth on the surface electronic structure of GaN is possible. The work function of Yb is 2.60 eV [58], that of Er is 2.97 eV [59], while Gd is 3.10 eV [57], all of which are lower than that of GaN (4.2 eV).

Regardless of the interplay between electron affinity and GaN surface work function, the resultant Au-RE:GaN Schottky barrier heights, as measured and noted above, are 1.68 ± 0.1 eV (Yb:GaN), 1.64 ± 0.1 eV (Er:GaN), and 1.33 ± 0.1 eV (Gd:GaN), and are significantly higher than observed for undoped GaN. Thus, band bending at the Au-RE:GaN (RE = Yb, Er, Gd) interface is larger than the normal (Au-GaN). This implies that barrier heights might be engineered to optimize depletion widths and charge collection volumes for sensor device applications.

6.4 Conclusions

Photoemission studies using synchrotron radiation showed that the Schottky barrier heights between Au and RE:GaN thin film samples were measured to be 1.68 ± 0.1 eV (Yb:GaN), 1.64 ± 0.1 eV (Er:GaN), and 1.33 ± 0.1 eV (Gd:GaN). This trend of the Schottky barrier heights follows the trend of the rare earth metal work function. The Au overlayer does not wet and cover the GaN surface, even with rare earth doping of the GaN. But in spite of the imperfections of the Au-RE:GaN interface, the resulting Schottky barrier interfaces might lead to significant improvement in device performance in sensor applications.

References

- [1] S. R. McHale, J. W. McClory, J. C. Petrosky, J. Wu, A. Rivera, R. Palai, Y. B. Losovyj, and P. A. Dowben, "Schottky barrier formation at the Au to rare earth doped GaN thin film interface," *European Physical Journal Applied Physics*, 2011, in press.
- [2] T. Koubaa, M. Dammak, M. Kammoun, W. M. Jadwisienczak, and H. J. Lozykowski, "Crystal field and Zeeman parameters of substitutional Yb³⁺ ion in GaN," *Journal of Alloys and Compounds*, vol. 496, no. 1-2, pp. 56–60, 2010.

- [3] T. Koubaa, M. Dammak, M. Kammoun, W. M. Jadwisieniczak, H. J. Lozykowski, and A. Anders, "Spectra and energy levels of Yb³⁺ in AlN," *Journal of Applied Physics*, vol. 106, no. 1, p. 013106, 2009.
- [4] W. M. Jadwisieniczak and H. J. Lozykowski, "Optical properties of Yb ions in GaN epilayer," *Optical Materials*, vol. 23, no. 1-2, pp. 175–181, 2003.
- [5] A. J. Kenyon, "Recent developments in rare-earth doped materials for optoelectronics," *Progress in Quantum Electronics*, vol. 26, no. 4-5, pp. 225–284, 2002.
- [6] J. H. Park and A. J. Steckl, "Effect of process conditions on gain and loss in GaN: Eu cavities on different substrates," *Physica Status Solidi(a)*, vol. 205, no. 1, pp. 26–29, 2008.
- [7] A. Nishikawa, T. Kawasaki, N. Furukawa, Y. Terai, and Y. Fujiwara, "Room-temperature red emission from a p-type/europium-doped/n-type gallium nitride light-emitting diode under current injection," *Applied Physics Express*, vol. 2, no. 7, p. 1004, 2009.
- [8] A. J. Steckl, J. Heikenfeld, D. S. Lee, and M. Garter, "Multiple color capability from rare earth-doped gallium nitride," *Materials Science and Engineering B*, vol. 81, no. 1-3, pp. 97–101, 2001.
- [9] J. H. Tao, N. Perea-Lopez, J. McKittrick, J. B. Talbot, K. Klinedinst, M. Raukas, J. Laski, K. C. Mishra, and G. Hirata, "Synthesis of rare-earth activated AlN and GaN powders via a three-step conversion process," *Physica Status Solidi C*, vol. 5, no. 6, pp. 1889–1891, 2008.
- [10] J. Shi, M. V. S. Chandrashekhar, J. Reiherzer, W. Schaff, J. Lu, F. Disalvo, and M. Spencer, "High intensity red emission from Eu doped GaN powders," *physica status solidi (c)*, vol. 5, no. 6, pp. 1495–1498, 2008.
- [11] C. G. Duan, R. F. Sabirianov, W. N. Mei, P. A. Dowben, S. S. Jaswal, and E. Y. Tsymbal, "Electronic, magnetic and transport properties of rare-earth monopnictides," *Journal of Physics: Condensed Matter*, vol. 19, p. 315220, 2007.
- [12] V. Heine, "Theory of surface states," *Phys.Rev*, vol. 138, no. 6A, pp. 1689–1696, 1965.
- [13] T. U. Kampen and W. Mnch, "Barrier heights of GaN Schottky contacts," *Applied Surface Science*, vol. 117, pp. 388–393, 1997.
- [14] Y. Kribes, I. Harrison, B. Tuck, T. S. Cheng, and C. T. Foxon, "Investigation of Au Schottky contacts on GaN grown by molecular beam epitaxy," *Semiconductor Science and Technology*, vol. 12, p. 913, 1997.

- [15] L. He, X. J. Wang, and R. Zhang, “Enhanced electrical performance of Au/*n*-GaN Schottky diodes by novel processing,” *Journal of Vacuum Science & Technology A: Vacuum, Surfaces, and Films*, vol. 17, p. 1217, 1999.
- [16] P. Hacke, T. Detchprohm, K. Hiramatsu, and N. Sawaki, “Schottky barrier on *n*-type GaN grown by hydride vapor phase epitaxy,” *Applied Physics Letters*, vol. 63, no. 19, pp. 2676–2678, 1993.
- [17] S. C. Binari, H. B. Dietrich, G. Kelner, L. B. Rowland, K. Doverspike, and D. K. Gaskill, “Electrical characterisation of Ti Schottky barriers on *n*-type GaN,” *Electronics Letters*, vol. 30, no. 11, pp. 909–911, 1994.
- [18] A. C. Schmitz, A. T. Ping, M. A. Khan, Q. Chen, J. W. Yang, and I. Adesida, “Schottky barrier properties of various metals on *n*-type GaN,” *Semiconductor Science and Technology*, vol. 11, p. 1464, 1996.
- [19] R. Sporken, C. Silien, F. Malengreau, K. Grigorov, R. Caudano, F. J. Sanchez, E. Calleja, E. Munoz, B. Beaumont, and P. Gibart, “XPS study of Au/GaN and Pt/GaN contacts,” *MRS Internet Journal Nitride Semiconductor Research*, vol. 1, no. 23, 1996.
- [20] Q. Z. Liu and S. S. Lau, “A review of the metal-GaN contact technology,” *Solid-State Electronics*, vol. 42, no. 5, pp. 677–691, 1998.
- [21] C. I. Wu and A. Kahn, “Investigation of the chemistry and electronic properties of metal/gallium nitride interfaces,” *Journal of Vacuum Science & Technology B: Microelectronics and Nanometer Structures*, vol. 16, p. 2218, 1998.
- [22] A. Barinov, L. Casalis, L. Gregoratti, and M. Kiskinova, “Au/GaN interface: Initial stages of formation and temperature-induced effects,” *Physical Review B*, vol. 63, no. 8, p. 85308, 2001.
- [23] A. D. Barinov, L. Casalis, L. Gregoratti, and M. Kiskinova, “Stages of formation and thermal stability of a gold-*n*-GaN interface,” *Journal of Physics D: Applied Physics*, vol. 34, pp. 279–284, 2001.
- [24] K. A. Rickert, A. B. Ellis, J. K. Kim, J. L. Lee, F. J. Himpsel, F. Dwikusuma, and T. F. Kuech, “X-ray photoemission determination of the Schottky barrier height of metal contacts to *n*GaN and *p*GaN,” *Journal of Applied Physics*, vol. 92, p. 6671, 2002.
- [25] A. R. Arehart, B. Moran, J. S. Speck, U. K. Mishra, S. P. DenBaars, and S. A. Ringel, “Effect of threading dislocation density on Ni/ *n*-GaN Schottky diode IV characteristics,” *Journal of Applied Physics*, vol. 100, p. 023709, 2006.
- [26] E. Monroy, F. Calle, T. Palacios, J. Sánchez-Osorio, M. Verdú, F. J. Sánchez, M. T. Montojo, F. Omnès, Z. Bougrioua, and I. Moerman, “Reliability of Schottky contacts on AlGaN,” *Physica Status Solidi (a)*, vol. 188, no. 1, pp. 367–370, 2001.

- [27] W. Götz, N. M. Johnson, R. A. Street, H. Amano, and I. Akasaki, "Photoemission capacitance transient spectroscopy of n -type GaN," *Applied Physics Letters*, vol. 66, no. 11, pp. 1340–1342, 1995.
- [28] D. Qiao, L. S. Yu, S. S. Lau, J. M. Redwing, J. Y. Lin, and H. X. Jiang, "Dependence of Ni/AlGa_N Schottky barrier height on Al mole fraction," *Journal of Applied Physics*, vol. 87, p. 801, 2000.
- [29] F. Binet, J. Y. Duboz, N. Laurent, E. Rosencher, O. Briot, and R. L. Aulombard, "Properties of a photovoltaic detector based on an n -type GaN Schottky barrier," *Journal of Applied Physics*, vol. 81, p. 6449, 1997.
- [30] I. Shalish, L. Kronik, G. Segal, Y. Shapira, M. Eizenberg, and J. Salzman, "Yellow luminescence and Fermi level pinning in GaN layers," *Applied Physics Letters*, vol. 77, p. 987, 2000.
- [31] R. H. Fowler, "The analysis of photoelectric sensitivity curves for clean metals at various temperatures," *Physical Review*, vol. 38, no. 1, p. 45, 1931.
- [32] S. Picozzi, A. Continenza, G. Satta, S. Massidda, and A. J. Freeman, "Metal-induced gap states and Schottky barrier heights at nonreactive GaN/noble-metal interfaces," *Physical Review B*, vol. 61, no. 24, p. 16736, 2000.
- [33] S. Kurtin, T. C. McGill, and C. A. Mead, "Fundamental transition in the electronic nature of solids," *Physical Review Letters*, vol. 22, no. 26, pp. 1433–1436, 1969.
- [34] J. S. Foresi and T. D. Moustakas, "Metal contacts to gallium nitride," *Applied Physics Letters*, vol. 62, no. 22, p. 2859, 1993.
- [35] J. D. Guo, M. S. Feng, R. J. Guo, F. M. Pan, and C. Y. Chang, "Study of Schottky barriers on n -type GaN grown by low-pressure metalorganic chemical vapor deposition," *Applied Physics Letters*, vol. 67, p. 2657, 1995.
- [36] T. Mori, T. Kozawa, T. Ohwaki, Y. Taga, S. Nagai, S. Yamasaki, S. Asami, N. Shibata, and M. Koike, "Schottky barriers and contact resistances on p -type GaN," *Applied Physics Letters*, vol. 69, no. 23, pp. 3537–3539, 1996.
- [37] D. K. Schroder, *Semiconductor Material and Device Characterization*. John Wiley and Sons, 1990.
- [38] S. R. McHale, J. W. McClory, J. C. Petrosky, J. Wu, R. Palai, P. A. Dowben, and I. Ketsman, "The effective surface debye temperature of Yb:Ga_N," *Materials Letters*, vol. 65, p. 1476, 2011.
- [39] M. H. Kim, S. N. Lee, C. Huh, S. Y. Park, J. Y. Han, J. M. Seo, and S. J. Park, "Interfacial reaction and Fermi level movement induced by sequentially deposited metals on GaN: Au/Ni/GaN," *Physical Review B*, vol. 61, no. 16, pp. 10 966–10 971, 2000.

- [40] V. M. Bermudez, T. M. Jung, K. Doverspike, and A. E. Wickenden, “The growth and properties of Al and AlN films on GaN (0001)-(1 (times) 1),” *Journal of Applied Physics*, vol. 79, no. 1, p. 110, 1996.
- [41] V. M. Bermudez, D. D. Koleske, and A. E. Wickenden, “The dependence of the structure and electronic properties of wurtzite GaN surfaces on the method of preparation,” *Applied Surface Science*, vol. 126, no. 1-2, pp. 69–82, 1998.
- [42] W. Xiao, Q. Guo, Q. Xue, and E. G. Wang, “Gd on GaN (0001) surface: Growth, interaction, and Fermi level movement,” *Journal of Applied Physics*, vol. 94, p. 4847, 2003.
- [43] J. I. Pankove and H. Schade, “Photoemission from GaN,” *Applied Physics Letters*, vol. 25, no. 1, pp. 53–55, 1974.
- [44] M. G. Ramchandani, “Energy band structure of gold,” *Journal of Physics C: Solid State Physics*, vol. 3, p. S1, 1970.
- [45] H. Ebel and N. Gurker, “Deconvolution of the XPS-valence band spectrum of gold,” *Physics Letters A*, vol. 50, no. 6, pp. 449–450, 1975.
- [46] L. Ley, R. A. Pollak, F. R. McFeely, S. P. Kowalczyk, and D. A. Shirley, “Total valence-band densities of states of III-V and II-VI compounds from x-ray photoemission spectroscopy,” *Physical Review B*, vol. 9, no. 2, pp. 600–621, 1974.
- [47] S. Hüfner, *Photoelectron spectroscopy: principles and applications*. Springer Verlag, 2003.
- [48] P. W. Chye, I. Lindau, P. Pianetta, C. M. Garner, C. Y. Su, and W. E. Spicer, “Photoemission study of Au Schottky-barrier formation on GaSb, GaAs, and InP using synchrotron radiation,” *Physical Review B*, vol. 18, no. 10, pp. 5545–5559, 1978.
- [49] W. Mönch, *Semiconductor surfaces and interfaces*. Springer Verlag, 2001.
- [50] D. R. Penn, “Electron mean-free-path calculations using a model dielectric function,” *Physical Review B*, vol. 35, no. 2, pp. 482–486, 1987.
- [51] M. P. Seah and W. A. Dench, “Quantitative electron spectroscopy of surfaces: A standard data base for electron inelastic mean free paths in solids,” *Surface and Interface Analysis*, vol. 1, no. 1, pp. 2–11, 1979.
- [52] J. Venables, *Introduction to surface and thin film processes*. Cambridge Univ Pr, 2000.
- [53] J. A. Venables, “Atomic processes in crystal growth,” *Surface Science*, vol. 299, pp. 798–817, 1994.

- [54] Q. Z. Liu, K. V. Smith, E. T. Yu, S. S. Lau, N. R. Perkins, and T. F. Keuch, "On the epitaxy of metal films on GaN," *Materials Research Society Symposium Proceedings*, vol. 449, p. 1079, 1996.
- [55] G. L. Lay, D. Mao, A. Kahn, Y. Hwu, and G. Margaritondo, "High-resolution synchrotron-radiation core-level spectroscopy of decapped GaAs (100) surfaces," *Physical Review B*, vol. 43, no. 17, pp. 14 301–14 304, 1991.
- [56] W. R. L. Lambrecht, B. Segall, S. Strite, G. Martin, A. Agarwal, H. Morkoc, and A. Rockett, "X-ray photoelectron spectroscopy and theory of the valence band and semicore Ga 3*d* states in GaN," *Physical Review B*, vol. 50, no. 19, pp. 14 155–14 160, 1994.
- [57] D. E. Eastman, "Photoelectric work functions of transition, rare-earth, and noble metals," *Physical Review B*, vol. 2, no. 1, pp. 1–2, 1970.
- [58] M. V. Nikolic, S. M. Radi, V. Mini, and M. M. Risti, "The dependence of the work function of rare earth metals on their electron structure," *Microelectronics Journal*, vol. 27, no. 1, pp. 93–96, 1996.
- [59] E. M. Savitskiy, V. F. Terekhova, and E. V. Maslova, "Thermoelectron emission of Yttrium, Scandium, and Erbium," *Radio Engr Electron Phys*, vol. 7, p. 1233, 1967.

VII. Neutron Detection Using Gadolinium

7.1 Overview

Owing to the fact that neutron detection offers the greatest likelihood to identify the presence of special nuclear material, this chapter will examine the rare earth metal gadolinium in that capacity. The thermal neutron capture cross section of ^{157}Gd (255,000 barns) is the largest of all known natural isotopes, which distinguishes the material as a logical candidate for neutron detection. Recall that neutron detection requires the conversion of neutrons to ionizing radiation that generates electron-hole pairs via energy deposition in the active collection volume of a device. Ignoring contact types for the following discussions, the charge produced from a single ^{157}Gd neutron capture event will be analyzed and compared to the intrinsic noise level of typical commercially available charge-to-voltage preamplifiers. Next, material and geometry considerations will be discussed and applied to multiple capture events due to a hypothetical neutron flux. The single and multiple event calculations will be compared to boron carbide (B_5C), which is an emerging material in the field of solid state neutron detectors. Although the calculations presented in the subsequent sections are somewhat idealized, they serve to identify those parameters of device design that might be suited for further analysis via detailed computational modeling prior to device fabrication. Additionally, the fundamental calculations serve to answer overarching questions associated with an engineering study of this type, to include:

- (1) Can a ^{157}Gd neutron capture event generate a signal that is detectable above the intrinsic noise of the pulse processing electronics and the leakage current of a typical diode?
- (2) What is the anticipated frequency response of the diode in the presence of a thermal neutron flux?

- (3) What are the ranges and mean free paths in a Gd-based semiconductor for the charged particles and photons created in a capture event, and how do those distances compare with the depletion width of the diode?
- (4) How do Gd-based devices perform against the boron carbide benchmarks for single and multiple capture events?

7.2 Single Neutron Capture Event

7.2.1 Gd-157 Neutron Capture Scheme.

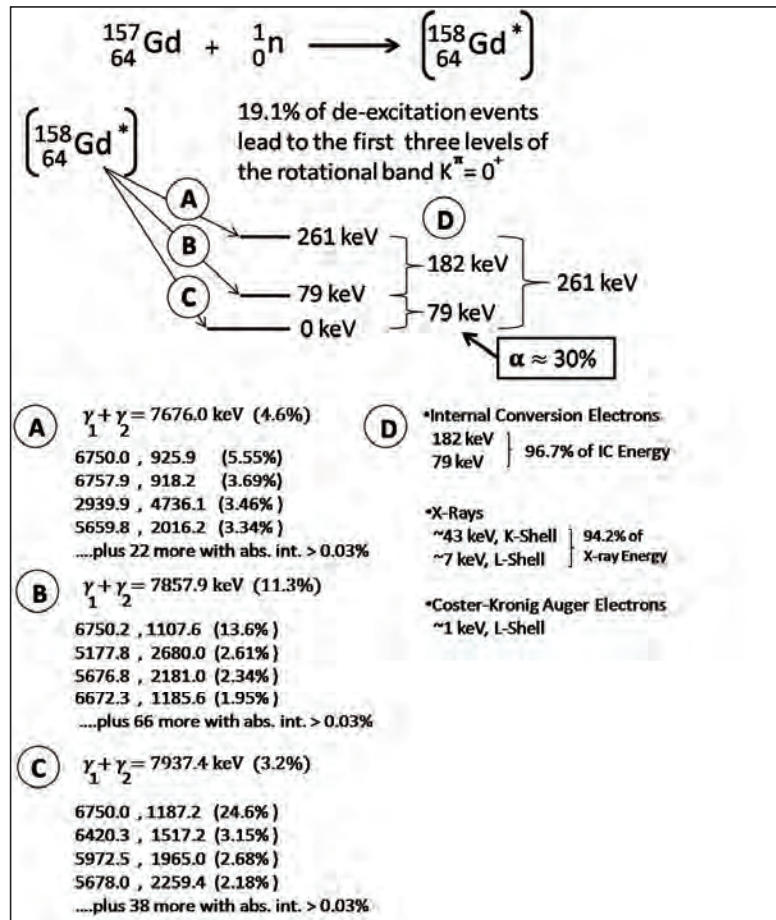


Figure 38. De-excitation schemes of $^{158}\text{Gd}^*$ following neutron capture by ^{157}Gd . Adapted from [1–3].

To determine the amount of energy available for electron-hole pair production in a Gd-based semiconductor device, the ^{157}Gd neutron capture and subsequent de-

excitation reactions must be examined. Neutron capture by ^{157}Gd results in an excited, or compound $^{158}\text{Gd}^*$ nucleus that is 7937 keV from the ground state energy of ^{158}Gd . The compound nucleus can decay to the ground state by several paths, and 19.1% of these de-excitations are well understood and summarized in Figure 38.

Decay path C in the figure is the most straightforward, occurs 3.2% of the time, and results in coincident emission of two gamma rays (γ_1, γ_2) whose energy sum equals 7937 keV, as expected. The distribution of the gamma ray energies and their probabilities of occurrence are listed below the gamma ray energy sum at the lower left corner of the figure. Decay paths A and B occur 4.6% and 11.3% of the time, respectively, and result in a $^{158}\text{Gd}^*$ nucleus that is 261 keV and 79 keV, respectively, from the ground state energy of ^{158}Gd . The decays to those energy levels produce gamma rays whose energy sum equals (7937 keV - 261 keV) and (7937 keV - 79 keV) for paths A and B, respectively, and their probabilities of occurrence are listed below their gamma ray energy sums. Following these initial decays, and shown as event D in the figure, the $^{158}\text{Gd}^*$ nucleus may decay to the ground state energy of ^{158}Gd via emission of a 182 keV or 79 keV gamma ray, or through the competing process of internal conversion electron emission.

Internal conversion (IC) occurs when the excited nucleus transfers energy to an atomic electron, typically in the K ($n = 1$) or L ($n = 2$) electronic shell, where n is the principle quantum number. The preference for the competing processes of IC and gamma emission is described by the internal conversion coefficient α as

$$\alpha = \frac{N_e}{N_\gamma}, \quad (84)$$

where N_e and N_γ are the number of internal conversion electrons and gamma photons, respectively, for the nuclear transition. This coefficient increases with the cube of the atomic number and decreases with E^* ; thus, internal conversion is prevalent in the

decay of low-lying excited states (small E^*) of heavy nuclei [4]. Lastly, the kinetic energy E_e of the ejected atomic electron is very nearly equal to the difference between the excitation energy of the E^* nucleus and the binding energy of the electronic shell E_B as

$$E_e = E^* - E_B. \quad (85)$$

Returning to Figure 38, the internal conversion coefficient for the 79 keV transition is expected to be 0.3. This predicts that 30% of 11.3% of events from transition $B \rightarrow C$ will result in IC emission, or 3.4% of all ^{157}Gd neutron capture events. It follows that 30% of 4.6%, or 1.4% of events from transition $A \rightarrow B$ ($\Delta E = 182$ keV) will result in IC emission. As IC for Gd is known to be preferential to L -shell electron emission [5], and the average L -shell binding energy for Gd has been theoretically calculated and experimentally verified to be approximately 7 keV [6], equation (85) predicts that 72 keV electron emission will dominate capture events that result in IC. The vacancy following ejection of an IC electron from a low-lying electronic orbital will be filled by an electron from a higher orbital, which will cause the higher orbital's vacancy to be filled by an electron from another outer orbital, and the downward cascade will continue. The corresponding energy difference between electronic orbitals results in a series of characteristic X-rays of approximately 43 keV and 7 keV for $L \rightarrow K$ and $M \rightarrow L$ transitions, respectively [6]. The energy difference may also be transferred to an L -shell electron, in which case an Auger electron will be emitted with a kinetic energy equal to the difference between the transition and the binding energy of the electronic state from which it originated, or approximately 35 keV.

If the detailed examination of the $^{157}\text{Gd}(n, \gamma)^{158}\text{Gd}$ reaction above appeared tedious, full understanding of the ensuing reactions facilitates detector design dimensions and detection equipment settings to ensure prudent discrimination when analyzing spectral features. The salient points of the analysis are summarized as follows:

- (1) less than 5% (3.4% + 1.4%) of all ^{157}Gd neutron capture events produce charged particles (internal conversion and Auger electrons) capable of generating electron-hole pairs in a Gd-based semiconductor device,
- (2) relatively low energy (keV-range) photon production occurs in
 - (a) decay chain D via emission of 43 keV K -shell and 7 keV L -shell characteristic X-rays, following internal conversion electron emission,
 - (b) decay chain D where 182 keV and 79 keV gamma rays are emitted for 3.2% (70% of 4.6%) and 7.9% (70% of 11.3%), respectively, of transitions,
- (3) the dominant high energy photon (MeV-range) production occurs in decay chain B, where 13.6% of 11.3%, or 1.5% of transitions produce coincident gamma rays of 6.7 MeV and 1.1 MeV.

Alternatively, the significant reactions discussed above, which account for nearly all of the $^{158}\text{Gd}^*$ de-excitations, may be tabulated as shown in Table 5.

Table 5. Summary of ionizing radiation produced from neutron capture by ^{157}Gd .

Absolute Intensity [%]	Radiation Produced	Energy(ies)	Decay Chains
3.4	IC electron	72 keV	B,D
	K -shell X-ray	43 keV	
	L -shell X-ray	7 keV	
1.4	IC electron	174 keV	A,D
	K -shell X-ray	43 keV	
	L -shell X-ray	7 keV	
7.9	γ -ray	79 keV	B
3.2	γ -ray	182 keV	A
1.5	γ -ray	1.1, 6.7 MeV	B
	KLL Auger electron	35 keV	
	LMM Auger electron	6 keV	

7.2.2 Ionizing Radiation Charge Production.

The quantity of electron-hole pairs produced by ionizing energy loss events is dominated by the bandgap of the semiconductor in which they were created. Consider a single ^{157}Gd neutron capture event that results in a 72 keV internal conversion

electron. Assuming a cost of approximately $3E_g$ per electron-hole pair [7], and that the internal conversion electron is doing most of the work E_{ion} , the maximum charge Q_{max} that can be created from a single event is given as

$$Q_{\text{max}} = \frac{E_{\text{ion}}}{3E_g} \times (1.6 \times 10^{-19}) \quad [\text{C}]. \quad (86)$$

The bandgap for $\text{Gd}_x\text{Ga}_{1-x}\text{N}$ is assumed to vary linearly as a function of molar concentration x between GdN (1.0 eV) and GaN (3.4 eV) as

$$E_g [\text{Gd}_x\text{Ga}_{1-x}\text{N}] = x E_g [\text{GdN}] + (1 - x) E_g [\text{GaN}]. \quad (87)$$

Charge generation dependence upon semiconductor bandgap for a single ^{157}Gd neutron capture event, via (86) and (87), is depicted in Figure 39 for $\text{Gd}_x\text{Ga}_{1-x}\text{N}$. The

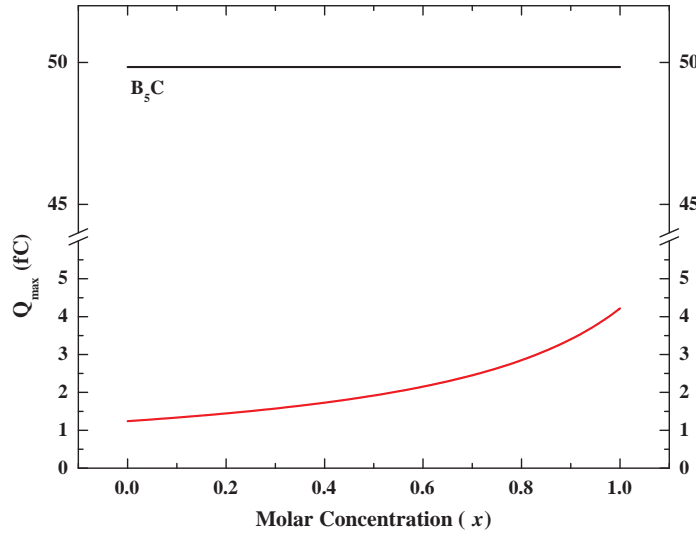
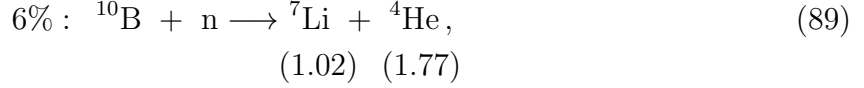
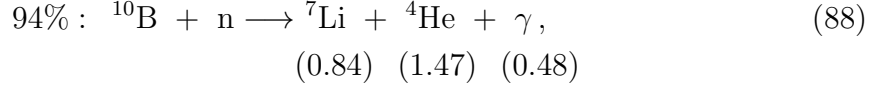


Figure 39. Q_{max} creation from (red): a single ^{157}Gd neutron capture event resulting in 79 keV internal conversion electron emission, as a function of molar concentration x in $\text{Gd}_x\text{Ga}_{1-x}\text{N}$; (black): a single neutron capture event in B_5C resulting in 0.84 MeV ^7Li ion production, as shown in (88).

figure indicates that the charge generated varies between 1.2 fC for GaN and 4.2 fC

for GdN. As a benchmark for comparison, the boron conversion reactions in a B₅C device were considered



where the branching ratios and reaction product energies (MeV) are shown to the left and beneath the reactions, respectively. Using the most conservative charged particle energy (0.84 MeV) and assuming a B₅C bandgap of 0.9 eV [8], Figure 39 shows that the charge generated from a single neutron capture event is more than an order of magnitude greater in B₅C than in GdN.

7.3 Detector Circuit Considerations

The charge produced from the interaction of a single particle must be collected to form a basic electrical signal. This collection is accomplished typically by the imposition of an electric field within the detector. The collection time t_c can be approximated as

$$t_c = \frac{d}{v}. \quad (90)$$

Here, d is the charge collection distance and v is the drift velocity expressed as a function of charge mobility μ [cm² V⁻¹ sec⁻¹] and the applied electric field \mathcal{E} as

$$v = \mu\mathcal{E}. \quad (91)$$

Therefore, the transient current I_t produced by a single event radiation-induced charge pulse is expressed as the ratio of equations (86) and (90) as

$$I_t = \left(\frac{qE_{\text{ion}}}{3E_g} \right) \left(\frac{\mu\mathcal{E}}{d} \right). \quad (92)$$

Assuming a typical diode leakage current on the order of 10^{-9} A, a rough comparison between the transient and leakage currents can be made for a Gd-based device. Using $\mu = 1 \text{ cm}^2 \text{ V}^{-1} \text{ sec}^{-1}$, $\mathcal{E} = 10^5 \text{ V cm}^{-1}$, and d corresponding to a depletion width of $5\mu\text{m}$ as reasonable order of magnitude estimates, yields $I_t \sim 0.2\mu\text{A}$, which is two orders of magnitude above the leakage current. As a first approximation, and under ideal conditions, the transient current is, as a minimum, marginally better than leakage.

For a prototype detector, the current pulse may be illustrated as shown in Figure 40, and it follows from the figure that the time-integrated current over the duration

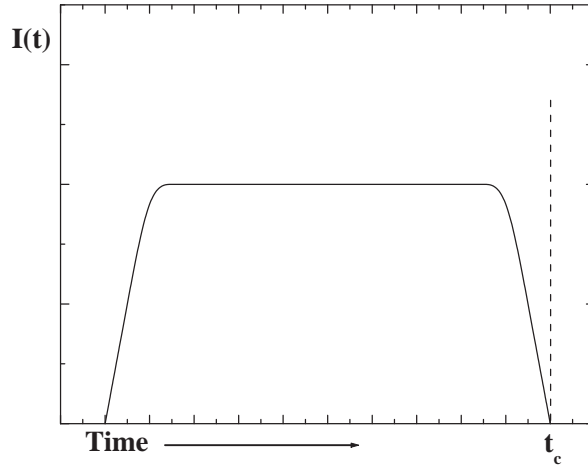


Figure 40. Example of detector current pulse where t_c represents collection time. Adapted from [5].

of the pulse collection time must equal the collected charge Q , or

$$\int_0^{t_c} I(t) dt = Q. \quad (93)$$

Whereas Figure 40 shows a symmetric pulse, in practice, many pulses will be asymmetric, owing to time dependent current fluctuations. It is also assumed that either the radiation interaction rate is low enough, or the time constant of the external circuit is small compared to the charge collection time, so that each individual interaction gives rise to a distinguishable current. In most detection applications, the time integral of each transient current, or total charge Q , is recorded, and the deposited energy in the detector is related directly to Q . In applications designed to measure the energy of individual events, as would be required to identify an individual internal conversion electron following neutron capture by ^{157}Gd , the pulse mode of detector operation is best [5]. As an example, the pulse height spectra for a B_5C heterojunction neutron detector in the presence of various reactor fluxes [9] is shown in Figure 41 and clearly discerns the dominant spectral features predicted by the boron neutron capture reactions (88) and (89).

In practice, generating pulse height spectra for a solid state neutron detector as shown in Figure 41 requires the detector to be connected to pulse processing electronic equipment. This requirement is levied owing to the fact that the generated charge is so small that signal pulses require an intermediate amplification step. The elements of a typical pulse height spectrometry signal chain are shown in Figure 42. The voltage supply imposes the applied electric field in the detector, such that the radiation induced charge may be collected, converted to a voltage, amplified, and pulse-shaped after departing the preamplifier-amplifier configuration. The significant contribution to noise occurs at the beginning of the signal chain, when the signal is minimized. Any noise contribution at this point undergoes the same amplification as

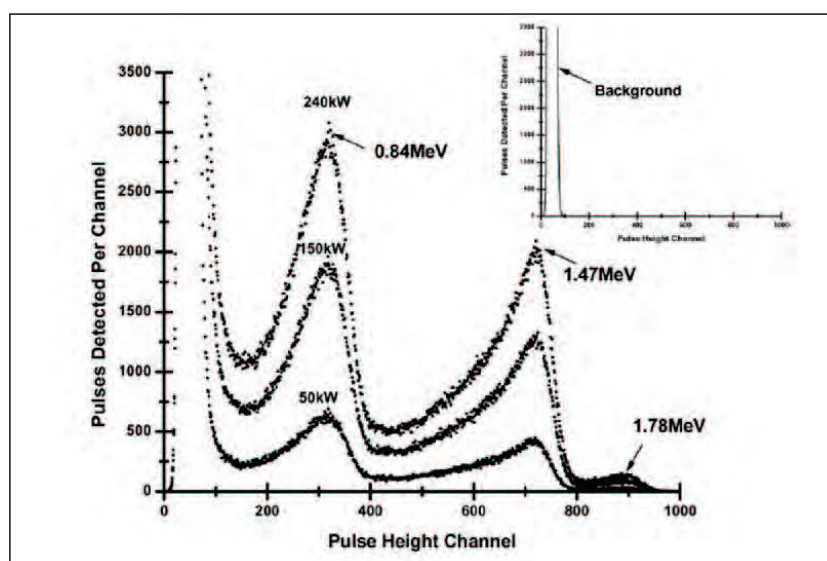


Figure 41. Pulse height spectra and background (inset) from a B_5C heterojunction detector. Each spectra was collected for 600 seconds at the reactor power indicated. The three identifiable peaks are attributable to the boron capture products shown in reactions (88) and (89). The 1.02 MeV peak is lost in the continuum between the 0.84 MeV and 1.47 MeV peaks owing to its branching ratio [9].

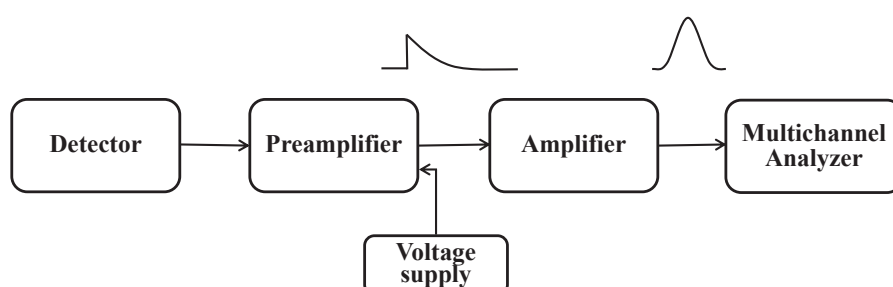


Figure 42. Elements of a typical signal chain for pulse height analysis. Adapted from [5].

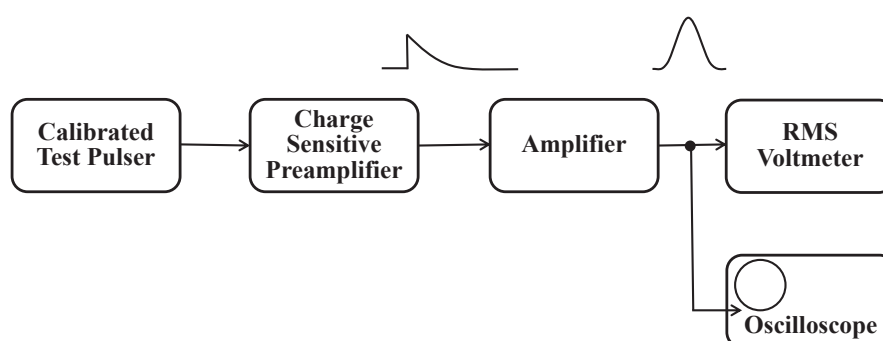


Figure 43. System for measuring charge-sensitive preamplifier noise.

the signal, whereas noise generated during later stages in the signal chain is typically much smaller than the signal. It is therefore of significant interest to know whether the charge generated by a ^{157}Gd neutron capture event exceeds the intrinsic noise level of the preamplifier input stage.

The intrinsic noise level of a charge-sensitive commercial preamplifier, typically expressed as a function of input capacitance, is determined by charge injection into the preamplifier, as shown in Figure 43. The charge can be injected by a detector and radiation source or a step pulse generator connected to the preamplifier input through a capacitor, sometimes referred to as a charge terminator. The preamplifier noise can be determined by measuring the root-mean-square (rms) noise voltage V_{rms} at the output of the filter amplifier in the absence of any pulses. The ratio V_{rms}/V_p , referred to as the equivalent noise charge [5], and reported in either eV or number of electrons, is used to determine noise as

$$\text{FWHM (noise)} = 2.35 \epsilon \frac{V_{\text{rms}}}{V_p} \text{ [eV]}, \quad (94)$$

where ϵ is the deposited energy required to create one charge carrier. Typical capacitance-dependent performance values are based upon the silicon equivalent ($\epsilon = 3.6 \text{ eV}$) and range between 2–27 keV for commonly used ORTEC systems [10]. Conversion to the corresponding number of electrons is done by dividing the reported values by the silicon equivalent, which yields a range of 555–7500 electrons, or an equivalent noise charge of approximately 0.1–1.2 fC. Keeping in mind that manufacturer performance specifications are determined under ideal conditions, the charge generated from a ^{157}Gd neutron capture event, as shown in Figure 39, approaches the intrinsic noise level of many commercially available charge-to-voltage preamplifiers.

On the basis of charge collection, the governing physics implies marginal performance of Gd-based semiconductor neutron detectors. However, if the preamplifier

gain can be minimized to account for the low charge production, gadolinium may warrant consideration as a detection material. Assuming the pulse processing electronics can be optimized as stated, the charge collection analysis conducted above reveals nothing about the anticipated count rate or collection time required to obtain statistically significant data in a pulse height spectrum. In order to predict this detector response, one must account for material and geometry considerations such as neutron flux, capture cross section, detector collection volume, and conversion reaction branching ratios.

7.4 Material and Geometry Considerations

Assuming that a charge pulse resulting from a ^{157}Gd neutron capture event could be detected, the idealized pulse rate f_s may be determined as

$$f_s = \dot{R}_{\text{vol}} V_d \mathcal{K} \quad [\text{sec}^{-1}] . \quad (95)$$

The first term, volumetric reaction rate \dot{R}_{vol} , depends directly on the macroscopic capture cross section Σ_c and the thermal neutron flux Φ_{th} , or

$$\dot{R}_{\text{vol}} = \Sigma_c \Phi_{th} . \quad (96)$$

The macroscopic capture cross section is calculated as

$$\Sigma_c = N \sigma_c , \quad (97)$$

where σ_c is the microscopic neutron capture cross section in barns [10^{-24} cm^2] and N is the concentration of nuclei [cm^{-3}], calculated as

$$N = \frac{\rho N_{AV}}{M_{AW}} , \quad (98)$$

via the material density ρ , Avogadro's number N_{AV} , and the molar mass M_{AW} . The second and third terms in (95) are the detector collection volume V_d , and the conversion reaction branching ratio \mathcal{K} . Collection volume is calculated as

$$V_d = A_c W, \quad (99)$$

where A_c is the contact area and W is the depletion region of the solid state device. Assembling the components from (95)–(99), the idealized pulse rate is expressed as

$$f_s = \left(\frac{\rho N_{AV}}{M_{AW}} \right) (\sigma_c \Phi_{th} A_c W \mathcal{K}). \quad (100)$$

Assuming that collection volumes are identical for hypothetical B₅C and Gd-based diodes, and that both are subject to an identical neutron flux, f_s would scale linearly with the macroscopic capture cross section and branching ratio, making a comparison between the two materials straightforward. Using parameters summarized in Table 6, and assuming 100% ¹⁰B and ¹⁵⁷Gd in the diodes, the ratio of charge pulse rates in the ¹⁰B neutron capture reaction (88) and the ¹⁵⁷Gd neutron capture reaction in Figure 38 is $f_s(\text{B}_5\text{C}) / f_s(\text{GdN}) = 3.2/2.3 = 1.4$. Therefore, assuming

Table 6. Diode parameters for charge pulse rate comparison. Parameters common to both materials are: $\Phi_{th} = 10^4 \text{ n cm}^{-2}\text{s}^{-1}$; $A_c = \pi(0.1 \text{ cm})^2/4$; $W = 4.2 \mu\text{m}$

Material	ρ (g cm ⁻³)	M_{AW} (g mol ⁻¹)	σ_c (barn)	\mathcal{K}
B ₅ C	2.52	55.2	3840	0.94
GdN	2.30	171.2	2.55×10^5	(0.113) (0.30)

the pulse processing electronics can be optimized to account for the low charge production from a ¹⁵⁷Gd neutron capture event, the ratio of charge pulse rates above predicts that a pulse height spectrum for a Gd-based diode, such as that in Figure 41 for B₅C, would not be significantly reduced on the basis of the poor branching

ratio for internal conversion electron in ^{157}Gd , nor significantly improved owing to its favorable neutron capture cross section.

With questions (1) and (2) from Section 7.1 addressed, question (3) requires consideration. During device operation, the depletion width, and hence charge collection volume, are controlled by the bias conditions. Making the assumption that a Gd-based material could be grown on a substrate with a similar bandgap, like $p\text{-Si}$, such that an abrupt homojunction diode could be constructed, W is determined from

$$W = \left[\frac{2\epsilon_s}{q} \left(\frac{N_A + N_D}{N_A N_D} \right) (V_{bi} - V) \right]^{1/2}. \quad (101)$$

The dielectric constant ϵ_s and acceptor N_A and donor N_D concentrations are material properties and can, to some extent, be influenced during device fabrication. Additionally, the built in voltage V_{bi} is also a function of doping concentration as

$$V_{bi} = \frac{k_B T}{q} \ln \left(\frac{N_A N_D}{n_i^2} \right), \quad (102)$$

where n_i is the intrinsic carrier density. For the sake of brevity, full development of (101) and (102) will not be shown, but can be found in various semiconductor textbooks [11, 12].

The requirement to optimize the depletion width in a semiconductor device becomes apparent from inspection of pulse rate (95) and transient current (92). Specifically, any improvement to detection efficiency (f_s) has the opposite effect upon the minimum detectable level (I_t) within a detector. Furthermore, the effects of growth (doping) and device operation (bias) allow depletion widths to be engineered via (101) such that they approach the mean free path of the neutron capture reaction products. Figure 44 shows the bias dependent depletion width in a hypothetical Gd-based homojunction neutron detector, using estimates of $N_D = 10^{19}$, $N_A = 10^{14}$,

$n_i = 10^{10}$, and $\epsilon = 9$. As an example, during a low power application with a bias

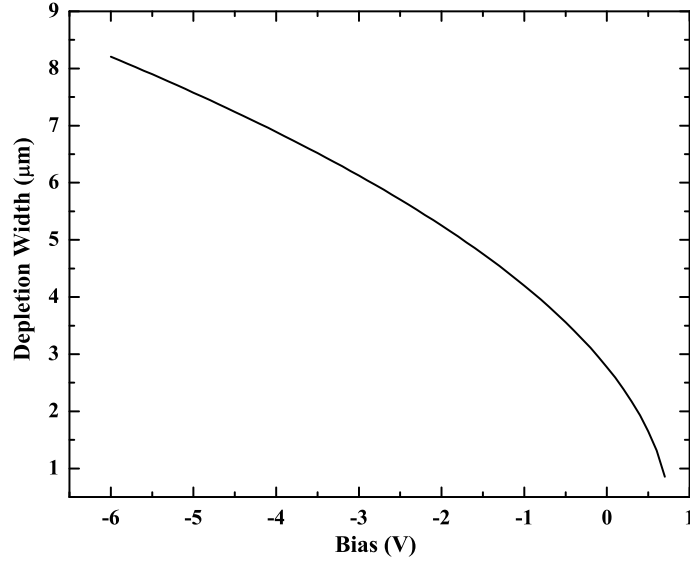


Figure 44. Depletion width as a function of bias for a hypothetical Gd-based (100% ^{157}Gd) homojunction neutron detector using $N_D = 10^{19}$ and $N_A = 10^{14}$.

of -1 V, $W = 4.2 \mu\text{m}$. Detailed parameter studies would reveal the full influence of depletion width upon the design considerations discussed above, but any analysis should, as a minimum, address the mean free paths of the electrons and photons summarized in Table 5.

Recall that a narrow beam of monoenergetic photons, with an incident intensity I_0 , interacting with a layer of material with thickness x and density ρ , will emerge with intensity I given by the exponential attenuation law

$$I(x) = I_0 e^{-\left(\frac{\mu}{\rho}\right) \rho x}, \quad (103)$$

where μ/ρ is the photon mass attenuation coefficient, which is a function of incident photon energy and absorber material density. Alternatively, photons can be characterized by their mean free path λ , which is the average distance traveled in an

absorber material before an interaction takes place, or

$$\lambda = \frac{\int_0^\infty x e^{-\mu x} dx}{\int_0^\infty e^{-\mu x} dx} = \frac{1}{\mu}. \quad (104)$$

NIST values [13] of μ/ρ for gadolinium oxysulfide at photon energies of 182 keV, 79 keV, 43 keV, and 7 keV from Table 5 are 0.481, 2.613, 5.854, and 130.6 cm² g⁻¹, respectively, and $\rho = 2.3$ g-cm⁻³. The resulting mean free paths are 9 mm, 2 mm, 700 μ m, and 33 μ m for the respective photon energies above. The possibility of a 7 keV photon interaction with the material cannot be ruled out from these calculations. However, the charge generated from a single event interaction would be ~ 0.1 fC, well below the intrinsic noise level of a commercial preamplifier. Therefore, the effects of photon interaction within the depletion widths of Figure 44 of the hypothetical diode are negligible.

Based on limited availability of data, electron interactions will be addressed more qualitatively. Theoretical electron mean free path calculations in solids [14, 15] are limited to electron kinetic energies up to ~ 10 keV, and range-energy plots for more energetic electrons are available for silicon [5], but are not obtainable for non-conventional semiconductor devices. However, in silicon, the internal conversion electrons created from neutron capture by ¹⁵⁷Gd have ranges of approximately 40–160 μ m [5]. Electron stopping power, and hence range, results from collisional and radiative electron energy losses, and scales linearly with electron density n . Therefore, the ratio of $n_{\text{Si}}/n_{\text{Gd}} \sim 1/5$ provides a very rough scaling factor for approximating the internal conversion electron range in a Gd-based semiconductor device. Based upon this scaling factor, the range of internal conversion electrons can be approximated as 5–20 μ m.

The most effective method to determine electron ranges is by Monte Carlo simulations, which are computational methods that rely on random sampling. In fact,

the estimate of electron range using fundamental physics and reasonable approximations is in fair agreement with CASINO and GEANT4 simulations [16,17]. CASINO, which predicts electron trajectories in solid materials, was used to determine the internal conversion electron penetration depth in a Gd_2O_3 on SiC diode, and found a mean penetration, for full energy deposition, of $\sim 26 \mu\text{m}$ [16]. However, out of the 10^5 incident electrons with 79 keV energy, only 21 fully deposited their energy at all ranges between 8–42 μm [16]. While many of the remaining electrons would have deposited a portion of their energy in the diode material, the generated charge would almost certainly fall below the intrinsic noise level of a commercial preamplifier.

GEANT is an abundant set of physics models designed to handle the interactions of particles with matter across a very wide energy range. Like CASINO, GEANT uses Monte Carlo simulations to replicate charged particle interactions with matter, but adds the flexibility to simulate neutral particles. Figure 45 is a schematic of a GEANT simulation [17] in which 10^6 thermal neutrons were incident on a Gd-doped HfO_2 thin film grown on a thick n -silicon wafer. Natural gadolinium was used ($\sim 16\% \text{ }^{157}\text{Gd}$), and the doping level of the Gd in HfO_2 was simulated at 15%. The depletion width at 1 V reverse bias was the full width of the Gd layer and 3 μm in silicon. Figure 46(a) shows that roughly 0.2% (or about 2000) of the incident neutrons produced electrons. The low production was attributed to the doping level in the HfO_2 [17], and the large range of electrons, relative to the depletion width, is another likely cause. The Auger and internal conversion electron peaks predicted by theory were observed in the simulation, as shown in Figure 46(a). Figure 46(b) shows the energy deposited in the thin film and the number of electrons that fully deposited their energy. As an example, there were just over 100 events that occurred where 30 keV was deposited in the active region of the diode (solid black line), and of those events, most were full depositions (red dashed line). Thus, a few events occurred where more energetic electrons deposited a portion of their energy in the

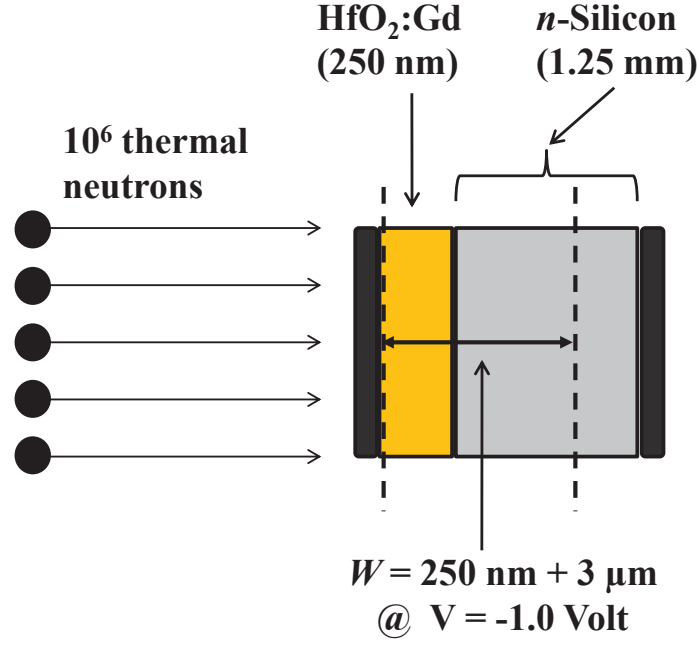
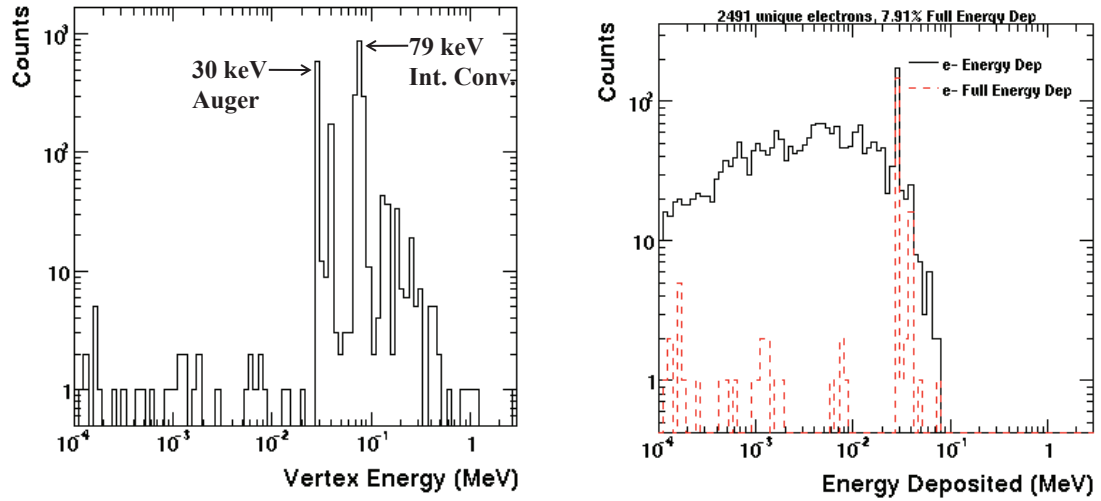


Figure 45. Schematic of GEANT4 simulation of thermal neutrons incident on $\text{HfO}_2\text{:Gd}$ on silicon heterojunction. The doping concentration was 15% natural Gd.



(a) The energy with which each electron is initially formed following neutron capture in natural gadolinium.

(b) Solid black: Total energy deposited by electrons in the active volume of the diode. Dashed red: Full energy deposition by electrons in the active detector.

Figure 46. GEANT4 simulation output [17].

active region. The dominant deposition at 30 keV in Figure 46(b) corresponds to a generated charge of 0.4 fC, which, unfortunately, is below the intrinsic noise level of many commercial preamplifiers.

The CASINO and GEANT4 simulations [16, 17] reinforce the challenges of low charge production from neutron capture by ^{157}Gd and large electron range relative to typical diode dimensions. However, there exists an opportunity to optimize the depletion width via doping concentrations during film growth and bias conditions during operation, which will be discussed later.

The disparity in capture cross section between the two materials also affects the quantity of neutron interactions. Recall that in a simplistic one-dimensional analysis, if a monoenergetic narrow beam neutron experiment were conducted, the entering neutron flux Φ_0 would attenuate exponentially [5, 18], via the neutron capture process, with absorber thickness x as

$$\Phi(x) = \Phi_0 e^{-\Sigma_c x} . \quad (105)$$

Alternatively, (105) permits the fraction of neutrons deposited in material \mathcal{F} to be expressed as

$$\mathcal{F} = 1 - \frac{\Phi(x)}{\Phi_0} = 1 - e^{-\Sigma_c x} . \quad (106)$$

A graph of (106) is shown in Figure 47 for B_5C (100 % ^{10}B) and GdN (100 % ^{157}Gd) homojunctions and clearly indicates that the massive cross section of ^{157}Gd most significantly affects device design for the parameter of film thickness. Simply stated, an equivalent number of neutron capture events would occur for much thinner Gd-based films compared to B_5C films. As an example, the fraction of neutrons absorbed in a $10\text{ }\mu\text{m}$ B_5C film would required a ^{157}Gd film thickness of $0.5\text{ }\mu\text{m}$.

In theory, film thickness appears to be a significant design advantage for Gd-based devices over their boron counterparts. However, in practice, and as discussed

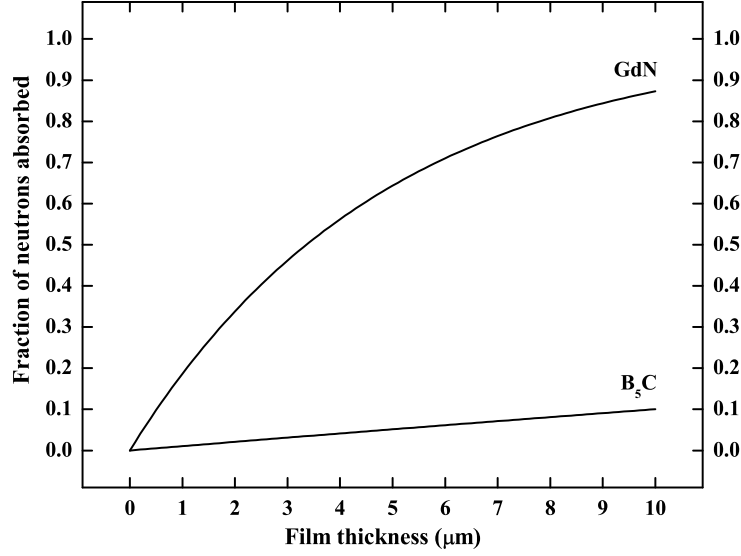


Figure 47. Fraction of absorbed neutrons as a function of film thickness for B₅C and GdN. A one dimensional monoenergetic narrow beam of thermal neutrons is assumed.

earlier, the range of internal conversion electrons created from neutron capture by ¹⁵⁷Gd is likely about 20–25 μm, and is larger than the range of the heavy charged particles created from neutron capture by B₅C. Therefore, thicker depletion widths would be required to achieve full energy deposition of the neutron-capture-generated internal conversion electrons, which might also limit the gamma-blindness of a detector. Furthermore, to generate a depletion width of 25 μm would require a bias of –62.1 V, using the parameters discussed for Figure 44. Thus, low power operation would be inhibited.

Figure 48 shows the dependence of mean free path on photon energy for natural Gd, determined from photon energy dependent μ/ρ values from the NIST database [13] and using $\rho = 7.9 \text{ g cm}^{-3}$ for Gd; GaN has $\rho = 6.1 \text{ g cm}^{-3}$. The figure indicates that a diode depleted to the full 25 μm range of internal conversion electrons created from neutron capture by ¹⁵⁷Gd will be gamma blind to photons with $h\nu > 17 \text{ keV}$. The possibility of depletion region interactions between photons with energies below this threshold and a diode with a comparable material density cannot be ruled out,

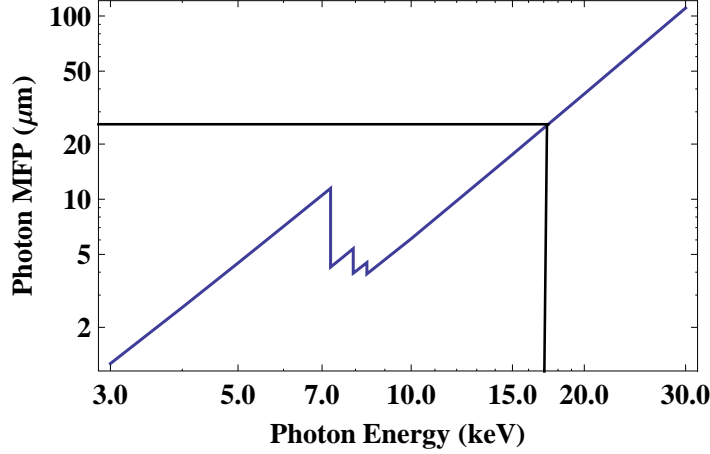


Figure 48. Photon energy dependent mean free path λ , determined from NIST-tabulated [13] values of μ/ρ for natural Gd.

based upon the anticipated reaction dependent photon energies discussed in Section 7.2.2. The likelihood also exists for higher energy photons to be Compton scattered below the gamma discrimination energy. However, a 17 keV energy deposition in the active region of an ideal $\text{Gd}_x\text{Ga}_{1-x}\text{N}$ $p-n$ homojunction diode corresponds to a generated charge of $0.4(x=0)$ – $0.9(x=1)$ fC, which is below the intrinsic noise level of many commercial preamplifiers. Thus, it is expected that a diode depleted to the 25 μm range of 79 keV internal conversion electrons will be either gamma blind or charge insensitive to gamma ray interactions within the depletion region.

In the end, the calculations presented here are made possible under the critical assumption that the charge generated in a Gd-based semiconductor by an internal conversion electron created from ^{157}Gd neutron capture exceeds the intrinsic noise level of the preamplifier required for pulse height analysis. Based upon previous research [1, 16] and topical review of solid state neutron detection [19], this critical assumption may be invalid and gadolinium may, in fact, be “romanticized,” as predicted by many researchers. This is not to say that development of novel solid state neutron detectors using gadolinium should be abandoned, but until the pulse

processing electronics necessary to detect a neutron induced signal are improved, the endeavor may prove vexing. On the other hand, I find the words of John D. Rockefeller compelling:

I do not think there is any other quality so essential to success of any kind as the quality of perseverance. It overcomes almost everything, even nature.

References

- [1] C. M. Young, “Gadolinium Oxide / Silicon Thin Film Heterojunction Solid-State Neutron Detector,” Master’s thesis, Air Force Institute of Technology, 2010.
- [2] M. A. Ali, V. A. Khitrov, Y. V. Kholnov, A. M. Sukhovej, and A. V. Vojnov, “Properties of the ^{158}Gd compound state gamma-decay cascades,” *Journal of Physics G: Nuclear and Particle Physics*, vol. 20, pp. 1943–1953, 1994.
- [3] Y. Sakurai and T. Kobayashi, “Experimental verification of the nuclear data of gadolinium for neutron capture Therapy,” *Journal of Nuclear Science and Technology, Supplement*, vol. 2, pp. 1294–1297, 2002.
- [4] J. E. Turner, *Atoms, Radiation, and Radiation Protection*. New York: John Wiley and Sons, 1995.
- [5] G. F. Knoll, *Radiation Detection and Measurement*. Hoboken, NJ: John Wiley and Sons, 2000.
- [6] G. Shani, B. Laster, S. Rozin, G. V. Miloshevsky, and V. I. Tolkach, “Calculated electron energy levels in gadolinium atoms and utilization of the $^{157}\text{Gd}(\text{n}, \gamma)^{158}\text{Gd}$ reaction as a source of Auger electrons for tumor cells killing,” in *Engineering in Medicine and Biology Society, 2000. Proceedings of the 22nd Annual International Conference of the IEEE*, vol. 1, 2000.
- [7] C. A. Klein, “Bandgap dependence and related features of radiation ionization energies in semiconductors,” *Journal of Applied Physics*, vol. 39, no. 4, pp. 2029–2038, 1968.
- [8] J. E. Bevins, “Characterization of a Boron Carbide Heterojunction Neutron Detection,” Master’s thesis, Air Force Institute of Technology, 2011.

- [9] E. Day, M. J. Diaz, and S. Adenwalla, “Effect of bias on neutron detection in thin semiconducting boron carbide films,” *Journal of Physics D: Applied Physics*, vol. 39, p. 2920, 2006.
- [10] “ORTEC 142A, B, and C Preamplifiers,” ORTEC Corporation, online at <http://www.ortec-online.com>.
- [11] S. M. Sze, *Semiconductor Devices: Physics and Technology*. Hoboken, NJ: John Wiley and Sons, 2002.
- [12] S. M. Sze and K. N. Kwok, *Physics of Semiconductor Devices*. Hoboken, NJ: John Wiley and Sons, 2007.
- [13] “Tables of X-Ray Mass Attenuation Coefficients,” National Institute of Standards and Technology, online at: <http://www.nist.gov/physlab/data/xraycoef/index.cfm>.
- [14] M. P. Seah and W. A. Dench, “Quantitative electron spectroscopy of surfaces: A standard data base for electron inelastic mean free paths in solids,” *Surface and Interface Analysis*, vol. 1, no. 1, pp. 2–11, 1979.
- [15] D. R. Penn, “Electron mean-free-path calculations using a model dielectric function,” *Physical Review B*, vol. 35, no. 2, pp. 482–486, 1987.
- [16] B. R. Thomas, “Neutron Detection Using Gadolinium-Based Diodes,” Master’s thesis, Air Force Institute of Technology, 2011.
- [17] A. Bickley, C. Young, B. Thomas, J. McClory, P. Dowben, and J. Petrosky, “Performance evaluation of neutron detectors incorporating intrinsic Gd using a GEANT4 modeling approach,” in *Materials Research Society Proceedings*, Spring 2011.
- [18] R. A. Knief, *Nuclear Engineering: Theory and Technology of Commercial Nuclear Power*. Taylor & Francis, 1992.
- [19] A. N. Caruso, “The physics of solid-state neutron detector materials and geometries,” *Journal of Physics: Condensed Matter*, vol. 22, p. 443201, 2010.

VIII. Conclusions

8.1 Summary of Findings

During the past decade, rare earth doped semiconductors have generated considerable attention for their application in new optoelectronic devices [1–4], but incomplete understanding of the physical and electronic properties of these materials classifies rare earth doped GaN heterostructures as non-conventional, as compared to silicon-based devices. To determine the extent to which even low concentrations of a rare earth in a GaN host can alter device properties, investigations of the surface electronic structure and interface properties of $\text{RE}_x\text{Ga}_{1-x}\text{N}$ ($\text{RE} = \text{Gd}, \text{Er}, \text{Yb}$) semiconductors are necessary.

With these considerations in mind, X-ray photoemission spectroscopy was used to determine the effective Debye temperatures of gallium and ytterbium in GaN:Yb thin films. The similarity between their measured values suggested that substitutional occupation of a Ga site by a Yb ion occurs, which supports experimental data and theoretical calculations. Careful comparison of the Ga and Yb values indicated a slightly smaller effective Debye temperature of the Yb atom, which reflects a surface that is softened and strained, possibly due to an increased Yb–N bond length as compared to the Ga–N bond length.

Next, resonant photoemission for GaN thin films doped with various rare earths ($\text{RE} = \text{Gd}, \text{Er}, \text{Yb}$) was investigated using synchrotron based photon energy dependent photoemission spectroscopy, in order to probe what valence bands of the semiconductors have strong $4f$ and/or rare earth weight. The calculated Fano profiles predicted the experimentally observed $4d \rightarrow 4f$ super Coster-Kronig processes. Additionally, strong rare earth $4f$ weights were observed about 5–6 eV below the valence band maximum for Gd and Er doped GaN. For Yb, the photoemission resonance was much weaker, indicating that there was only a very little depletion of

the $4f^{14}$ occupancy, but strong hybridization with GaN was implicated. There was also evidence, from the selectivity of the resonant photoemission enhancement of the valence band, for strong $4f$ hybridization with the GaN valence bands, particularly within the Er $4f_{5/2}$ envelope. Furthermore, the resonant photoemission results strongly supported the predicted hybridization with the host lattice [5], and the expected $f-s$ hybridization [5–8]. The results on the placement of the occupied Gd, Er and Yb $4f$ levels, deep within the valence band, suggested that the intra-atomic $f-f$ transitions may be more ‘blue’ than predicted by many theoretical models, which has implications for both the physics and the device fabrication and engineering communities.

Device fabrication and neutron detector applications were explored more carefully by measuring the Schottky barrier heights at the gold to rare earth doped GaN interface for the Gd, Er, and Yb dopants via ultraviolet photoemission spectroscopy. The Au overlayer did not wet and cover the GaN surface, even with rare earth doping of the GaN. The photoemission studies showed that the Schottky barrier heights between Au and RE:GaN thin film samples were measured to be 1.68 ± 0.1 eV (Yb:GaN), 1.64 ± 0.1 eV (Er:GaN), and 1.33 ± 0.1 eV (Gd:GaN), which was 25–55% larger than those reported at the gold to undoped GaN interface [9–25]. This trend of the Schottky barrier heights followed the trend of the rare earth metal work function. These results were uniform for all of the rare earths studied, and imply further reduction in leakage currents as compared with undoped GaN devices. Moreover, the larger barrier height at the metal to rare earth doped GaN interface means that radiation-induced charge collection volumes are increased, and thus more efficient, over what would be the case in pure GaN devices.

Last, the utility of gadolinium as a neutron detection material in a hypothetical solid form direct conversion homojunction was examined using fundamental nuclear and semiconductor physics, and compared to a boron carbide benchmark. In the

single neutron detection limit, the charge produced in a Gd-based semiconductor by an internal conversion electron created from ^{157}Gd neutron capture was found to approach the intrinsic noise level of commercial preamplifiers required for pulse height analysis. In general, the fraction of captured neutrons, and hence efficiency, was maximized with Gd-layer thickness, and was found to exceed that of ^{10}B layers by at least an order of magnitude. However, the range of internal conversion electrons created from neutron capture by ^{157}Gd was estimated to be about 20–25 μm , which is larger than the range of the heavy charged particles created from neutron capture by B_5C . Therefore, thick Gd films ($\sim 30\text{--}40\ \mu\text{m}$) would be required to achieve full energy deposition of the neutron-capture-generated internal conversion electrons, which might also limit the gamma-blindness of a detector. Moreover, full depletion of a Gd-based homojunction to the range of the 72 keV internal conversion electrons required large bias of $V = -62.1\ \text{V}$, thus inhibiting low power operation. For gadolinium to warrant serious consideration as a neutron detection material will require maturation of preamplifier technology, such that the gain can be minimized to account for inherently low charge production.

8.2 Future Work

There are several natural experimental and computational extensions of the current findings toward future research. Researchers who are interested in semiconductor device characteristics could fabricate multiple Schottky diodes on a single GaN:RE thin film. The Schottky barrier could then be calculated from device current-voltage characteristics, as discussed in Chapter II. Ideally, metal contacts would be sputtered onto thin films to produce multiple diodes from a single sample, and I-V characteristics could be obtained either from a conventional source measurement unit (via soldered wires) or directly through a probe station coupled with a semiconductor characterization system. To summarize the method, the current-voltage characteris-

tic of a metal-semiconductor contact is

$$J = J_s (e^{qV/k_B T} - 1) , \quad (107)$$

$$J_s = A^* T^2 e^{-\Phi_{B,n}/k_B T} , \quad (108)$$

where J_s is the saturation current and A^* is the effective Richardson constant, in units of $\text{A}/\text{K}^2\text{-cm}^2$, which depends directly on the electron effective mass in the semiconductor material.

Experimental calculation of Schottky barrier heights via equations (107) and (108) is done as follows and as shown in Figure 49. For values of V such that

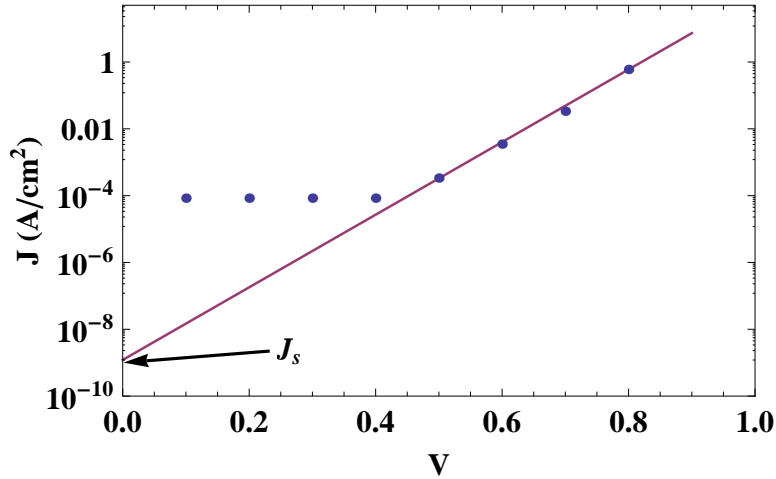


Figure 49. Logarithm of forward current density versus applied voltage for NTE555 PIN Schottky Diode (points) and least squares fit (line) in the linear region of the diode characteristic.

$qV > 3k_B T$, it follows that $J \approx J_s e^{qV/k_B T}$. The logarithm of current density

$$\ln J = \ln J_s + \frac{qV}{k_B T} , \quad (109)$$

versus applied forward voltage is plotted and extrapolated to $V = 0$, yielding a value

for J_s , from which the barrier height is obtained via (108) and knowledge of the effective Richardson constant. Figure 49 shows this procedure for a commercial NTE555 Schottky barrier PIN diode, which yielded a calculated saturation current density of 1.21 nA/cm^2 . Assuming a circular diode contact area of 0.55 mm^2 [26], and $A^* = 110$ for n -Si [27], (108) yields a Schottky barrier height of 0.94 eV . Experimental results of various metal- n -Si systems are known [28] to obey the empirical relationship

$$\Phi_{B,n} = 0.27\phi_m - 0.52. \quad (110)$$

Therefore, the calculated Schottky barrier height of 0.94 eV indicates that a high work function contact metal $\phi_m = 5.43 \text{ eV}$ was used in the NTE555 diode. Although the manufacturer's specifications do not identify the contact metal, common high work function metals such as Au and Pt have work function values that range from $5.10\text{--}5.42 \text{ eV}$ and $5.12\text{--}5.93 \text{ eV}$, respectively.

When the experimental data are plotted against the theoretical current density (107) using $\Phi_{B,n} = 0.94 \text{ eV}$ and the other parameters specified above, there is poor agreement between the results, as shown in Figure 50. The relatively weak correlation between data and theory is attributable to the fact that (107) assumes an ideality factor η of 1.0 . In practice [12, 13, 29, 30], a more accurate expression for the current density at metal-semiconductor interfaces and $p-n$ junctions [27, 28] is

$$J = J_s \left(e^{qV/\eta k_B T} - 1 \right), \quad (111)$$

where $1 \leq \eta \leq 2$.

For typical $p-n$ junctions, when ideal diffusion current dominates, $\eta = 1$, whereas when recombination current dominates, $\eta = 2$. Accordingly, when both currents are comparable, η has a value between $1\text{--}2$. For typical Schottky diodes with doping

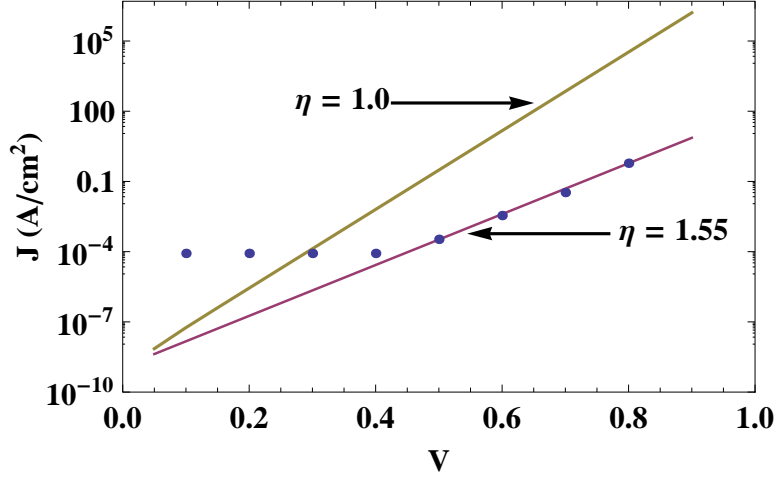


Figure 50. Logarithm of forward current density versus applied voltage for NTE555 PIN Schottky Diode (points) and theoretical current density (lines) for a Schottky contact with $\Phi_{B,n} = 0.94$ eV and ideality factors $\eta = 1$ (yellow) and $\eta = 1.55$ (purple).

concentrations $\leq 10^{17} \text{ cm}^{-3}$ operated at room temperature, the dominant current transport mechanism is thermionic emission of majority carriers from the semiconductor, over the potential barrier, and into the metal [27]. In this case, where tunneling current and depletion layer recombination are minimized, J is determined almost entirely by thermionic emission and η is close to unity. However, as doping concentrations increase, the probabilistic process of tunneling increases, owing to the increased occupancy of available states in the conduction band of the semiconductor. In this case, tunneling currents increase and η can be much larger than unity. The relationship between tunneling current and doping concentration for Au-Si Schottky diodes [28] shows that $\eta \approx 1.55$ when $N_D \approx 10^{19} \text{ cm}^{-3}$. Although the complete design details of the NTE555 Schottky barrier PIN diode are proprietary, the diode cannot be classified solely as either a $p-n$ junction or a Schottky diode. Therefore, it's likely that the calculated value of $\eta = 1.55$ for the NTE555 is due to a combination of $p-n$ junction recombination and Schottky barrier tunneling currents.

Regardless of the success or failure to reverse engineer design characteristics of the NTE55 Schottky barrier PIN diode, the process to calculate the Schottky barrier

via current-voltage characteristics is valid and may be applied to thin films used during this research. The calculated barrier heights from I-V characteristics could be compared to the values obtained via photoemission spectroscopy. If successful calculation of Schottky barrier heights via I-V characteristics were accomplished for all of the rare earth dopants studied during this research, the results may merit publication.

Researchers who are motivated by device modeling could examine device parameters and conduct sensitivity analyses for a Gd-based diode or other device structure in a thermal neutron environment. This research endeavor would most likely require integration of multiple computational tools, to include the GEometry AND Tracking (GEANT) toolkit, which can be used to accurately simulate the passage of both charged and neutral particles through matter, as well as a finite element device simulation code, such as Synopsis TCAD, to model the semiconductor device structure and characteristics. At least one researcher [31] has already conducted similar research for B₅C heterostructures, which would provide an interesting comparison.

One type of heterojunction application that may warrant consideration is the quantum well [28], depicted in Figure 51. Quantum wells use the differences between conduction band ΔE_C and valence band ΔE_V levels between two heterojunctions or three layers of materials in order to form barriers for charge carriers. In Figure 51, the middle GdN layer, of relatively low bandgap ($E_g \sim 1$ eV), is inserted between GaN:Gd layers, of relatively large bandgap ($E_g \sim 3$ eV), such that the middle layer has the lowest E_C for an electron well and the highest E_V for a hole well. Whereas electrons in a bulk semiconductor are free to move in three dimensions, a quantum well confines electrons or holes in a two-dimensional system. In this 2-D system, the solutions for the electron and hole wavefunctions inside the quantum well obey the Schrödinger equation, and the energy eigenvalues are quantized at distinct levels, shown as E_1 and E_2 in the figure. A critical parameter for quantum well design

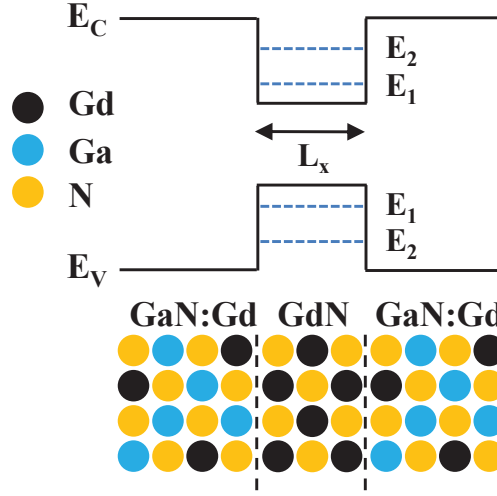


Figure 51. Single quantum well schematic.

is the well width L_x . If the well width is smaller than the de Broglie wavelength of the electron or hole, electron and hole wavefunctions between adjacent quantum well structures begin to overlap, and distinct energy minibands are formed in a superlattice structure, as shown in Figure 52.

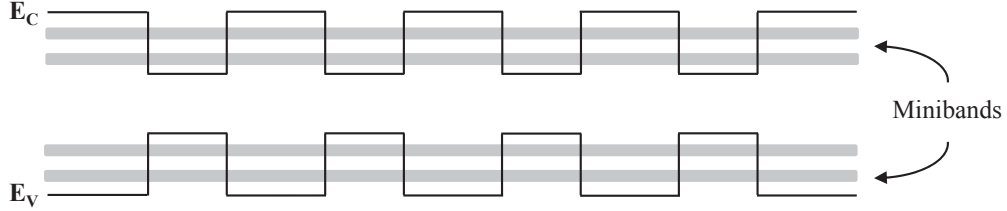


Figure 52. Superlattice structure schematic.

If multiple quantum wells can be grown and fabricated into a heterostructure superlattice, such that the generated charge from ^{157}Gd neutron conversion can be collected efficiently, the challenge of low charge generation may be abated. At this point, a quantum well or superlattice approach to neutron detection using Gd is a concept only, as good heteroepitaxy growth with the different materials is relatively unproven. However, under the assumption that structures could be fabricated, de-

tailed device modeling may provide a reasonable estimate of the charge collection efficiency of these devices.

An extension of the combined achievements of both research efforts discussed in the previous paragraphs could be measurement of the radiation response of a Gd-based diode in a thermal neutron environment, such as the AFIT thermal pile or The Ohio State University research reactor, and comparison with the computational model.

Lastly, researchers who are interested in the surface electronic structure and interface properties of thin film semiconductors might use photoemission spectroscopy to duplicate many of the experiments conducted during this research effort, but with an actinide rare earth, such as uranium. Plans to pursue this endeavor already exist.

References

- [1] T. Koubaa, M. Dammak, M. Kammoun, W. M. Jadwisieniczak, and H. J. Lozykowski, “Crystal field and Zeeman parameters of substitutional Yb³⁺ ion in GaN,” *Journal of Alloys and Compounds*, vol. 496, no. 1-2, pp. 56–60, 2010.
- [2] T. Koubaa, M. Dammak, M. Kammoun, W. M. Jadwisieniczak, H. J. Lozykowski, and A. Anders, “Spectra and energy levels of Yb³⁺ in AlN,” *Journal of Applied Physics*, vol. 106, no. 1, p. 013106, 2009.
- [3] W. M. Jadwisieniczak and H. J. Lozykowski, “Optical properties of Yb ions in GaN epilayer,” *Optical Materials*, vol. 23, no. 1-2, pp. 175–181, 2003.
- [4] A. J. Kenyon, “Recent developments in rare-earth doped materials for optoelectronics,” *Progress in Quantum Electronics*, vol. 26, no. 4-5, pp. 225–284, 2002.
- [5] G. M. Dalpian and S. H. Wei, “Electron-induced stabilization of ferromagnetism in Ga_{1-x}Gd_xN,” *Physical Review B*, vol. 72, no. 11, p. 115201, 2005.
- [6] T. Komesu, H. K. Jeong, J. Choi, C. N. Borca, P. A. Dowben, A. G. Petukhov, B. D. Schultz, and C. J. Palmstrm, “Electronic structure of ErAs (100),” *Physical Review B*, vol. 67, no. 3, p. 035104, 2003.

- [7] I. N. Yakovkin, T. Komesu, and P. A. Dowben, "Band structure of strained Gd (0001) films," *Physical Review B*, vol. 66, no. 3, p. 035406, 2002.
- [8] P. Strange, A. Svane, W. M. Temmerman, Z. Szotek, and H. Winter, "Understanding the valency of rare earths from first-principles theory," *Nature*, vol. 399, p. 756, 1999.
- [9] Y. Kribes, I. Harrison, B. Tuck, T. S. Cheng, and C. T. Foxon, "Investigation of Au Schottky contacts on GaN grown by molecular beam epitaxy," *Semiconductor Science and Technology*, vol. 12, p. 913, 1997.
- [10] L. He, X. J. Wang, and R. Zhang, "Enhanced electrical performance of Au/*n*-GaN Schottky diodes by novel processing," *Journal of Vacuum Science & Technology A: Vacuum, Surfaces, and Films*, vol. 17, p. 1217, 1999.
- [11] P. Hacke, T. Detchprohm, K. Hiramatsu, and N. Sawaki, "Schottky barrier on *n*-type GaN grown by hydride vapor phase epitaxy," *Applied Physics Letters*, vol. 63, no. 19, pp. 2676–2678, 1993.
- [12] S. C. Binari, H. B. Dietrich, G. Kelner, L. B. Rowland, K. Doverspike, and D. K. Gaskill, "Electrical characterisation of Ti Schottky barriers on *n*-type GaN," *Electronics Letters*, vol. 30, no. 11, pp. 909–911, 1994.
- [13] A. C. Schmitz, A. T. Ping, M. A. Khan, Q. Chen, J. W. Yang, and I. Adesida, "Schottky barrier properties of various metals on *n*-type GaN," *Semiconductor Science and Technology*, vol. 11, p. 1464, 1996.
- [14] R. Sporken, C. Silien, F. Malengreau, K. Grigorov, R. Caudano, F. J. Sanchez, E. Calleja, E. Munoz, B. Beaumont, and P. Gibart, "XPS study of Au/GaN and Pt/GaN contacts," *MRS Internet Journal Nitride Semiconductor Research*, vol. 2, no. 23, 1997.
- [15] Q. Z. Liu and S. S. Lau, "A review of the metal-GaN contact technology," *Solid-State Electronics*, vol. 42, no. 5, pp. 677–691, 1998.
- [16] C. I. Wu and A. Kahn, "Investigation of the chemistry and electronic properties of metal/gallium nitride interfaces," *Journal of Vacuum Science & Technology B: Microelectronics and Nanometer Structures*, vol. 16, p. 2218, 1998.
- [17] L. Casalis, A. Barinov, L. Gregoratti, and M. Kiskinova, "Au/GaN interface: initial stages of formation and temperature-induced effects," *Physical Review B*, vol. 63, no. 8, p. 85308, 2001.
- [18] A. Barinov, L. Casalis, L. Gregoratti, and M. Kiskinova, "Stages of formation and thermal stability of a gold-*n*-GaN interface," *Journal of Physics D: Applied Physics*, vol. 34, pp. 279–284, 2001.

- [19] K. A. Rickert, A. B. Ellis, J. K. Kim, J. L. Lee, F. J. Himpsel, F. Dwikusuma, and T. F. Kuech, "X-ray photoemission determination of the Schottky barrier height of metal contacts to n -GaN and p -GaN," *Journal of Applied Physics*, vol. 92, p. 6671, 2002.
- [20] A. R. Arehart, B. Moran, J. S. Speck, U. K. Mishra, S. P. DenBaars, and S. A. Ringel, "Effect of threading dislocation density on Ni/ n -GaN Schottky diode IV characteristics," *Journal of Applied Physics*, vol. 100, p. 023709, 2006.
- [21] E. Monroy, F. Calle, T. Palacios, J. Sánchez-Osorio, M. Verdú, F. J. Sánchez, M. T. Montojo, F. Omnès, Z. Bougrioua, and I. Moerman, "Reliability of Schottky contacts on AlGaIn," *Physica Status Solidi (a)*, vol. 188, no. 1, pp. 367–370, 2001.
- [22] W. Götz, N. M. Johnson, R. A. Street, H. Amano, and I. Akasaki, "Photoemission capacitance transient spectroscopy of n -type GaN," *Applied Physics Letters*, vol. 66, no. 11, pp. 1340–1342, 1995.
- [23] D. Qiao, L. S. Yu, S. S. Lau, J. M. Redwing, J. Y. Lin, and H. X. Jiang, "Dependence of Ni/AlGaIn Schottky barrier height on Al mole fraction," *Journal of Applied Physics*, vol. 87, p. 801, 2000.
- [24] F. Binet, J. Y. Duboz, N. Laurent, E. Rosencher, O. Briot, and R. L. Aulombard, "Properties of a photovoltaic detector based on an n -type GaN Schottky barrier," *Journal of Applied Physics*, vol. 81, p. 6449, 1997.
- [25] I. Shalish, L. Kronik, G. Segal, Y. Shapira, M. Eizenberg, and J. Salzman, "Yellow luminescence and Fermi level pinning in GaN layers," *Applied Physics Letters*, vol. 77, p. 987, 2000.
- [26] "NTE555 Silicon PIN Diode UHF/VHF Detector," online at <http://www.ntec.com/specs/500to599/pdf/nte555.pdf>.
- [27] S. M. Sze, *Semiconductor Devices: Physics and Technology*. Hoboken, NJ: John Wiley and Sons, 2002.
- [28] S. M. Sze and K. N. Kwok, *Physics of Semiconductor Devices*. Hoboken, NJ: John Wiley and Sons, 2007.
- [29] J. D. Guo, M. S. Feng, R. J. Guo, F. M. Pan, and C. Y. Chang, "Study of Schottky barriers on n -type GaN grown by low-pressure metalorganic chemical vapor deposition," *Applied Physics Letters*, vol. 67, p. 2657, 1995.
- [30] T. U. Kampen, M. Eyckeler, and W. Mönch, "Electronic properties of cesium-covered GaN (0001) surfaces," *Applied Surface Science*, vol. 123, pp. 28–32, 1998.
- [31] J. E. Bevins, "Characterization of a Boron Carbide Heterojunction Neutron Detection," Master's thesis, Air Force Institute of Technology, 2011.

REPORT DOCUMENTATION PAGE				Form Approved OMB No. 074-0188	
<p>The public reporting burden for this collection of information is estimated to average 1 hour per response, including the time for reviewing instructions, searching existing data sources, gathering and maintaining the data needed, and completing and reviewing the collection of information. Send comments regarding this burden estimate or any other aspect of the collection of information, including suggestions for reducing this burden to Department of Defense, Washington Headquarters Services, Directorate for Information Operations and Reports (0704-0188), 1215 Jefferson Davis Highway, Suite 1204, Arlington, VA 22202-4302. Respondents should be aware that notwithstanding any other provision of law, no person shall be subject to a penalty for failing to comply with a collection of information if it does not display a currently valid OMB control number.</p> <p>PLEASE DO NOT RETURN YOUR FORM TO THE ABOVE ADDRESS.</p>					
1. REPORT DATE (DD-MM-YYYY) 09-09-2011		2. REPORT TYPE Ph. D. Dissertation		3. DATES COVERED (From – To) July 2010 – September 2011	
4. TITLE AND SUBTITLE The Effects of Rare Earth Doping on Gallium Nitride Thin Films				5a. CONTRACT NUMBER N/A	
				5b. GRANT NUMBER N/A	
				5c. PROGRAM ELEMENT NUMBER N/A	
6. AUTHOR(S) McHale, Stephen R., LTC, USA				5d. PROJECT NUMBER N/A	
				5e. TASK NUMBER N/A	
				5f. WORK UNIT NUMBER N/A	
7. PERFORMING ORGANIZATION NAMES(S) AND ADDRESS(S) Air Force Institute of Technology Graduate School of Engineering and Management (AFIT/EN) 2950 Hobson Way WPAFB OH 45433-7765				8. PERFORMING ORGANIZATION REPORT NUMBER AFIT/DS/ENP/11-S05	
9. SPONSORING/MONITORING AGENCY NAME(S) AND ADDRESS(ES) Defense Threat Reduction Agency COL Mark Mattox 1900 Wyoming Blvd SE Kirtland AFB, NM 87117-5669				10. SPONSOR/MONITOR'S ACRONYM(S) DTRA/OP-CSU	
				11. SPONSOR/MONITOR'S REPORT NUMBER(S) N/A	
12. DISTRIBUTION/AVAILABILITY STATEMENT DISTRIBUTION STATEMENT A: APPROVED FOR PUBLIC RELEASE; DISTRIBUTION UNLIMITED					
13. SUPPLEMENTARY NOTES					
14. ABSTRACT The thermal neutron capture cross section of the rare earth (RE) metal isotope Gd-157 is the largest of all known natural elements, which distinguishes the material as a logical candidate for neutron detection. To address an incomplete understanding of rare earth doped Gallium Nitride (GaN) materials, investigations of the surface electronic structure and interface properties of GaN thin films doped with rare earths (Yb, Er, Gd) were undertaken. Lattice ion occupation, bonding, rare earth 4f occupation, and gold Schottky barrier formation were examined using synchrotron photoemission spectroscopy. Measured Debye temperatures indicate substitutional occupation of Ga sites by RE ions. The occupied RE 4f levels, deep within the valence band, suggest that intra-atomic f-f transitions may be more 'blue' than predicted by theoretical models. Thin layers of gold did not wet and uniformly cover the GaN surface, even with rare earth doping of the GaN. The resultant Schottky barrier heights for GaN:Yb, GaN:Er, and GaN:Gd, are 25-55% larger than those reported at the gold to undoped GaN interface. The utility of gadolinium as a neutron detection material was examined via fundamental nuclear and semiconductor physics. Low charge production and the large range of internal conversion electrons limits charge collection efficiency.					
15. SUBJECT TERMS Rare earth doping, Gallium Nitride, Thin films, Debye temperature, Resonant photoemission, Schottky barrier, Neutron detection					
16. SECURITY CLASSIFICATION OF:			17. LIMITATION OF ABSTRACT	18. NUMBER OF PAGES	19a. NAME OF RESPONSIBLE PERSON
REPORT	ABSTRACT	c. THIS PAGE			LTC John W. McClory, AFIT/ENP
U	U	U	U	181	19b. TELEPHONE NUMBER (Include area code) (937) 255-3636 ext 7308, john.mcclory@afit.edu